Tunable Photonic Crystal Devices

Vom Promotionsausschuss der
Technischen Universität Hamburg-Harburg
zur Erlangung des akademischen Grades
Doktor Ingenieur

genehmigte Dissertation

von
Jan Hendrik Wülbern
aus
Brunsbüttel

2010

Gutachter:

Prof. Dr. Manfred Eich (TU Hamburg–Harburg)

Prof. Dr. Ernst Brinkmeyer (TU Hamburg–Harburg)

Tag der mündlichen Prüfung:

15. Juli 2010

Contents

List of Figures

List of Abbreviations

2D	Two-Dimensional
3D	Three-Dimensional
APC	Amorphous Polycarbonate
BOX	Buried Oxide
CMOS	Complementary Metal Oxide Semiconductor
CST	Computer Simulation Technology
EBL	Electron Beam Lithography
EO	Electro-optic
FIT	Finite Integration Technique
FWHM	Full Width Half Maximum
GME	Guided Mode Expansion
I/O	Input Output
$LiNbO_3$	Lithium Niobate
MGE	Maxwell Grid Equation
MZI	Mach-Zehnder Interferometer
NLO	Nonlinear Optical
PBG	Photonic Bandgap
PhC	Photonic Crystal
P(MMA/DR1)	Poly(Methyl Methacrylate / Disperse Red 1)
Q	Quality Factor
RF	Radio Frequency
SEM	Scanning Electron Micrograph
SOI	Silicon-on-Insulator
TE	Transverse Electric
TM	Transverse Magnetic
TIR	Total Internal Reflection

Chapter 1

Introduction and motivation

Lightwave technology has been the backbone of long-haul communication and Internet traffic for more than 20 years up to today. It offers enormous transmission capacity, distant repeater spacing, is non-emitting and immune to electromagnetic interference. It is the only technology capable of meeting the vast and exponentially increasing demands of global communication [1, 2]. Owing to the immense bandwidth of optical transmission links and growing data rate demand, which is difficult to meet with electrical links, lightwave systems begin to replace copper in intermediate and short distance communication as well. Fiber to the home [3] and gigabit ethernet local area networks (LAN) [4] based on optical fibers are examples of mature and readily available technologies.

For example, in 2009 Luxtera (www.luxtera.com) introduced a 40 gigabits per second (Gbps) active optical cable transceiver with available cable lengths of 1 to 4000 m for the application in LANs, storage area networks and high performance computing (rack-to-rack and board-to-board interconnects). Apart from the data rate advantage, optical fiber cables facilitate physical installation due to smaller cable diameter, bend radii and immunity to electromagnetic interference compared to copper based interconnects [5]. All these benefits make optical links attractive in a number of application in the near future, where data rates will exceed the 1 Gbps threshold such as:

- Ultra high definition displays and display arrays with e.g. 3072 by 2304 pixels, 60 Hz repetition rate and 24 bit color depth;
- Parallel data access to arrays of multiple solid state disks with more than 0.25 Gbps data rate per disc;
- Data transfer in medical imaging, full body three-dimensional (3D) computed tomography ($\approx$ 20 gigabyte for one process).

At even shorter link distances, namely chip-to-chip and on-chip (die-to-die) communication, optical data links are emerging as a necessary alternative to electrical links [6, 7, 8]. As postulated by Moore's law, the integration density (i.e. transistor density on a chip) has grown exponentially in the last 40 years and simultaneously the data processing capabilities within one chip. However, the electrical data input and output (I/O) does not scale accordingly and requires increased power, reduced range and more sophisticated signal processing to keep up with bandwidth demands [9]. To overcome the limitations of electrical chip I/O, the introduction of optical I/O structures on microchips is necessary. Major microelectronics companies such as Intel, IBM, and Sun Microsystems recognized the advantages of lightwave technology and entered the active research of integrating electronic circuits and components for optical I/O.

Research of integrated lightwave technology encompasses six main areas or building blocks. These include generating the light, selectively guiding and transporting it, encoding light, detecting light, and intelligently controlling all of these photonic functions.

The focus of this thesis is on electro-optic (EO) modulators, which are essential on the transmitter side of optical interconnects to encode the (electrical) information onto a stream of photons. They convert an electric signal to an optical signal by modulating amplitude, frequency or phase of the optical carrier wave. Of special interest for EO-modulation is the Pockels effect, this second order effect, fundamentally a three wave mixing process, connects a change in refractive index with an external electric field and requires a second order nonlinear polarization. The EO-modulators developed in the scope of this project combine the benefits of three kinds of optical media, namely photonic crystals (PhC), silicon and nonlinear optical (NLO) organic materials, all three will be introduced briefly in the following.

Photonic crystals

A photonic crystal is an optical medium with a spatially periodic variation of the dielectric constant. Consequently they are built from at least two different materials, which are structured on the wavelength scale of light. The interaction of an optical wave with a periodic medium leads to the emergence of a spectral band structure, similar to the electronic band structure found in crystalline solids [10, 11]. Choosing an appropriate dielectric lattice geometry creates forbidden frequency regions, called photonic bandgaps (PBG), in which the light wave cannot propagate [12]. This effect originates from destructive interference among the multiply scattered waves at the periodic dielectric boundaries. PhCs are interesting for integrated optical circuits, since the PBG effect allows to manipulate

the propagation of light within a few lattice constants. Hence, they offer a high packing density, which is necessary for highly compact optical devices.

Two-dimensional (2D) PhC slabs are slab waveguides periodically structured in both in-plane directions. Consequently, the in-plane light propagation is governed by the band structure of the PhC and out-of-plane confinement is achieved by total internal reflection. These 2D PhC slabs have received considerable attention, because planar structures are relatively easy fabricated using current nano-patterning technology. By introducing point or line defects into the crystal lattice, resonant cavities or waveguides are formed respectively. Variations of the lattice geometry in the vicinity of these defects create virtually infinite degrees of freedom to manipulate the properties of the associated defect modes. For example PhC defect waveguides can be lattice engineered to have small group velocities with almost vanishing dispersion or extremely large (negative) dispersion [13]. Similarly PhC nanocavities have been shown to achieve quality factors exceeding 10^6, while the mode volume is only one cubic wavelength [14]. The resulting enhancement of the light and matter interaction may be exploited to increase the efficiency of NLO-processes. Here, the ability of PhC structures to form highly resonant cavities with a small geometrical footprint is applied to design highly efficient and compact EO-modulator devices.

Silicon photonics

Silicon is the standard material for highly integrated electrical circuits. At the same time it offers very attractive properties for integrated photonic circuits. These include a wide transparency window from near to mid infrared wavelengths. Its high refractive index ($n_{\mathrm{Si}} = 3.5$) at telecommunication wavelengths allows for waveguides with extremely tight bending radii and very compact components, while maintaining a moderate waveguide attenuation of 3 dB/cm [15]. The fabrication of silicon photonic circuits is fully compatible to the Complementary Metal Oxide Semiconductor (CMOS) process of microelectronic fabrication. The sum of these features offers the perspective of highly integrated photonic and electronic circuits on the same silicon chip in the near future [8, 16, 17, 18].

The crystal lattice of silicon is centrosymmetric and hence pristine silicon does not exhibit any $\chi^{(2)}$ nonlinearity, prohibiting EO-modulation. Research was very active in overcoming this limitation. Jacobsen and coworkers broke the centrosymmetry in silicon through strain induced on the atomic lattice and successfully demonstrated EO-activity [19]. However, the achieved Pockels coefficient was one order of magnitude lower than in the standard material used for EO-modulators today, Lithium Niobate ($LiNbO_3$).

Other approaches for electrically driven modulation of the optical properties of silicon

based photonic devices rely on the refractive index change resulting from the modulation of carrier density in silicon either by carrier depletion, injection or accumulation [20, 21, 22]. The achievable modulation speed using these methods is limited by the time constants with which the carriers can be injected into or removed from the area of the optical mode, which is in the order of nanoseconds. However, through the use of reversed biased pn-diodes, modulators with a 3 dB bandwidth of 30 GHz have been demonstrated [20].

The approach to be followed in the present thesis utilizes the excellent linear properties for confining and guiding the optical mode of silicon and its mature fabrication platform. For EO-modulation, the silicon device is to be hybridized with a nonlinear optical organic material to overcome the speed limitations set by the free carrier plasma dispersion in silicon.

Nonlinear optical organic materials

Typical organic NLO-materials with second order hyperpolarizabilities are optical polymers that have been functionalized either by doping of chromophores into the polymer matrix (guest-host system) or covalently binding the chromophore to the polymer chain (side-chain or main-chain systems). These chromophores are molecules, which have a strong dipole moment and high hyperpolarizability, due to the electron donor-π charge transfer bridge acceptor (D-π-A) structure. The nonlinear effect originates solely from the probability density distributions of different interacting electronic states and is hence inherently ultra fast ($<$ ps), enabling modulation bandwidths in the THz range [23]. Through polar alignment of the dipoles in the polymer along a preferential direction, which means breaking the centrosymmetry of the matrix, the bulk material develops a strong second order nonlinear polarization, manifesting in a $\chi^{(2)}$ susceptibility. Due to their dipole character, the chromophores are oriented technically by a strong static electric poling field. This process is referred to as poling.

Molecular engineering has led to a significant increase in the microscopic hyperpolarizability of the chromophores, yielding NLO-organic materials with bulk Pockels coefficients exceeding 300 pm/V at telecommunication wavelengths [24, 25, 26, 27]. This value surpasses $LiNbO_3$ by one full order of magnitude. This is a very important aspect, as the required drive voltage for modulation is inversely proportional to the Pockels coefficient.

Optical organic materials are a well suited material for optical applications because these compounds can show very low optical waveguide losses in the near infrared regime around the telecommunication windows of 1.3 μm and 1.55 μm ($<$ 1.0 dB/cm) due to their amorphous structures and the low absorption of their constituents [28]. The refractive

index of polymers is typically quite small ($n \approx 1.6$), which limits its light confinement abilities, mandating large bend radii of waveguides and hence restricts the integration of optical circuits on the chip level. However, in previous projects at this institute, it was demonstrated that polymer waveguide slabs can be a structured on the scale of nanometers to form two-dimensional photonic crystal slabs [29, 30].

NLO-polymers are typically applied on substrates by spin coating or, even simpler, drop casting from solution. The residual solvent is removed by baking the sample at an elevated temperature above the solvents boiling point. Depending on the solvent used, this is done in a range of 80 - 140°C. These features allow polymer materials to be integrated as a back-end process into the CMOS fabrication technology.

Objectives and outline of this thesis

The objective of this work is to develop concepts for EO-modulators, which meet the following requirements:

- operation at modulation frequencies in the microwave regime (> 10 GHz),
- low drive voltages (< 1 V), and
- ultra small geometrical footprint (on the scale of μm).

To fulfill the first two criteria organic NLO-materials are selected as the EO-functional medium, due to their inherently fast nonlinear response ($<$ ps) [23] and their ability to produce very high Pockels coefficients (> 300 pm/V) [26]. To comply with the requirement of a small geometrical footprint, the device design will focus on resonant PhC structures in silicon.

This thesis is structured as follows. In chapter 2, the theoretical background and fundamental concepts required for the results presented in the remainder of this thesis are revised. First, principles of second order NLO in organic materials are discussed and an introduction to the propagation of electromagnetic waves in media with periodically varying refractive index, photonic crystals, is given. Furthermore, physical mechanisms and effects of photonic cavities and resonant structures are reviewed. Finally, the simulation concepts used in this thesis are briefly introduced.

Chapter 3 analyzes possibilities to achieve full three-dimensional light confinement in resonant PhC slab structures (i.e. cavities) fabricated in NLO-polymers. Integrating the resonator structures completely into the NLO-polymer intrinsically leads to maximum field interaction with the NLO-material and hence ensures the largest possible spectral shift of the resonant frequency at a given amplitude of index modulation. Experimental

evidence of an omnidirectional photonic band gap in low index contrast PhC is presented. However, the subsequent detailed theoretical study concludes that highly resonant structures with small geometric footprint are not attainable in material configurations with low refractive index contrast.

In the following chapters EO-modulator structures based on Silicon-on-Insulator (SOI) substrates, which have been electro-optically functionalized with second order NLO-organic materials are developed and experimentally validated. Chapter 4 focuses on the design of PhC nanocavities in hybrid silicon-organic materials and the optimization of the spectral properties to enable a maximum modulation sensitivity while minimizing optical losses.

In chapter 5, EO-modulation in hybrid silicon-organic PhC devices with up to 40 GHz modulation bandwidth are experimentally demonstrated. The complete fabrication process with all relevant technological steps is explained. Issues of the high field poling process of second order nonlinear organic materials in narrow slot geometries are addressed. Finally, theoretical limitations of the proposed modulator concept are discussed.

Chapter 6 summarizes the results of the previous chapters and gives an outlook for further research.

Chapter 2

Theoretical background

2.1 Second order nonlinear optics in organic materials

This section gives an introduction into the general concepts of second order nonlinear optics (NLO) and into particular aspects of NLO-effects in organic materials. The discussion is restricted to effects, which are of relevance to this thesis. Comprehensive discussions of nonlinear optics can be found in references [2, 31] and of NLO in organic materials in references [32, 33]. The introduction into the NLO-effects of bulk optical media is followed by a discussion about the microscopic origin of NLO-effects in organic materials.

2.1.1 NLO-effects on the macroscopic scale

In a dielectric medium, the electric field $\mathbf{E}(t)$ of an electromagnetic wave induces dipole moments, resulting in the polarization density $\mathbf{P}(t)$. These two quantities are related to the displacement field $\mathbf{D}(t)$ via:

$$\mathbf{D} = \epsilon_0 \mathbf{E} + \mathbf{P} \tag{2.1}$$

$$= \epsilon_0 (1 + \chi) \mathbf{E}, \tag{2.2}$$

where the χ is the electric susceptibility, directly linking $\mathbf{E}$ and $\mathbf{P}$:

$$\mathbf{P} = \epsilon_0 \chi \mathbf{E}. \tag{2.3}$$

If the medium is anisotropic, the induced polarization density depends on the orientation of the electric field, thus the electric susceptibility has to be regarded as a tensor. In a nonlinear medium, χ is not a constant but dependent on the electric field itself and hence the relation between $\mathbf{P}$ and $\mathbf{E}$ can be expanded into a power series:

$$P_i = \epsilon_0 \left(\chi_{ij}^{(1)} E_j + \chi_{ijk}^{(2)} E_j E_k + \chi_{ijkl}^{(3)} E_j E_k E_l + \dots \right), \tag{2.4}$$

such that $\chi^{(n)}$ is a tensor of rank $(n+1)$, which are responsible for nonlinear optical effects for $n \geq 2$.

At this point, it should be noted that, in electric dipole approximation, only materials lacking an inversion symmetry (i.e. noncentrosymmetric materials) can exhibit second order NLO-properties. The rational behind this is that in media with inversion symmetry the polarization induced by two electric fields pointing in opposite directions are equal in amplitude and have opposite signs ($P(-E) = -P(E)$). Plugging this condition into equation 2.4 yields that $\chi^{(2)} = 0$ for materials with inversion symmetry.

The second order nonlinear susceptibility $\chi^{(2)}_{ijk}(-\omega_3; \omega_1, \omega_2)$ links the interaction of two electric fields $\mathbf{E}(\omega_1)$ and $\mathbf{E}(\omega_2)$ via the tensor product to the resulting nonlinear polarization response $\mathbf{P}(\omega_3)$. Important examples of second order nonlinear effects are second harmonic generation, optical rectification, three wave mixing and the electro-optic effect. The latter describes the interaction of a quasi-static (i.e. much lower in frequency compared to the optical field) electric field $\mathbf{E}(0)$ and the optical wave $\mathbf{E}(\omega)$, resulting in:

$$\mathbf{P}(\omega) = 2\epsilon_0 \chi^{(2)}(-\omega; \omega, 0)\mathbf{E}(\omega)\mathbf{E}(0). \tag{2.5}$$

The degeneracy factor of 2 is introduced into the above equation to account for the possible distinct permutations of the frequencies ω_1 and ω_2. Thus, the displacement field can be written as:

$$\begin{aligned} \mathbf{D}(\omega) &= \epsilon_0 \mathbf{E}(\omega) + \mathbf{P}(\omega) \\ &= \epsilon_0 \left(\underbrace{1 + \chi^{(1)}(-\omega, \omega)}_{\epsilon_r} + 2\chi^{(2)}(-\omega; \omega, 0)\mathbf{E}(0) \right) \mathbf{E}(\omega) \end{aligned} \tag{2.6}$$

where ϵ_r is the relative permittivity or dielectric tensor with the elements $\epsilon_{ij} = n^2_{ij}$. Its off diagonal elements vanish, if the coordinate system is chosen along the material's principal axis and it is then given by:

$$\epsilon_r = \begin{bmatrix} n^2_{11} & 0 & 0 \\ 0 & n^2_{22} & 0 \\ 0 & 0 & n^2_{33} \end{bmatrix}. \tag{2.7}$$

The nonlinear contributions in equation 2.6 can be regarded as a perturbation $\Delta\epsilon_{ij}$ to the corresponding tensor element:

$$\Delta\epsilon_{ij} = 2n_{ij}\Delta n_{ij} = 2\chi^{(2)}(-\omega; \omega, 0)\mathbf{E}(0) \tag{2.8}$$

and the refractive index change due to the EO-interaction can be written as:

$$\Delta n_{ij} = \frac{\chi^{(2)}_{ijk}(-\omega; \omega, 0)}{n_{ij}} E_k(0). \tag{2.9}$$

The electro-optic or Pockels coefficient is defined as the change of the impermeability $\eta = 1/\epsilon$:

$$\Delta\left(\frac{1}{n_{ij}^2}\right) \equiv r_{ijk}E_k(0). \tag{2.10}$$

Since the changes in Δn_{ij} are small for nonlinear optical processes, the EO induced change is:

$$\Delta n_{ij} = -\frac{n_{ij}^3}{2} r_{ijk}E_k(0) \tag{2.11}$$

and the tensor elements of the Pockels coefficient are linked to the counterparts of the nonlinear susceptibility by:

$$r_{ijk} = \frac{2\chi^{(2)}(-\omega;\omega,0)}{n_{ij}^4}. \tag{2.12}$$

2.1.2 Microscopic origin of NLO-effects in organic materials

The molecules, which are responsible for the second order nonlinearity in organic compounds are referred to as chromophores. In these molecules, the centrosymmetry is broken by deforming the π-electron distribution along a conjugated path by attaching groups with different electron affinity at both ends of the molecule. A simple example of such a molecule is given in figure 2.1. An acceptor- and a donor-like functional group are attached to an aromatic ring, which serves as a π-conjugated bridge. Due to an excess of charge at the acceptor side, the molecule has a dipole moment in its ground state. The response of the molecule to an electric field, or its polarizability, depends strongly on the direction of the applied field with respect to the molecule: charge flow is favored towards the acceptor, while hindered towards the donor. This asymmetric polarization provides strong second order nonlinear optical properties [33]. The polarization $\mathbf{p}$ on a molecular level can be written similar to equation 2.4:

$$p_i = \mu_i + \alpha_{ij}E_j + \beta_{ijk}E_jE_k + \gamma_{ijkl}E_jE_kE_l + \ldots \tag{2.13}$$

where μ is the ground state dipole moment of the molecule, α is the linear polarizability and β and γ are the first and second order hyperpolarizabilities, respectively. These coefficients are the microscopic counterparts of the susceptibilities in equation 2.4. Specifically, β is linked to $\chi^{(2)}$ and hence second order NLO-effects originate from the first order hyperpolarizability. Organic compounds offer a large flexibility of the molecular design, and extensive research in NLO-chromophores has led to very sophisticated molecular engineering with large β values. Reviews of the recent progress in this area are given in [27], [34], and [35].

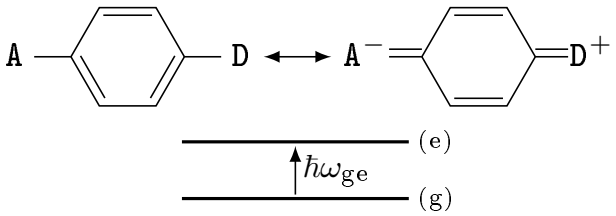

Figure 2.1: Ground state and first excited state of a chromophore molecule [33].

A simple model to predict the NLO properties of organic molecules is the two-level model. Within this model proposed by Oudar and Chemla [36, 37], the charge transfer contribution to the hyperpolarizability is given by [33]:

$$\beta(\omega_3;\omega_1,\omega_2) = 2\frac{e^2(\mu_\mathrm{e}-\mu_\mathrm{g})\mu_\mathrm{ge}^2}{\Delta E^2}\cdot\frac{\omega_\mathrm{ge}^4\left(3\omega_\mathrm{ge}^2+\omega_1\omega_2-\omega_3^2\right)}{\left(\omega_\mathrm{ge}^2-\omega_1^2\right)\left(\omega_\mathrm{ge}^2-\omega_2^2\right)\left(\omega_\mathrm{ge}^2-\omega_3^2\right)}, \tag{2.14}$$

where μ_g and μ_e denote the dipole moments of the ground and excited state, respectively. The transition dipole moment from is given by μ_ge and the energy difference of the states by ΔE. For EO-processes this expression simplifies to ($\omega_1 = -\omega_3 = \omega$ and $\omega_2 = 0$):

$$\beta(-\omega;\omega,0) = \underbrace{\frac{e^2(\mu_\mathrm{e}-\mu_\mathrm{g})\mu_\mathrm{ge}^2}{\Delta E^2}}_{\beta_0^\mathrm{EO}}\cdot\frac{\omega_\mathrm{ge}^2\left(3\omega_\mathrm{ge}^2-\omega^2\right)}{\left(\omega_\mathrm{ge}^2-\omega^2\right)^2}. \tag{2.15}$$

The term β_0^EO is referred to as the dispersion free or off-resonant hyperpolarizability since it is not dependent on the frequency of the optical fields involved in the nonlinear process.

The two-level model has been used up to the 1990s to guide the design of NLO-organic molecules. Today, calculations based on the quantum sum-over-states methods are used to determine the largest off-resonance nonlinear susceptibility allowed by quantum mechanics [38, 39]. This approach aided the development of new molecular designs with ultra-high intrinsic hyperpolarizabilities based on the modulation of conjugation [40]. M. G. Kuzyk used this method to identify the fundamental quantum limit of hyperpolarizability in second order NLO-molecules and concluded that bulk EO-coefficients exceeding 3000 pm/V in dye-doped polymers are feasible [41]. This value is one order of magnitude larger compared to the experimentally reported values [26], suggesting significant improvement potential in the design of NLO-molecules. Reviews of molecular engineering strategies for second order NLO-organic materials can be found in [27], [34], and [42].

The delocalization of the intra-molecular charges along the the π-conjugated bridge is almost instantaneous, resulting in response times in the femtosecond regime. This is a very important advantage of NLO-organic materials, especially in the context of broadband EO modulators with up to 100 GHz bandwidth. In fact, NLO-polymer based EO-modulators operating above 1 THz were demonstrated [23].

The molecular architecture of chromophores with strong donor and acceptor pairs connected by a conjugated bridge makes them susceptible to photodecomposition, which compromises their NLO-properties. This effect is most profound when the frequency of the incident radiation is at or close to the absorption bands (typically in the ultra-violet and visible spectrum) of the NLO-chromophore. This process leads to a reduction of the refractive index and is also known as photobleaching, which can be used to define optical waveguides in NLO-polymer films [43, 44]. In the near infrared part of the spectrum, relevant for telecommunication, this effect is orders of magnitude smaller compared to frequencies close to the absorption band [45]. However, it is also important to consider the photochemical stability of NLO-polymers at near infrared frequencies for long lifetime operation. Recent studies show that shielding the chromophores from ambient oxygen and singlet oxygen in the polymer matrix is essential for long lifetime polymeric telecommunication devices [46, 47]. Using these techniques, stable operation of EO-polymer devices at light intensities of 1 MW/cm^2 has been reported [48].

Achieving high $\chi^{(2)}$ values requires strong first order hyperpolarizability molecules. However, in amorphous polymers, the chromophores are randomly oriented, hence are macroscopically centrosymmetric and $\chi^{(2)} = 0$. Consequently, the chromophores in the polymer matrix have to be oriented in a preferential direction in order to observe macroscopic second order NLO-effects. Methods to orient the dipole moments are static field poling, photoassisted poling and all optical poling. Detailed information on these techniques can be found in reference [32]. In this thesis, the electrode contact static field poling is employed and shall be introduced briefly in the following.

As the name suggests, for electrode contact poling, the NLO-polymer is sandwiched between two electrodes (figure 2.2). Between these electrodes, the poling voltage V_{pol} is applied. The sample is then heated to the glass transition temperature T_g, where the mobility of the molecules is increased, allowing them to reorient within the matrix. Due to their electric dipole nature, the chromophores will then orient themselves along the applied static electric field. The sample is then cooled down to room temperature, still with the field turned on, thus freezing in the chromophore orientation. At room temperature, the poling voltage is turned off.

This state of the molecule ensemble is thermodynamically not stable and the orientation tends to decrease over time. The poled order relaxation of the chromophore molecules over time results from rotational diffusion processes in the polymer matrix. The temporal decay of the EO-coefficient is usually described by the Kohlrausch-Williams-Watt

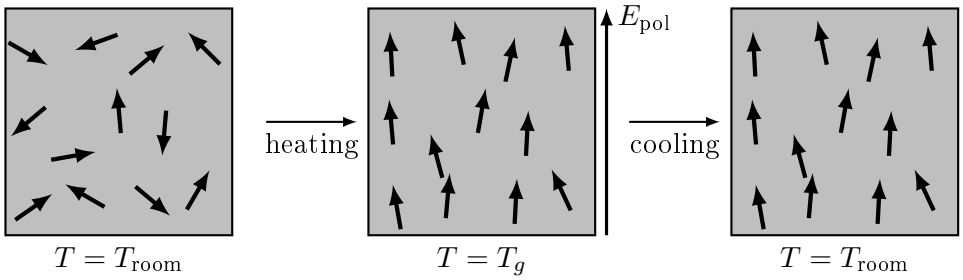

Figure 2.2: Schematic of the poling procedure. The chromophores are aligned at the glass temperature T_g by a static poling field E_{pol}.

stretched exponential function [32]:

$$r_{33}(t) = r_{33}(0)\,[-(t/\tau)^w] \tag{2.16}$$

where τ is a temperature dependent relaxation time constant and w describes the width of relaxation (deviation from monoexponential behavior). The values of these parameters depend on the measurement temperature. The closer the measurement temperature is to the glass transition temperature, the smaller the time constant and the larger the relaxation rates. The parameters are typically found by fitting the function to experimentally obtained data. Alternatively, a biexponential function can be used to describe the temporal decay. Both methods have shown to provide accurate results.

Long term thermal stability of the macroscopic second order NLO-effect was demonstrated in EO-polymers with high glass transition temperature ($T_{\text{g}} \approx 200°\text{C}$), retaining 90% of their inital Pockels coefficient for more than 1000 h at an elevated temperature of 100°C [49, 50]. By crosslinking the polymer matrix after the poling process, the rotational flexibility of the chromophore is hindered due to increased T_{g} and interchain entanglement of the polymer. Using this technique, thermal stabilities of up to 85°C were achieved [51, 52].

The microscopic contribution from the first order hyperpolarizability β is in general not easily linked to the macroscopic $\chi^{(2)}$ response of the NLO-polymer. A simplified treatment, however, is provided by the oriented gas model, giving a good approximation for poled EO-polymers. This model provides a simple relation of the β tensor elements given in the molecular coordinate system (x, y, z) and the $\chi^{(2)}$ tensor elements, which are given in the laboratory frame (X, Y, Z) (figure 2.3). The assumptions made by the oriented gas model are:

- The chromophores are assumed to rotate freely under the influence of the applied field at the poling temperature. Chromophore-chromophore coupling or interaction

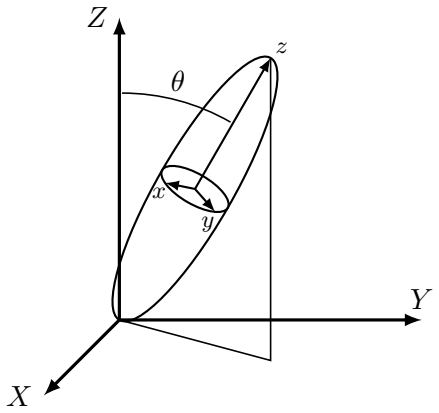

Figure 2.3: Laboratory (X, Y, Z) and chromophore (x, y, z) coordinate systems.

with the surrounding polymer matrix is ignored.

- The chromophores have cylindrical symmetry about the z axis and the only non-vanishing hyporpolarizability tensor element is β_{zzz}.
- The chromophore's dipole moment μ is oriented along the z axis.
- The chromopores are not interacting with each other.

Using these approximations, only two independent elements remain in the macroscopic second order susceptibility tensor, which are obtained from:

$$\chi^{(2)}_{ZZZ} = Nf\beta_{zzz} \left\langle \cos^3\theta \right\rangle \tag{2.17}$$

$$\chi^{(2)}_{ZXX} = Nf\beta_{zzz} \left\langle \cos\theta \sin^2\theta \right\rangle /2, \tag{2.18}$$

where N is the chromophore number density, f the local field correction factor and θ denotes the angle between poling field and the molecular axis. The distribution of the angular orientation can be expressed by Langevin functions of first and third order, which in turn are typically approximated a Maxwell-Boltzmann distribution function, giving two rather simple expressions for the averaging terms in the equations above (for a complete derivation see for example [33]):

$$\left\langle \cos^3\theta \right\rangle \approx \frac{\mu E_Z}{5k_BT} \quad \text{and} \quad \left\langle \cos\theta \sin^2\theta \right\rangle \approx \frac{2\mu E_Z}{15k_BT}, \tag{2.19}$$

where E_Z is the applied poling field, μ is the dipole moment, k_B is Boltzmann's constant and T is the temperature at which the polymer is poled. The molecules orient in the direction of the applied field to reduce their interaction potential μE_z. However, this

effect is in competition with the thermal disorientation energy k_BT. The macroscopic tensor components are found from:

$$\chi^{(2)}_{ZZZ} = Nf\beta_{zzz}\frac{\mu E_Z}{5k_BT}, \tag{2.20}$$

$$\chi^{(2)}_{ZXX} = Nf\beta_{zzz}\frac{\mu E_Z}{15k_BT}. \tag{2.21}$$

Hence, within this model, the ratio between the two tensor elements is given as:

$$\frac{\chi^{(2)}_{ZZZ}}{\chi^{(2)}_{ZXX}} = 3. \tag{2.22}$$

By using Voigt's notation to express the tensor indices in contracted form, the above elements become $\chi^{(2)}_{33}$ and $\chi^{(2)}_{13}$. Analogously, one finds for the Pockels coefficients r_{33} and r_{13} that $r_{33} = 3r_{13}$.

The above approximations of the Langevin functions are only valid if $\mu E_Z/k_Bt < 1$, which is often satisfied in experimental conditions. However, for large degrees of angular orientation $\langle\cos\theta\rangle$, the linearized model of the Langevin function (equation 2.19) is no longer valid and the ratio of $\chi^{(2)}$ tensor components can be larger than 3.

2.2 Photonic crystals

Photonic crystals (PhCs) are artificial optical media, whose refractive index is varied periodically on the scale of the optical wavelength. This periodicity of dielectric interfaces causes destructive multiwave interference for certain frequency regions, prohibiting propagation of a wave inside the PhC. These frequency regions are called photonic band gaps (PBGs), in analogy to the electronic band gaps in semiconductor materials.

PhCs are distinguished by the dimensionality of their periodicity in one-dimensional, two-dimensional, and three-dimensional crystals. One-dimensional crystals are essentially multilayer films, which have first been studied by Lord Rayleigh in 1887 [53]. However, the notion of photonic crystals was first coined by Yablonovitch [10] and John [11] with the introduction of 2D and 3D PhC structures. A standard text to the introduction to PhC is the book by Joannopoulos et al. [54].

To understand the propagation of waves in a medium with a spatially periodic dielectric constant one starts with Maxwell's equations for time harmonic fields ($\mathbf{A}(\mathbf{r},t) = \mathbf{A}(\mathbf{r})\exp(-j\omega t)$):

$$\begin{aligned} \nabla\times\mathbf{H} &= -j\omega\mathbf{D}+\mathbf{J} & \nabla\cdot\mathbf{D} &= \rho \\ \nabla\times\mathbf{E} &= j\omega\mathbf{B} & \nabla\cdot\mathbf{B} &= 0 \end{aligned} \tag{2.23}$$

and the material relations:

$$\mathbf{D}(\mathbf{r}) = \epsilon_0 \epsilon_r(\mathbf{r})\mathbf{E}(\mathbf{r}) \qquad \mathbf{B}(\mathbf{r}) = \mu_0 \mu_r(\mathbf{r})\mathbf{H}(\mathbf{r}). \tag{2.24}$$

The dielectric materials considered in this text are assumed to be free of charges ($\rho = 0$) and currents ($\mathbf{J} = 0$) and the magnetic permeability is unity ($\mu_r = 1$). The relative permittivity ϵ_r is then related to the refractive index by $n^2 = \epsilon_r$ and the vacuum speed of light is $c = 1/\sqrt{\epsilon_0 \mu_0}$. The equations 2.23 and 2.24 can then be rearranged to give an expression entirely in $\mathbf{H}(\mathbf{r})$, which is called the master equation:

$$\nabla \times \left(\frac{1}{\epsilon_r(\mathbf{r})} \nabla \times \mathbf{H}(\mathbf{r}) \right) = \left(\frac{\omega}{c} \right)^2 \mathbf{H}(\mathbf{r}), \tag{2.25}$$

This is an eigenvalue problem for the eigenmodes $\mathbf{H}(\mathbf{r})$ with the eigenvalue $(\omega/c)^2$. A PhC has a periodic refractive index distribution $\epsilon(\mathbf{r}) = \epsilon(\mathbf{r} + \mathbf{R})$, where $\mathbf{R} = N_1\mathbf{a}_1 + N_2\mathbf{a}_2 + N_3\mathbf{a}_3$ is the primitive lattice vector. Thus, the Bloch-Floquet theorem can be applied to the solution of the eigenproblem. The field distribution for any given wave vector $\mathbf{k}$ consequently is a periodic function in space multiplied by $\exp(j\mathbf{k} \cdot \mathbf{r})$ and can be written in the form:

$$\mathbf{H}_\mathbf{k}(\mathbf{r}) = e^{j\mathbf{k}\cdot\mathbf{r}} \mathbf{u}_\mathbf{k}(\mathbf{r}) \tag{2.26}$$

$$\mathbf{u}_\mathbf{k}(\mathbf{r}) = \mathbf{u}_\mathbf{k}(\mathbf{r} + \mathbf{R}). \tag{2.27}$$

Therefore, the analysis of the problem can be restricted to the primitive cell of the lattice. This solution is then easily expanded to the entire lattice. The primitive cell is a finite domain leading to discrete eigenvalues $i = 1, 2, \ldots$. The eigenvalues $\omega_i(\mathbf{k})$ are continuous functions of $\mathbf{k}$, resulting in the discrete bands when plotted versus the wave vector. In the context of PhC the dispersion relation ω versus $\mathbf{k}$ is also called band diagram.

The master equation is scale invariant, in other words there is no fundamental length scale. If the refractive index function is scaled in space by $\epsilon'(\mathbf{r}) = \epsilon(\mathbf{r}/s)$, the new mode profile is obtained from rescaling the old mode profile $\mathbf{H}'(\mathbf{r}') = \mathbf{H}(\mathbf{r}'/s)$ and similarly the new mode frequency is rescaled to $\omega' = \omega/s$. For this reason, the band diagram is typically presented in a notation where frequency $\omega a/2\pi c$ and wave vector $ka/2\pi$ are normalized to the lattice constant a.

Another important scaling property concerns the magnitude of the refractive index function. If its value is increased by a constant factor s everywhere $n'(\mathbf{r}) = s \cdot n(\mathbf{r})$, the frequency of the mode decreases by the same factor $\omega' = \omega/s$. However, the mode profiles remain unchanged.

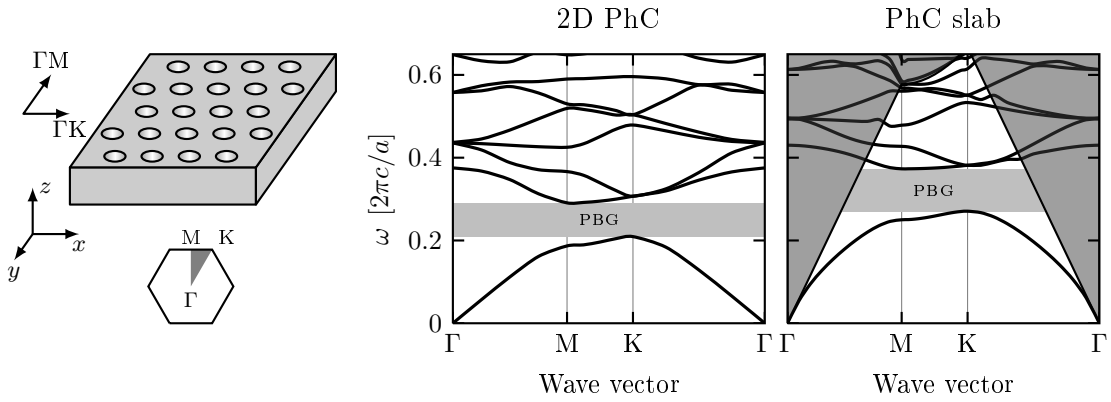

Figure 2.4: Band diagram of an infinite 2D PhC and a PhC slab of triangular lattice of air holes in silicon ($n_{\mathrm{si}} = 3.5$) in TE-like polarization, with the irreducible Brillouin zone at the lower left.

2.2.1 Photonic crystal slabs

A photonic crystal slab is a slab waveguide, which has a periodic index variation in both in-plane directions. The periodicity is two-dimensional and hence it could be regarded as a 2D PhC. However, due to the slab structure, its vertical translational symmetry is broken. Therefore these structures are commonly referred to as 2.5D systems or photonic crystal slabs. The latter will be used in this thesis. PhC slabs are of technological significance, because they can be fabricated using standard planar lithography and etching processes.

Due to the vertical mirror symmetry at the center of the slab, the modes can be separated into vertically even (H_{z} and E_{xy} components having symmetrical field distributions with respect to the mirror plane) and odd modes (antisymmetrical field distribution). Consequently, in the xy-mirror plane itself the even mode has only H_{z} and E_{xy} as its non vanishing field components and is purely transverse electrically (TE) polarized. Analogously the odd mode is purely transverse magnetically (TM) polarized at the slab mirror plane [55]. Moving away from the center all field vector components are non-zero. Hence the nomenclature of TE-like and TM-like modes is commonly used [54]. PhC slabs with air holes in a high dielectric slab preferably sustain a band gap for the TE mode. Hence, all following discussions of this text consider the TE polarized mode.

Photonic crystal slabs confine the light vertically within the slab via index guiding, a generalization of total internal reflection. Due to the in-plane periodicity, the wave vectors parallel to the plane $\mathbf{k}_{||}$ form a band structure when plotted versus the frequency ω, which is very similar to the band structure of the true 2D case (a direct comparison of the two diagrams in displayed in figure 2.4). The bands in the PhC slab case are shifted to higher frequencies because the effective refractive index of the slab is lower than the index of

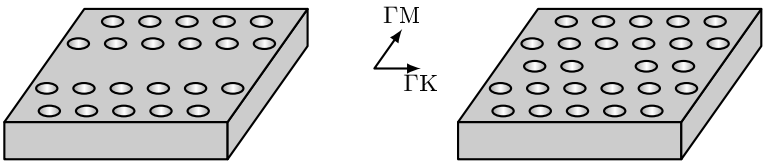

Figure 2.5: Schematic of line defect (left) and point defect (right) in a PhC slab.

the bulk material. The eigensolutions of the cladding medium are $\omega = c_{\text{clad}}\sqrt{|\mathbf{k}_{||}|^2 + k_{\perp}^2}$, where c_{clad} is the speed of light in the cladding medium $c_{\text{clad}} = c_0/n_{\text{clad}}$. When plotted against $\mathbf{k}_{||}$ this forms the continuous light cone $\omega \geq c_{\text{clad}}|\mathbf{k}_{||}|$, indicated by the darker region in figure 2.4. Modes beneath the light cone are confined to the slab and their field decays exponentially in the vertical direction. Since modes within the light cone radiate energy to the continuum, they are also referred to as radiation modes.

When omitting or shifting holes from their lattice positions, the periodic translational symmetry of the PhC is broken. Such deviations from the perfect PhC structure are called defects and form allowed states (defect states) within the photonic band gap. The most prominent examples of such defects are line defects and point defects (figure 2.5).

Line defects are formed by omitting a row of holes along one of the lattice directions. This forms a waveguide effectively consisting of two photonic crystal mirrors, providing confinement of the mode lateral to the propagation direction. The geometric structure is periodic in the direction of propagation and hence the propagating modes are Bloch modes. In principle for all modes below the light cone lossless operation is possible, when neglecting absorption and scattering from geometrical imperfections of the lattice (e.g. fluctuations in hole size, position and shape). PhC line defect waveguides have received considerable attention in the research community because their dispersion relation can be widely tuned by modifying the geometric properties of the PhC.

A point defect is formed by omitting or changing the size of one single or multiple adjacent holes in the PhC lattice. This type of defect can define localized modes for resonant frequencies within the band gap, as propagation is hindered in all in-plane directions by the PhC. Vertically the light is confined by the total internal reflection condition. The defect serves as a microcavity resonator. The modal volume of the cavity is typically in the order of one cubic wavelength, thus confining the optical energy very tightly. However, because translational symmetry of the PhC is broken and the resonant mode is spatially localized, the mode now has a continuum of wave vector components, parts of which can couple to the modes in the light cone and radiate energy. Consequently, these localized modes are always lossy. Methods to reduce the vertical radiation losses in PhC slab resonators are analyzed extensively in chapters 3 and 4. The losses of resonators are

quantified by their quality factor. This quantity and its importance for resonant systems will be discussed in the next section.

2.3 Cavities and resonators

An optical resonator confines light at resonance frequencies, which are determined by its configuration. It can be regarded as an optical transmission system with incorporated feedback. The light circulates or is repeatedly reflected within the resonator. Optical resonators are characterized by two key parameters, reflecting their ability to confine the optical energy temporally and spatially: The former is quantified by the quality (Q) factor and the latter by the mode volume V. Q is directly proportional to the storage time, a large value indicates strong temporal confinement. The mode volume measures the volume occupied by the optical mode, and a small value represents strong spatial confinement. Resonators are generally frequency selective elements and may serve as spectral analyzers and optical filters.

Assuming the energy stored in a resonator decays with the time constant τ, the optical field of this mode then decays with:

$$E(t) = E_0 e^{-j\omega_0 t} e^{-t/2\tau}, \tag{2.28}$$

where ω_0 is the resonant frequency. The frequency spectrum of the output intensity of this resonator is found by taking the Fourier transform of the previous equation:

$$|\mathcal{F}\{E(t)\}|^2 \propto I(\omega) = I_0 \frac{1}{4\left(\frac{\omega-\omega_0}{\Delta\omega}\right)^2 + 1}, \tag{2.29}$$

yielding a Lorentzian function, with a spectral line width defined by the full width at half maximum (FWHM) $\Delta\omega = 1/\tau$.

The Q factor of resonant circuits is defined as the ratio of stored energy (W) and the energy loss per cycle (P). Since, by definition, the energy decays with the rate of τ, the Q factor can be related to the ratio of resonance frequency ω_0 to the line width $\Delta\omega$:

$$Q = \frac{\omega_0 W}{P} = \omega_0 \tau = \frac{\omega_0}{\Delta\omega}. \tag{2.30}$$

Generally, multiple loss mechanisms are responsible for the resonator characteristic. These include losses at imperfect and finite sized mirrors as well as material absorption and scattering loss inside the resonator. An individual decay time τ_i and hence indvidual quality factor Q_i can be attributed to each of these dissipative mechanisms. These

individual parameters are connected to the total decay constant and quality factor via:

$$Q_{\mathrm{tot}} = \omega_0 \tau = \omega_0 \left[\sum_i \frac{1}{\tau_i} \right]^{-1} = \left[\sum_i \frac{1}{Q_i} \right]^{-1}. \tag{2.31}$$

Hence, the total Q is limited by the smallest individual Q factor, or, in other words, the strongest loss mechanism.

A microcavity in an infinitely extended PhC slab of lossless material, exhibits only vertical loss from coupling to radiation modes within the light cone. The associated quality factor is typically referred to as vertical Q or intrinsic Q because it is an intrinsic property of the isolated cavity. In the remainder of this text this value is expressed as $Q_\perp$. When the cavity is coupled to access waveguides, an additional loss mechanism is introduced, which is denoted by the in-plane quality factor $Q_{||}$. The cavity acts as a filter on the transmission function from the input to the output waveguide, transmitting only the resonant frequencies.

The transmission characteristic of a resonator coupled to a waveguide can be derived from coupled mode theory, which allows to express the transmission spectrum as a function of Q factors (a thorough derivation can be found in [54] and [56]):

$$T(\omega) = \frac{\left(\frac{Q_{\mathrm{tot}}}{Q_{||}} \right)^2}{4 \left(\frac{\omega - \omega_0}{\Delta\omega} \right)^2 + 1}. \tag{2.32}$$

Evidently, the spectral width of the transmission is the same as for the isolated cavity. However, the peak transmission T_0 at resonance is not 100%, but determined by the ratio of total to in-plane Q:

$$T_0 = \left(\frac{Q_{\mathrm{tot}}}{Q_{||}} \right)^2 = \left(1 - \frac{Q_{\mathrm{tot}}}{Q_\perp} \right)^2. \tag{2.33}$$

This means that the transmission at resonance is almost unity when $Q_\perp \gg Q_{||}$. This is easily explicable, since the cavity mode decays much more quickly into the waveguide than into the surrounding medium.

Here, the resonator shall be used for electro-optic modulation. A variation of the refractive index within the resonator volume causes a shift of the resonance frequency $\Delta\omega_0$ and consequently a shift of the transmission spectrum, thus modulating the transmission at a given frequency ω_p with the modulation depth ΔT (see figure 2.6). Clearly, the larger the Q, the deeper is the modulation depth for a fixed shift in resonance frequency. From this it follows that an efficient modulator should have its Q as large as possible to exhibit a large modulation depth with small shifts in resonance frequency. However, using resonant structures as modulators in high data rate communication schemes poses an upper limit

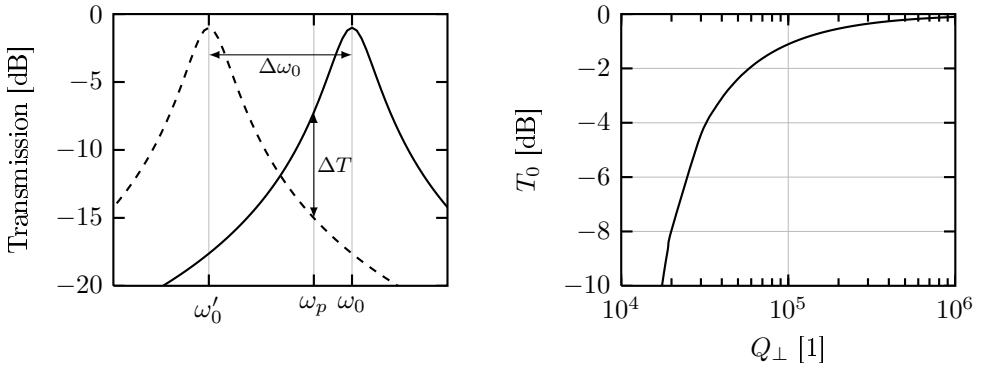

Figure 2.6: Spectral shift of the resonator transmission by $\Delta\omega$, resulting in a modulation depth ΔT at ω_p (left). Maximum transmission at resonance T_0 plotted against the cavity intrinsic Q factor (right).

on the permissible Q factor of the device. The photon lifetime τ should not exceed the time spacing between two data symbols, as this would lead to inter-symbol interference. Targeting 100 GHz operational bandwidth results in $\tau < 10$ ps. At the telecommunication wavelength of $\lambda = 1550$ nm, this yields a maximum total Q of $Q_{\text{tot}} = 12 \cdot 10^3$.

The maximum transmission of a resonator based modulator determines the insertion loss of the device and hence is desired to be close to to unity or 0 dB. From equation 2.33, it is easy to find the maximum transmission of a resonant cavity once the total and intrinsic Q are known. Obviously, the optimal cavity would have $Q_\perp = \infty$, this, however, is not possible in a PhC slab nano cavity. Even in a defect surrounded by a perfect PhC lattice the intrinsic Q can only be finite, due to wave vector components that are inside the light cone. In real world cavities this value will be further reduced by material absorption of the dielectric slab and additional vertical scattering losses from imperfections in the geometry (e.g. fluctuations in hole size, position and shape) of the PhC lattice.

In figure 2.6, T_0 is plotted versus the vertical Q factor of a cavity with $Q_{\text{tot}} = 12 \cdot 10^3$, which was identified to be the upper limit of the total Q factor in a resonant EO-modulator. In view of these boundary conditions it is obvious that overall device design has to primarily concentrate on the maximization of the intrinsic Q factor. At the same time simplifying the simulation efforts, as only isolated cavities need to be considered in the first design step. The minimum intrinsic Q factor $Q_\perp^{\min}$ required for any PhC cavity EO-modulator with given maximum transmission can be found from the right hand panel in figure 2.6. Hence, for an insertion loss not larger than 1 dB resonators with $Q_\perp > 10^5$ are a necessity.

2.4 Simulation concepts

The description of electromagnetic problems is entirely contained in Maxwell's equations presented in 2.23, and thus all optical properties of PhCs can be inferred from the solution of these equations. However, in complex two- and three-dimensional material arrangements, an analytic solution is generally not available. Over the last decades, several numerical techniques have been developed to efficiently solve partial differential equations like Maxwell's equations. Combined with the increase of computing power, this has led to a multitude of tools, which are available in computational photonics for the design of photonic structures. Numerical and experimental results are in fact in such a good agreement that it has become common practice to optimize devices in "numerical experiments" before the device is actually fabricated. For the design of the devices presented in the following chapters, the Finite Integration Technique (FIT) and Guided Mode Expansion method (GME) were used. Both shall be introduced here briefly.

2.4.1 Guided mode expansion

The GME method was developed by Andreani et al. for the efficient calculation of band diagrams of PhC slabs [57]. It is a special implementation of the well-known plane wave expansion method [58] to solve the master equation 2.25 and to obtain the mode frequencies and field distributions for any wavevector $\mathbf{k}$. An implementation of the code is provided as free software by L. C. Andreani [59].

In the plane wave expansion method, the periodic Bloch envelope of the magnetic field given in equation 2.26 is expanded into a three-dimensional Fourier series:

$$\mathbf{u_k}(\mathbf{r}) = \sum_{\mathbf{G}} \mathbf{c_G}(\mathbf{k}) e^{i\mathbf{G}\mathbf{r}}, \tag{2.34}$$

where $\mathbf{G}$ is the reciprocal lattice vector. The master equation 2.25 is transformed into a linear eigenequation by inserting the last expression and Fourier transformation:

$$\sum_{\mathbf{G}} \left[-\epsilon^{-1}_{\mathbf{G}'-\mathbf{G}} \cdot (\mathbf{k}+\mathbf{G}') \times (\mathbf{k}+\mathbf{G}) \times \right] \mathbf{c_G} = \frac{\omega^2}{c^2} \mathbf{c_{G'}}, \tag{2.35}$$

where $\epsilon^{-1}_{\mathbf{G}'-\mathbf{G}}$ is the Fourier transform of the inverse dielectric function. The above equation is typically solved numerically by truncating the infinite sum over $\mathbf{G}$ by introducing a wavevector cutoff $|\mathbf{G}| < \Lambda$.

The guided mode expansion method uses a slightly different basis to expand the magnetic field. Since it is applied to PhC slabs, it represents the field as a combination of

two-dimensional plane waves in the slab plane xy and as guided modes perpendicular to the slab plane (i.e. along z). This is expressed as:

$$\mathbf{H}_{\mathbf{k}}(\mathbf{r}) = \sum_{\mathbf{G},\alpha} c(\mathbf{k}+\mathbf{G},\alpha)\mathbf{H}^{\text{guided}}_{\mathbf{k}+\mathbf{G},\alpha}(\mathbf{r}). \tag{2.36}$$

The term $\mathbf{H}^{\text{guided}}_{\mathbf{k}+\mathbf{G},\alpha}(\mathbf{r})$ describes the guided modes of the effective waveguide at $(\mathbf{k}+\mathbf{G})$ and α is the index of the guided mode. The effective waveguide is considered to have a homogeneous refractive index distribution in its substrate, core and cladding layer. The refractive index in each layer is found by taking the spatial average of its $n(x,y)$ distribution within the unit cell of the PhC.

The GME does not introduce any artificial periodicity in the vertical direction. In the case of a monomode effective slab waveguide, the numerical effort is comparable to a 2D plane wave calculation. Hence, the calculation time for PhC slab band structures is reduced considerably compared to a 3D plane wave calculation. Furthermore, the coupling of modes above the light line to radiative modes of the continuum is quantified by this method by by using time-dependent perturbation theory (in analogy to Fermi's golden rule for quantum mechanics), which yields the imaginary part of the frequency of these lossy modes [57].

2.4.2 Finite integration technique

All FIT calculations presented in this thesis were obtained from the commercially available "Microwave Studio" program, which is maintained and distributed by the Computer Simulation Technology (CST) company in Darmstadt, Germany. A thorough introduction to the application of this software for PhC problems can be found in [60]. In the FIT algorithm, Maxwell's equations are applied to a discretized simulation volume in integral form.

Prior to the simulation of the actual electromagnetic problem, the simulation domain is discretized into a rectangular grid, defining finite mesh cells. Along the edges of these, the electric voltages **e** and through the facets the the magnetic fluxes **b** are defined as presented in figure 2.7. Simultaneously, a secondary grid is created orthogonally to the first one. The electric flux **d** and magnetic voltages **h** are defined along the facets and edges of this secondary grid, respectively.

The Maxwell equations are then applied to each of the cell facets. Faraday's law of induction:

$$\oint_{\partial A} \mathbf{E}\, d\mathbf{s} = -\frac{\partial}{\partial t} \iint_{A} \mathbf{B}\, d\mathbf{A} \tag{2.37}$$

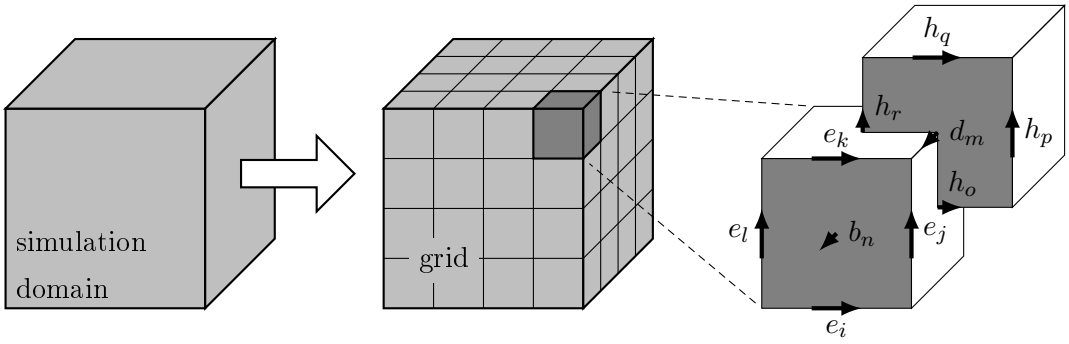

Figure 2.7: Generation of the computational primary and secondary grid used for the discretization in the FIT method. The electric voltages $\mathbf{e}$ and magnetic fluxes $\mathbf{b}$ are defined on the edges and faces of the primary grid, while the magnetic voltages $\mathbf{h}$ and dielectric fluxes $\mathbf{d}$ are defined on the secondary grid.

can be written at the facet n as:

$$e_i + e_j - e_k - e_l = -\frac{\partial}{\partial t} b_n. \tag{2.38}$$

Repeating this procedure for all available cell facets summarizes the calculation rule in a matrix formulation, introducing the topological matrix $\mathbf{C}$ as the discrete equivalent of the analytical curl operator:

$$\mathbf{Ce} = -\frac{\partial}{\partial t}\mathbf{b}. \tag{2.39}$$

The same procedure is applied to the secondary grid with Ampere's law and the topological matrix $\tilde{\mathbf{C}}$. Similarly, the discretization of the remaining divergence equations introduces discrete divergence operators $\mathbf{S}$ and $\tilde{\mathbf{S}}$, belonging to the primary and secondary grids, respectively. This results in the following notation of the Maxwell equations:

$$\begin{aligned} \tilde{\mathbf{C}}\mathbf{h} &= \mathbf{j} + \frac{\partial}{\partial t}\mathbf{d} & \tilde{\mathbf{S}}\mathbf{d} &= \mathbf{q} \\ \mathbf{Ce} &= -\frac{\partial}{\partial t}\mathbf{b} & \mathbf{Sb} &= \mathbf{0} \end{aligned}, \tag{2.40}$$

which is referred to as the Maxwell Grid Equations (MGE) [61, 62], where $\mathbf{j}$ are the electric currents through the facets and $\mathbf{q}$ the electric charges in the grid cells.

For the complete description of the electromagnetic properties of the modeled structures, the material equations need to be written in the matrix notation as well:

$$\begin{aligned} \mathbf{D} &= \epsilon\mathbf{E} & & & \mathbf{d} &= \mathbf{M}_\epsilon\mathbf{e} \\ \mathbf{B} &= \mu\mathbf{H} & \Longrightarrow & & \mathbf{b} &= \mathbf{M}_\mu\mathbf{h} \\ \mathbf{J} &= \sigma\mathbf{E} + \mathbf{J}_s & & & \mathbf{j} &= \mathbf{M}_\sigma\mathbf{e} + \mathbf{j}_s \end{aligned} \tag{2.41}$$

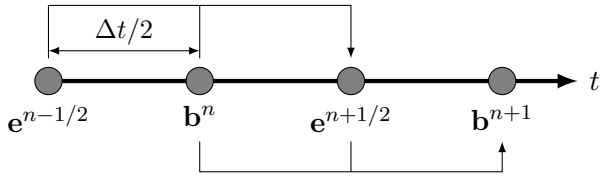

Figure 2.8: The leap-frog scheme used for time domain calculations in the FIT algorithm.

These material relations introduce inevitable numerical inaccuracy due to spatial discretization. In defining the necessary relations between voltages and fluxes, their integral values have to be approximated over the grid edges and cell areas, respectively.

Time domain calculations are implemented into the FIT algorithm by substituting the time derivatives in the MGEs by the central time differences, which results in the so-called leap-frog scheme (see figure 2.8). The time is discretized with intervals Δt and the fields are updated from previous magnetic fluxes and electric voltages, which are shifted in time by $\Delta t/2$. In other words, the electric voltages $\mathbf{e}^{n+1/2}$ are obtained at time step $n + 1/2$ from previous magnetic fluxes $\mathbf{b}^n$ and electric voltages $\mathbf{e}^{n-1/2}$:

$$\mathbf{e}^{n+1/2} = \mathbf{e}^{n-1/2} + \Delta t \mathbf{M}_\epsilon^{-1} \left(\tilde{\mathbf{C}} \mathbf{M}_\mu^{-1} \mathbf{b}^n + \mathbf{j}_s^n \right), \tag{2.42}$$

and subsequently, the magnetic fluxes are computed using $\mathbf{b}^n$ and $\mathbf{e}^{n+1/2}$:

$$\mathbf{b}^{n+1} = \mathbf{b}^n - \Delta t \mathbf{C} \mathbf{e}^{n+1/2}. \tag{2.43}$$

This method allows to calculate the evolution of arbitrary time signals, which are launched into the simulation domain. Using the grid vectors, the electric and magnetic field can be calculated at any point in time and space within the simulation volume. With the aid of the Fourier transform, the spectral characteristic of the modeled system is obtained directly from the temporal field characteristics.

Alternatively, the FIT algorithm may calculate the eigenmodes and frequencies of the simulation domain. For this purpose, the time dependence is eliminated from the MGEs by substituting time harmonic fields $\exp(-j\omega t)$. The master equation 2.25 rewritten in matrix form gives:

$$\mathbf{C} \mathbf{M}_\epsilon^{-1} \tilde{\mathbf{C}} \mathbf{h} = \mathbf{M}_\mu \mathbf{h}. \tag{2.44}$$

This technique is important to calculate band diagrams of PhCs. The eigenfrequencies are calculated at a given wave vector k, by setting the phase shift between the boundaries in propagation direction to $\varphi = ka$, hence finding the Bloch modes as defined in equation 2.26.

Chapter 3

Low dielectric contrast photonic crystals

This chapter explores possibilities to achieve full three-dimensional light confinement in resonant photonic crystal (PhC) structures (i.e. cavities) fabricated in nonlinear optical polymer slab with air holes. At the resonant frequency, the optical field is strongly localized in the cavity volume. Refractive index changes within this volume will therefore have a considerable impact on the resonator spectral characteristics, most noteworthy the resonant frequency. Integrating the resonator structures completely into the NLO-polymer intrinsically leads to maximum field interaction with the NLO-material and hence ensures the largest possible shift of the resonant frequency at a given amplitude of index modulation.

To observe a photonic band gap (PBG) in a PhC of triangular lattice of air holes in a true two-dimensional geometry (not PhC slab), a minimum contrast of 1.39:1 is required [54]. Since the available contrast with polymers is near this mark ($n_{\mathrm{poly}} \approx 1.6$), it becomes clear that the obtainable band gap size is very limited. Especially when PhC slabs are considered, where the effective index of the slab mode is always below the core material's refractive index. Additionally, in the case of PhC in slab waveguides, modes above the light line can couple to radiation modes and hence might limit the light confinement abilities of the PhC structures. This necessitates a careful design of the PhC geometry.

3.1 Resonators in periodic ridge waveguides

A PBG can be formed in a ridge waveguide that has been periodically perforated with air holes in the direction of light propagation. This geometry is comparable to one-dimensional Bragg stacks in terms of its optical properties, however it offers a higher

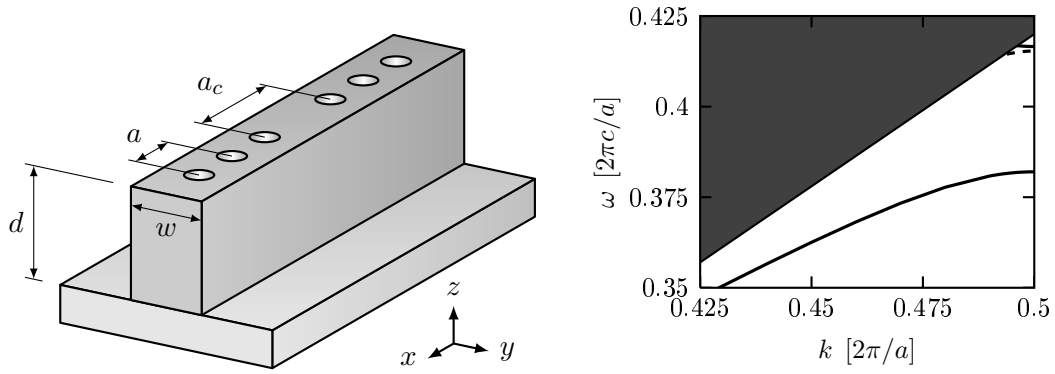

Figure 3.1: Geometry of a periodic ridge waveguide (left) and its photonic band structure (right). The PBG opens between the first two modes with even symmetry (indicated with solid lines). The dashed line represents a mode with odd symmetry.

mechanical stability than an alternating arrangement of dielectric material and air. By introducing a defect into this periodicity an allowed energy state is formed within the bandgap [63, 64]. Such a cavity makes use of the PBG effect in one direction (x) and total internal reflection in the remaining two (y and z). Resonators with $Q = 6 \cdot 10^4$ [65] and $Q = 7.5 \cdot 10^5$ [66], respectively, have been experimentally demonstrated in high refractive index contrast systems based on SOI and air bridged silicon. In the following the properties of such resonator cavities in low index systems, which use a NLO-polymer as core material are investigated.

The basic geometry of this resonator type is sketched in the left panel of figure 3.1. The right hand panel of the same figure displays the band diagram of a perfectly periodic arrangement of air holes in a low index ridge waveguide ($n = 1.54$) suspended on an ultra low index substrate ($n = 1.19$). The geometry of the ridge was chosen for single mode operation at 1.3 μm operation wavelength, with a thickness of $d = 1.35$ μm and width of $w = 0.8$ μm. The air holes have a radius of $r = 136$ nm while the lattice constant is $a = 520$ nm. This results in a relative photonic band gap of approx. 9%, centered at 1.3 μm. The dashed line in the band diagram indicates a mode with odd symmetry, which hence is orthogonal to the two modes with even symmetry (solid lines) defining the band edges of the PhC.

M. Schmidt found that linearly tapering the radii of the three air holes closest to the cavity from $r_1 = 80$ nm to $r = 136$ nm, substantially decreases vertical scattering losses. From FIT simulations, Q values exceeding 10^4 for this cavity type were obtained. Thus they are potential candidates for electro-optic modulators, if realized in a suitable electro-optic polymer [30].

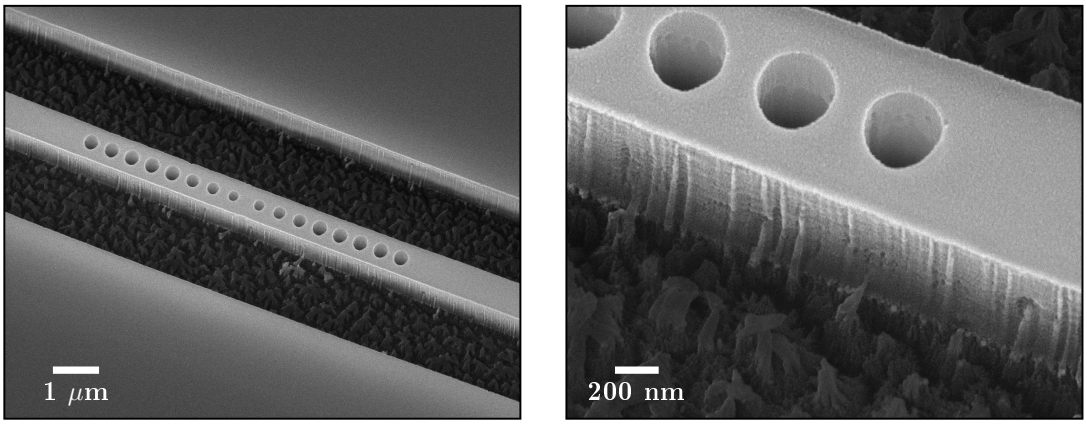

Figure 3.2: Scanning electron micrographs (SEM) displaying a PhC ridge waveguide cavity. The core is made from P(MMA/DR1), which is supported by mesoporous silica as substrate material. The magnified image on the right emphasizes surface roughness on the etched sidewall of the waveguide. The sponge-like topography of the mesoporous silica is evident in both pictures.

For experimental validation of the simulation results presented in referecnce [30], resonator structures according to the geometric features described above were fabricated. The ridge waveguides used were made from a polymer guiding layer of poly(methyl methacrylate) covalently functionalized with Disperse-Red 1 P(MMA/DR1) [67] (thickness 1.35 μm, $n = 1.54$ at 1300 nm excitation wavelength). The polymer was deposited by standard spin coating technique on a low index substrate mesoporous silica material (thickness 1 μm, $n = 1.19$ at 1300 nm excitation wavelength). To facilitate handling and ensure mechanical stability silicon wafers (thickness 0.54 mm) were used as substrate. The patterning of the ridge waveguide and photonic crystal structure were carried out at the *Institute for Photonic Technology Jena*. On top of the NLO-polymer a 50 nm NiCr-film is deposited and subsequently a 300 nm layer of PMMA electron beam resist. The pattern is written into the top layer using standard electron beam lithography (EBL). After development of the resist the structure is transferred into the NiCr hard mask by Argon ion beam etching. The patterned NiCr layer then served as an etch mask for an electron cyclotron resonance high-density plasma etching process to define the structure in the NLO-polymer layer. A detailed description of the fabrication process can be found in references [68] and [69]. The holes were etched into the core material (etching depth 1.5 μm), with a slight penetration of the substrate layer.

Scanning electron micrograph (SEM) pictures of the structures are presented in figure 3.2. The sponge-like topography of the mesoporous silica substrate is well visible in these pictures. The high air content within the pores is responsible for the extremely low

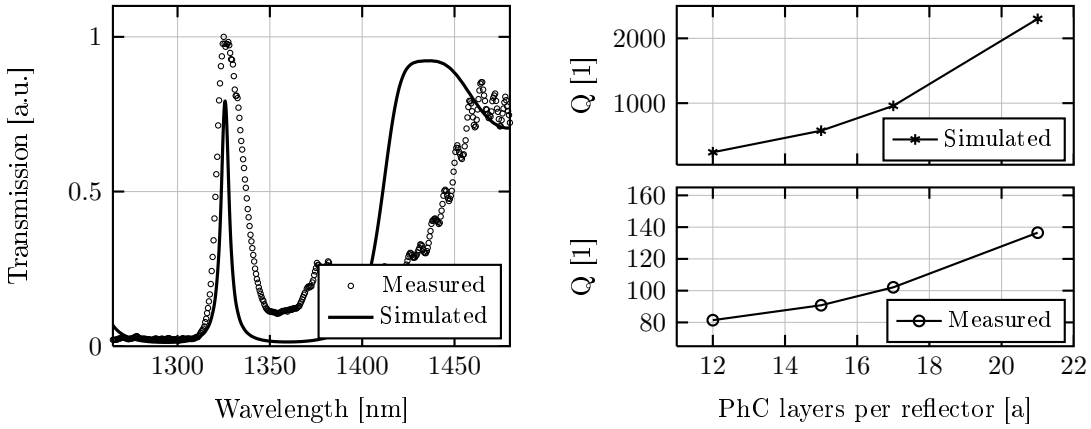

Figure 3.3: Left: Simulated (solid line) and experimental (dots) transmission spectra of a polymer PhC ridge waveguide cavity. The three innermost hole radii are linearly tapered from $r_1 = 80$ nm to $r = 136$ nm. The PBG mirrors of the resonator were 17 lattice constants in length. The simulated data was red shifted by 22 nm. Right: Simulated and experimental Q values of a polymer PhC ridge waveguide.

refractive index of this material.

The optical properties of these structures were characterized using the prism coupling technique. Tunable laser sources in the wavelength range of 1260 to 1495 nm served as light source. The proper plane of polarization for the TE polarized mode was selected by a Glan polarizer, before coupling to the waveguide. The out coupled light was detected by a standard Ge-diode. The spectrum was scanned in 0.5 nm steps.

The transmission characteristic match the results from FIT simulations (figure 3.3). The relative spectral position of the dielectric band edge and the resonance are in good agreement. The air band edge lies outside the scanning range of the laser sources and hence is not visible in the transmission spectrum. However, the difference in spectral width of the resonance between simulation and experiment is significant.

The experimental quality factors of the fabricated samples with various PBG mirror lengths are compared to those obtained from FIT simulations in figure 3.3. The quality factors found in experiments deviate significantly from the predicted simulation results. Even though the Q rises rise with each length increment of PBG mirrors in the experiment, the increase is much less than expected from the numeric simulations. The difference in the sample with 21 layers of PhC mirrors is more than one order of magnitude ($Q_{\mathrm{sim}} \approx 2300$ against $Q_{\mathrm{exp}} \approx 130$). The significantly lower Q values result from additional losses present in the system, which are not modeled by the numeric simulation. Most noteworthy are vertical scattering losses due to fabrication imperfections. Using the

relation $Q_{\mathrm{exp}}^{-1} = Q_{\mathrm{sim}}^{-1} + Q_{\mathrm{loss}}^{-1}$, these scattering losses are found to be $Q_{\mathrm{loss}} = 140 \pm 15$ for all measured samples. In figure 3.2, side wall roughness as well as imperfect hole placement and hole shape are visible, which are limiting the value of Q_{loss}^{-1}, resulting in the low total Q factor. Such low quality figures are insufficient for the application in effective broadband modulation schemes. Further substantial improvement in the fabrication technology is necessary before this type of structure in low refractive index material will be interesting for the application envisioned here.

The electron beam lithography used to define the geometry pattern here is essentially the same process, which is used to pattern structures in high index materials, where placement accuracies below 2 nm were achieved [70, 71]. However, the etching process and behavior of organic materials is different from semiconductors and not yet as well understood [68]. Consequently, the structure quality in terms of side wall roughness and vertical uniformity could be improved with an optimized etching process. In high refractive index structures, experimental Q factors above 10^5 were reported [65, 66] indicating that the lossy Q factor in structures with optimized fabrication processes is at least on this order of magnitude. Thus, resonators in periodically patterned low index ridge waveguides could achieve the quality factors predicted from simulations ($Q_{\mathrm{sim}} > 10^4$ in [30]) if fabricated in an optimized process with significantly reduced geometrical imperfections.

3.2 Omnidirectional photonic bandgap

In this section, the existence of a complete PBG in a polymer structure is theoretically shown and experimentally proven. Kee et al. showed that polymer slabs immersed in air with a triangular array of holes can, in theory, exhibit a complete PBG for TE polarization [72]. Since in such air-bridge structures, a major part of the waveguide does not rest on a solid substrate, they are intrinsically mechanically unstable and it is particularly difficult when a dielectric access channel is to be attached to the PBG defect waveguide. In the approach presented here, the polymer core is not suspended in air, an "air-like" substrate material with a refractive index close to unity is used ($n_{\mathrm{sub}} = 1.15$ at 1300 nm). Mesoporous silica is such a material due to its air filling fraction of 70% [73]. Using this substrate instead of air offers two advantages: An additional wet etching step after structuring the waveguide core is not needed and the PhC slab has a good mechanical stability residing on a solid substrate.

The GME method was used to calculate the photonic band diagram of the PhC slab structure [57]. The structure is not vertically symmetric, however, following the argumentation in [74] the modes can still be distinguished into TE- and TM-like. In order to

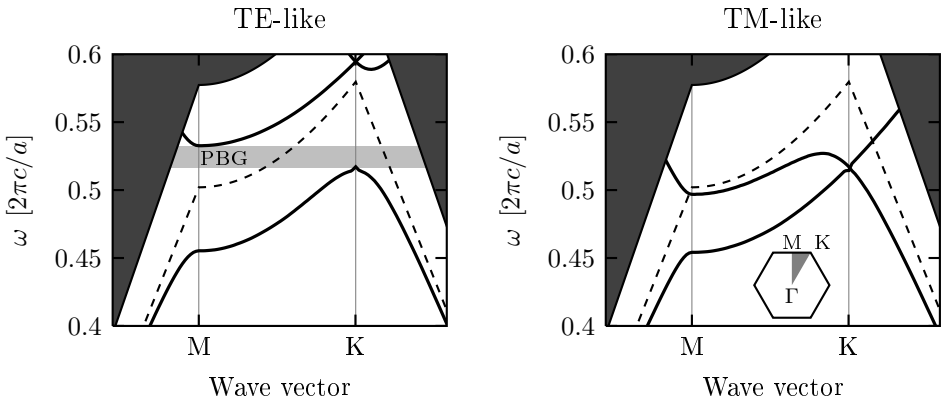

Figure 3.4: Band diagram of a triangular photonic crystal of air holes in a polymer ($n_{\text{poly}} = 1.54$) slab waveguide suspended on an air-like mesoporous silica material ($n = 1.15$) for TE-like (left) and TM-like (right) polarizations. An omni-directional PBG is visible for TE-like polarized modes (left). The air light cone is represented by the shaded region. The substrate light line is marked by the dashed line.

identify the TE- and TM-like polarized modes, the field profiles of the 3D calculation to the results of 2D calculations of the corresponding polarizations were compared. The resulting band diagram is shown in figure 3.4. This figure reveals the existence of a complete in-plane band gap for TE-like polarized modes between 0.51 and 0.53 c/a. However, it becomes apparent that considerable parts of this band gap are above the light line of the substrate (dashed line), which implies that modes with frequencies above the air band edge of the band gap can couple to radiation modes propagating inside the substrate. Usually, it is desired to have the PBG as far below the light line as possible below the light line, since otherwise the life time and, hence, the propagation distance of potential defect modes can be significantly reduced by this coupling mechanism. As shown previously, this problem can be avoided by etching away the PhC underlying substrate material, thereby removing the substrate material and creating an air-bridge structure [75]. Under etched waveguide structures are undesired for the reasons mentioned above. Below it will be shown that losses incurred from vertical radiation into the continuum of substrate modes, however, are negligible in this experiment.

From the guided mode expansion method the intrinsic radiation losses of a mode above the light line are found and described by the imaginary part $\Im(\omega)$ of the eigenmode frequency [57]. The mode is thus attenuated by $\exp(-\Im(\omega)\tau)$ per unit time τ. The propagation distance is obtained from multiplication of τ with the group velocity v_g and hence the power loss coefficient of the mode is given by $\alpha_{\text{loss}} = 2\Im(\omega)/v_g$ [76]. Calculations yielded that for this particular geometry these losses are below 1 dB/mm. Over a distance

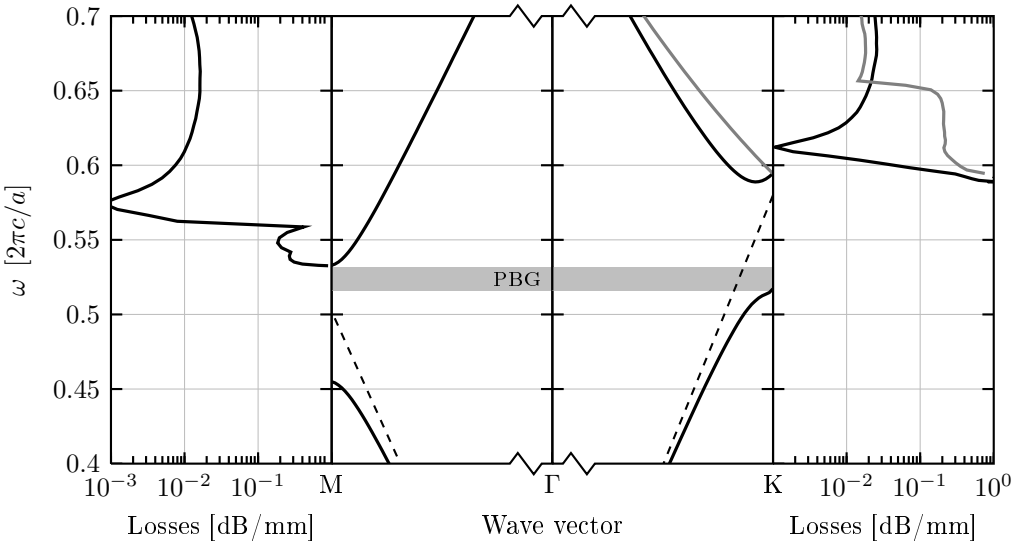

Figure 3.5: Band diagram and radiation losses of a triangular lattice photonic crystal of air holes in a polymer ($n = 1.54$) slab waveguide suspended on an air-like mesoporous silica material ($n = 1.15$) for TE-like modes in ΓM and ΓK directions. The losses of modes above the light line (gray line) due to coupling to radiation modes were calculated using the guided mode expansion method.

of a few tens (in this case 40) of lattice constants, the radiation losses are far below 1 dB and thus negligible as can be seen in figure 3.5. Therefore, the additional fabrication step of etching away the substrate material underlying the PhC was omitted.

In the next step PhC slabs were fabricated in order to experimentally confirm the existence of a complete in-plane PBG. Fabrication was carried out as described in section 3.1. Figure 3.6 shows a SEM picture of the investigated structures. The slab waveguides was made from low index substrate mesoporous silica (thickness 1 μm) and a polymer guiding layer of P(MMA/DR1) (thickness 1.5 μm). The triangular lattice was chosen to have a lattice constant of $a = 650$ nm and a hole radius of 280 nm. The bulk PhCs extended 40 lattice constants parallel to the direction of propagation and 8000 lattice constants perpendicular to it. In order to allow measurements where the light propagates in the ΓM and ΓK direction, two sets of structures were fabricated, one for each propagation direction.

To measure the transmission spectra of the structures, a measurement setup suitable to control the plane of polarization was chosen. It consisted of a white light source (100 W halogen lamp), monochromator (1/4 m, excitation wavelength range $600-2400$ nm), Glan polarizer and a Fresnel rhombus to select the desired polarization. The light was coupled in and out of the waveguide by means of prism couplers. The out coupled light was detected

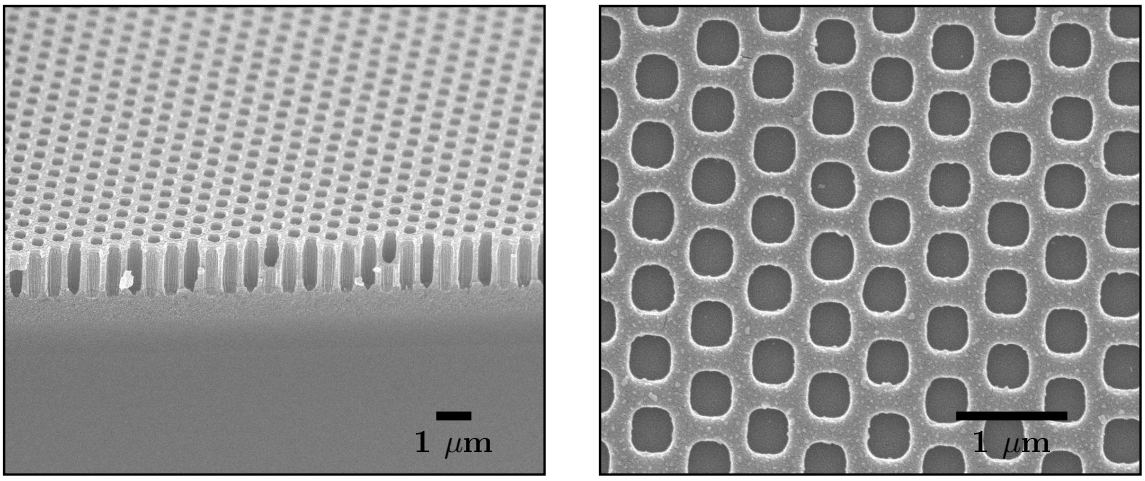

Figure 3.6: SEM displaying the cleaved edge (left) and the top view (right) of a 2D polymer triangular photonic crystal made from a P(MMA/DR1) core, with mesoporous silica as the substrate material (a = 650 nm, r = 280 nm). Holes were etched into the core material, with a slight penetration of the substrate material.

by a standard Ge-diode and registered using the lock-in technique. All transmission spectra were measured with a resolution of 2 nm in a range from $1000 - 1600$ nm. The spectra of the patterned waveguide were divided by the spectra of an unpatterned slab waveguide in order to obtain the transmission characteristic of the PhC without the influences of the waveguide material. The results of these measurements are depicted in figure 3.7, where the transmission spectra of the bulk PhC for each crystal orientation (ΓM and ΓK) are shown. In the ΓM, direction both the dielectric and air band edge (1400 and 1150 nm respectively) are easy to identify. The dielectric band edge in the ΓK direction is also apparent, whereas the air band edge is outside of the measurement range. All theses values match the results obtained from the guided mode expansion method calculations. Between 1170 and 1235 nm, a region with a signal suppression of 15 dB is clearly visible, which corresponds to the bandwidth of the omnidirectional PBG. The transient solver of CST Microwave Studio was used to calculate the expected transmission spectra. The result is plotted in Figure 3.7 and is in accordance with the experimental results.

In summary, bulk PhCs were fabricated with a triangular lattice in polymer slab waveguides on low-index air-like substrates. E-beam lithography was used and a subsequent refractive ion etching step. Band diagram calculations predicted an omnidirectional PBG for TE-like polarized modes. This prediction was confirmed by transmission measurement in the ΓM and ΓK direction of the crystal. Furthermore the experimental results are in accordance with the results obtained from FIT calculations. For future applica-

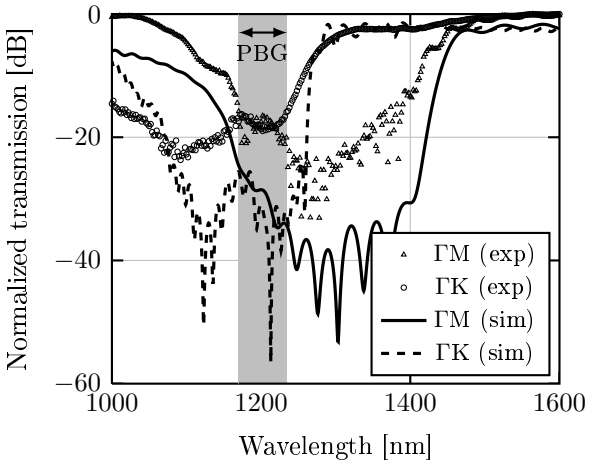

Figure 3.7: Simulated (lines) and experimental (dots) transmission spectra of a bulk 40 lattice constant triangular photonic crystal in a polymer slab waveguide. The simulated and experimental results are in excellent agreement. A band gap between 1170 and 1235 nm is clearly visible.

tions, especially resonant structures and PhC waveguides realized in polymer materials, an etching method needs to be developed, which allows the selective under etching of the PBG structure without the destabilization of the access waveguides. This is necessary in order to lift the light line completely above the PBG and avoid losses from defect modes due to coupling to radiation modes.

3.3 Microcavities in 2D low index photonic crystals

Defects can be introduced into the PhC lattice to break its translational symmetry, and hence create defect states, whose frequencies lie within the photonic band gap [54]. In a 2D PhC slab, light confinement of the microcavity is governed by distributed Bragg reflection in the slab plane and total internal reflection (TIR) perpendicular to the plane of the slab. Such resonant structures with potentially high quality (Q) factors are interesting in telecommunication applications as narrow band filters. If the resonator material is an electro-optic polymer, the optical volume and hence the resonant frequency can be shifted by modifying the polymer's refractive index. Consequently, the wavelength filter becomes tunable and can also serve as an electro-optic modulator.

Numerous geometries have been proposed to achieve extremely high Q ($> 10^6$) cavities with modal volumes on the order of one cubic wavelength in high index ($n \approx 3.5$) semiconductors [77]. Quality factor to mode volume ratios of this magnitude lead to very strong

light-matter interaction and are required to realize low threshold lasers [78], single-photon emitters [79] or compact optical buffer memories [80]. High index systems are preferred for these types of applications as they intrinsically offer better light confinement properties. However, here the PhC microcavities are to be integrated into a material system with low refractive index contrast, which naturally makes their design more challenging. At the same time, the requirements on Q factor and mode volume are slightly loosened, if the PhC cavity is to be used as a filter in a wavelength division multiplex communication scheme or as a broadband EO-modulator, as intended in this work. In the envisioned applications, mode volume is of secondary importance since a strongly enhanced light matter interaction is not necessary. For filter applications Q values of $12 \cdot 10^3$ are sufficient (see also section 2.3) and EO-modulators with $Q > 10^4$ prohibit modulation speeds in the GHz frequency range due to the photon lifetime in the cavity [30].

In this section, three different PhC microcavity designs are presented and their geometry optimized in terms of Q factor. Finally, an analysis will be carried out to determine the intrinsic limitations of PhC microcavities in low refractive index contrast environments.

3.3.1 H1 and L3 cavities

Among the most thoroughly studied microcavity types are the so called H1 and L3 cavities. An H1 cavity is formed by omitting a single hole in an hexagonal lattice, whereas the L3 cavity is formed by omitting three holes in the ΓK direction (see figure 3.8). In silicon based systems, Q factors of several 10^5 have been obtained with such cavities by appropriate engineering of the lattice geometry (hole position and radius) in immediate vicinity of the cavity [81, 82, 83, 84, 85].

In general, the quality factor of a cavity is determined by its losses, i.e. the photon lifetime inside the cavity. If the cavity material itself is assumed lossless, the only two remaining loss mechanisms are radiation losses perpendicular to the slab plane ($Q_\perp$) and in-plane losses due to energy leakage through a finite number of PhC layers ($Q_{||}$). The total Q can be expressed as:

$$\frac{1}{Q} = \frac{1}{Q_\perp} + \frac{1}{Q_{||}} \tag{3.1}$$

If the number of surrounding PhC layers is made sufficiently large $Q_{||} \to \infty$ and the total Q is determined by the radiation losses only, this value is also referred to as the intrinsic or unloaded Q factor of a cavity. Only the intrinsic quality factors ($Q_\perp$) of defect structures in low index PhC slabs are presented and discussed in this section and hence the subscript $\perp$ is dropped here.

The radiation losses of PhC slab microcavities arise from k-vector components of the

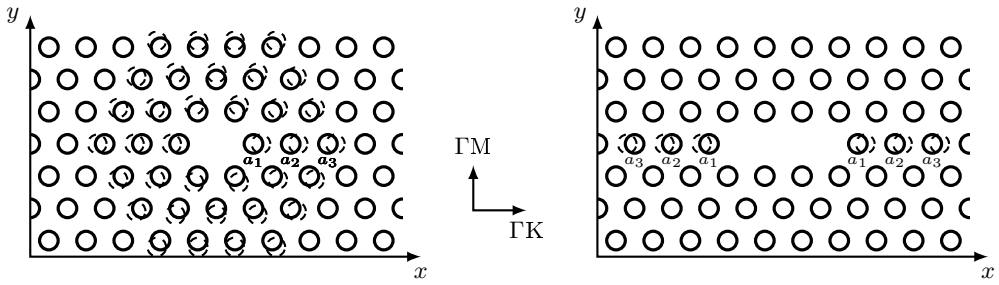

Figure 3.8: Schematic layout of the H1 (left) and L3 (right) cavities. The dashed circles indicate which holes have been shifted relative to their original position.

cavity mode, which violate the total internal reflection condition. This leaky region is determined by the in-plane k-vectors ($k_{||}$), which satisfy the condition:

$$\left|k_{||}\right| \leq k_{\text{leak}} = \frac{\omega_0}{c} \tag{3.2}$$

where ω_0 is the angular frequency of the resonant mode and c is the speed of light in the cladding material. The field distribution in k-space is connected to the optical field distribution in real space through the spatial Fourier transform. This property is exploited in the referenced works above to optimize the Q factor. By modifying the dielectric function in space, the distribution of the optical field is also altered. Hence, by proper choice of the geometry parameters, the k-vector components in the leaky region can be minimized. The details of this theory will be discussed thoroughly in section 3.3.3.

In the following, the effect of lattice geometry modifications on the quality factor of H1 and L3 cavities in low index contrast PhC are studied. Adawi et al. [86] performed such a study by shifting the innermost hole (a_1 in figure 3.8) of a L3 cavity. They found that the influence on the Q in a low index contrast PhC is more than an order of magnitude lower than a comparable variation in a semiconductor system with high index contrast. However, Akahane et al. showed in [84] that in high index contrast PhC slabs, the structural tuning of the second and third row of holes has a strong impact (factor 3) on the quality factor of a PhC cavity. Thus, the influences of the positions and geometries of the second and third nearest neighboring holes are investigated and discussed in the following.

Obviously, if one was to modify every individual hole in terms of displacement and radius, the degrees of freedom approach infinity. Here, parameter space scans were performed to study the effect of displacement of the first three hexagons of air hole layers of the H1 cavity and the displacement of the nearest three holes in ΓK direction of the L3 cavity (a_1, a_2 and a_3 in figure 3.8). Following the approach in [84], the parameter

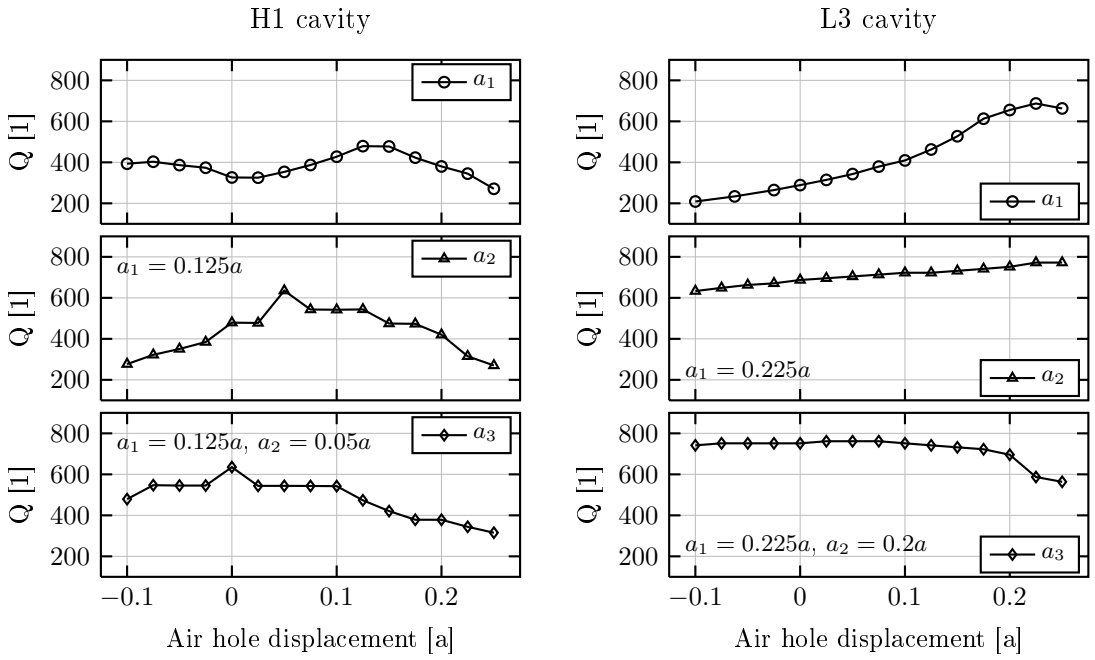

Figure 3.9: Cavity Q factors obtained numerically for H1 and L3 cavities in low index PhC

sweeps were carried out incrementally for each parameter. Therefore, not the full parameter space was scanned, but the optimal position of the first parameter was determined before optimizing the second parameter, while keeping the first at its optimal value and so on. This incremental procedure does not necessarily yield the highest possible Q factor of the PhC cavity. However, this method was chosen to keep the computational effort within limits. A full scan of all possible parameter permutations would have required an unfeasible amount of computing time. A rigorous analytical method to optimize the Q factor of a PhC cavity in low index slabs will be presented in section 3.3.3

The simulations were carried out using the transient solver of CST Microwave Studio. The bulk lattice parameters were lattice constant $a = 650$ nm, air hole radius $r = 0.34a$, slab thickness $h = a$ and slab refractive index $n = 1.6$. The structure is assumed to be air-bridged, hence the cladding and substrate index is unity. The quality factor was calculated using the full-width-half-maximum (FWHM) criterion taken from the frequency spectrum recorded by a field probe located inside the cavity. The cavity was surrounded by 20 layers of air holes, which was found to be sufficient to eliminate the contribution of in-plane losses to the total Q. A larger simulation volume did not increase the quality factor and hence the Q is determined by radiation losses only.

The results in figure 3.9, evidence that indeed the modification of the lattice geometry surrounding the cavity improves the intrinsic Q factor from initially ~ 300 to almost 800

in both cases. However, this value is still one order of magnitude below the required value for efficient EO-modulators.

3.3.2 Double heterostructure cavity

The highest reported simulated ($Q \sim 10^9$ [87]) and experimentally ($Q > 10^6$ [14]) achieved Q factors in PhC microcavities are based on photonic double heterostructures [77]. In these geometries, the microcavity is formed by joining PhC defect waveguides with slightly different longitudinal lattice constants. The change in lattice constants shifts the frequency of the defect mode. As a result, a mode gap is opened between the sections of the PhC waveguides and photons with a specific frequency can exist only in the cavity region (see figure 3.10). When the waveguide with the cavity lattice constant is short enough, the frequencies that photons can take in this region become quantized and a photonic microcavity is formed.

In the waveguide direction, the confinement is achieved by the mode gap effect and is not caused by the band gap effect due to the periodic variation of the dielectric function. This leads to an exponential decay of the envelope function of the optical field outside the cavity in ΓK direction. Proper choice of lattice constants along the waveguide allow the approximation of an Gaussian envelope function for the field profile of the resonant mode and hence an extremely reduced amount of k-vector components inside the leaky region, explaining the enormous reported Q values.

Using the same geometry parameters for the PhC lattice and simulation techniques as described in the previous section, Q factors of a double heterostructure cavity in low refractive index contrast PhC were investigated. The lattice constant in the cavity region was chosen to be $a_{\text{cav}} = 660$ nm and $a_{\text{cav}} = 655$ nm, respectively. The Q values computed to be $Q(a_{\text{cav}} = 660 \text{ nm}) \approx 1500$ and with $Q(a_{\text{cav}} = 655 \text{ nm}) \approx 2500$. Compared to the results from the H1 and L3 cavities, this is a more than two fold increase. However, in high index contrast systems, the introduction of double heterostructure cavities has led to a more than one order of magnitude increase in quality factor. In the next section, the origin of these dramatic differences in photon confinement in low and high index systems are analyzed.

3.3.3 Limits of low index contrast microcavities

It is intuitively clear that integrated optical systems with high index contrast offer better light confinement capabilities than low index systems. Therefore, the results of the previous section might not be unexpected. However, the observations do not answer the

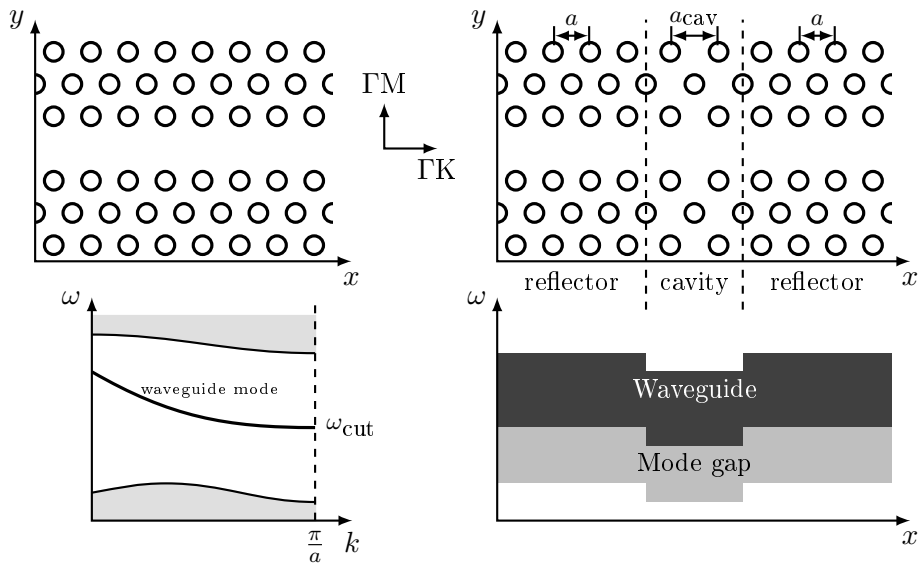

Figure 3.10: Schematic layout of a PhC waveguide (upper left) and its typical band structure (lower left). The double heterostructure is formed by changing the longitudinal lattice constant in the desired cavity region (upper right). Band structure along the ΓK direction of the waveguide (lower right). Photons with specific frequency can only exist in the cavity waveguide [14].

question whether there is a general upper limit to the achievable Q factor of a PhC cavity in a low index contrast system.

In an ideal isolated PhC cavity, as in the cases described above, the only loss mechanism is vertical scattering determined by those in-plane k-vector components, which violate the total internal reflection condition given in equation 3.2. Srinivasan and Painter therefore suggested the simple rule to minimize the optical field components in k-space to achieve high Q values in 2D PhC slab cavities [88, 89]. Furthermore, Englund et al. derived an expression that relates the total radiated power from the cavity to the 2D Fourier transforms (denoted by $\mathcal{F}_2$) of the electric and magnetic field distributions in a surface just above the slab [90]. They express the radiated power with:

$$P \approx \frac{\eta}{2\lambda^2 k} \int_{k_{||} \leq k_{\text{leak}}} \frac{dk_x dk_y}{k_{||}^2} k_z \left[\frac{1}{\eta} |\mathcal{F}_2\{E_z\}|^2 + |\mathcal{F}_2\{H_z\}|^2 \right], \tag{3.3}$$

where $\vec{k}_{||} = (k_x, k_y)$ and $\vec{k}_z$ are the in-plane and out-of-plane k-components respectively. Furthermore, $\eta = \sqrt{\mu_0/\epsilon_0}$, λ is the mode wavelength in air and E_z and H_z are the vector components of the electric and magnetic field perpendicular to the plane of the slab. In the case of TE-modes, only the optical field (E_x, E_y, H_z) are unequal to zero at the slab center, hence for such modes the term $|\mathcal{F}_2\{H_z\}|^2$ will be dominant just above the slab

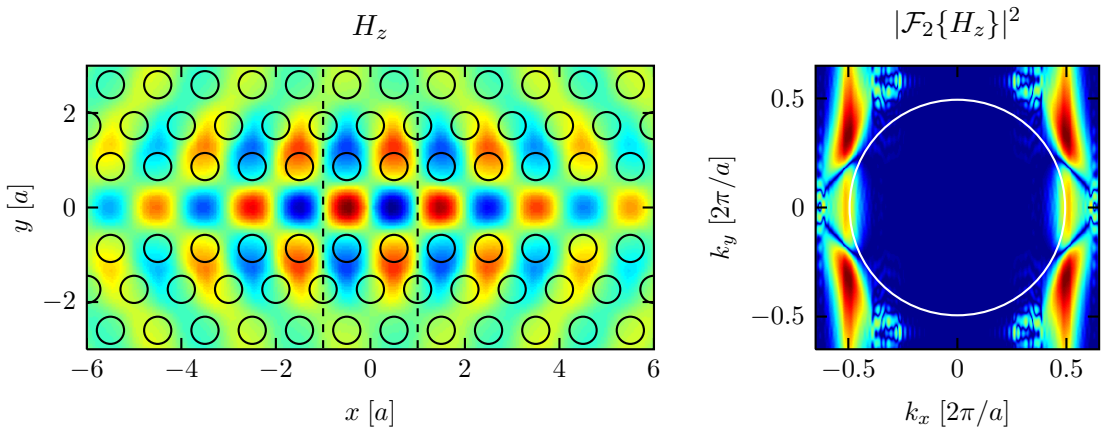

Figure 3.11: H_z field profile of the resonant mode in a double heterostructure PhC cavity in polymer (left). Fourier space representation of the H_z field component just above the slab (right). Both representations are in false color with logarithmic scaling. The leaky region is indicated by the white circle.

surface, and $|\mathcal{F}_2\{E_z\}|^2$ can be neglected in the analysis of the radiation loss above). Since Q is defined as the ratio of energy stored in the cavity U and energy lost per optical cycle P:

$$Q \equiv \omega_0 \frac{U}{P}, \tag{3.4}$$

it becomes clear that the quality of a cavity can be optimized by proper engineering of the k-space distribution of H_z.

Theoretically, it is possible to start from a desired field distribution in k-space, deduce the field distribution in real space by Fourier transform and then find a function of the dielectric constant in space $\epsilon(\mathbf{r})$, which satisfies these conditions. In practice, however, the rigorous approach of momentum space design is not practicable as it may lead to impractical values in the dielectric function (e.g. negative) or with today's technology unachievable distributions of ϵ in space.

Here, the theory of momentum space design is used to investigate the feasibility of high-Q cavities in low index polymers. To understand the difficulty of high-Q in low index compared to high index materials, it is helpful to consider the case of a double heterostructure cavity (section 3.3.2). Following the argumentation in [90, 91], the resonance frequency ω_0 of the cavity mode is given by the cut-off frequency of the PhC defect waveguide mode and the maxima $\mathbf{k}_0$ of the mode distribution in k-space is given by the edge points of the first Brillouin zone of the hexagonal lattice. Hence $k_{0x} = \pm\frac{\pi}{a}$ in ΓK and $k_{0y} = \pm\frac{2\pi}{\sqrt{3}a}$ in ΓM direction.

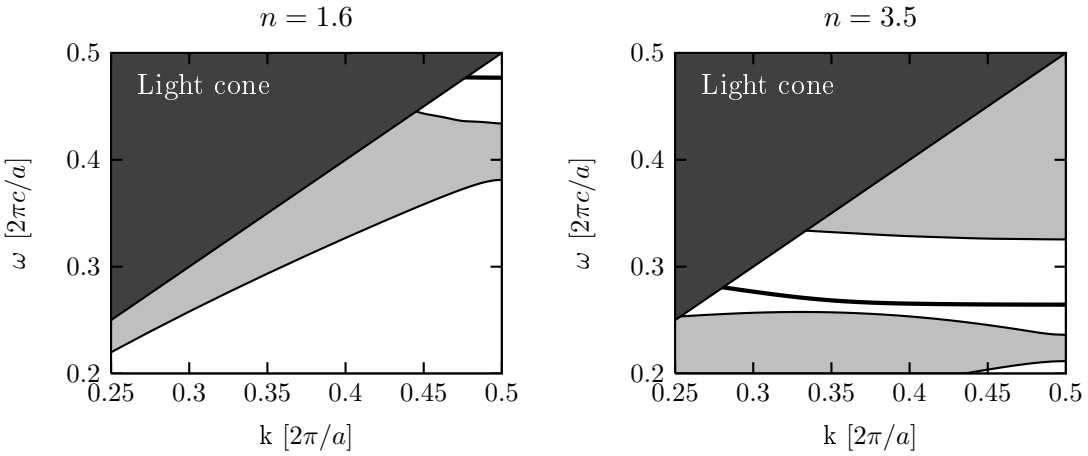

Figure 3.12: Band diagrams of W1.0 PhC defect waveguides in high index and low index materials. The defect mode is represented by the thick black line. The bulk PhC modes are indicated by the lightly shaded regions and the continuum of modes above the light line is marked by the dark shaded region.

Figure 3.11 displays a typical field distribution in real and wave vector space of the vertical component of the magnetic field of a PhC double heterostructure resonant mode just above the slab. The k-space field profile unveils that the majority of the field components within the leaky region are oriented along the k_x axis. It is therefore reasonable to reduce the complexity of the problem to one dimension and focus on the mode shape in x direction only to understand the difficulty of achieving high Q values in low refractive index PhC cavities. To tackle the problem analytically the envelope shape in x direction will be approximated by a Gaussian function with a width of σ. The approximation with a Gaussian envelope function is justified under the condition to find an upper estimate of Q. H_z is then given by:

$$H_z(x) = \frac{1}{\sqrt{\sqrt{\pi}\sigma}} \exp\left[-\frac{1}{2}\left(\frac{x}{\sigma}\right)^2\right] \cos(k_{0x}x) \tag{3.5}$$

in real space and the Fourier transform $\mathcal{F}\{H_z\}$ gives the k-space distribution:

$$\mathcal{F}\{H_z\} = \sqrt{\frac{\sigma}{\sqrt{\pi}}}\left(\exp\left[-\frac{1}{2}\left(\sigma(k-k_{0x})\right)^2\right] + \exp\left[-\frac{1}{2}\left(\sigma(k+k_{0x})\right)^2\right]\right). \tag{3.6}$$

The prefactor is needed to keep the mode energy, which is proportional to $\int_{-\infty}^{\infty} |H_z|^2 dx$ constant.

Figure 3.12 shows the band diagrams of a PhC defect waveguide formed by omitting one row of holes in the ΓK direction in a low index ($n = 1.6$) and a high index ($n = 3.5$) core material, respectively. From the location of the cut-off frequency of the defect mode,

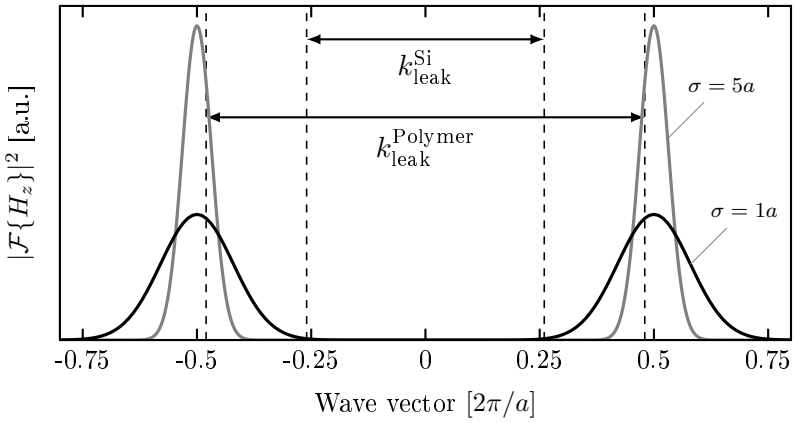

Figure 3.13: Profile of a resonant mode with Gaussian envelope function in momentum space

it is obvious that the resonant frequency of a cavity in the low index material ($\omega_0 \approx 0.48$) will be substantially higher than in the high index material ($\omega_0 \approx 0.26$), resulting in a substantially increased leaky region of wave vector components in the low index case. Figure 3.13 gives an impression of the massive increase of the integral over k within the leaky region if extension of the mode in x direction is assumed to be equal for the low and high index cases.

To compensate for the increased leaky region, the width of the mode profile in momentum space needs to be reduced. Figure 3.13 shows how an increase in σ leads to narrower profile in k-space, while increasing its maximum value due to conversation of energy. By evaluating the integral over the wave vector components in the leaky region, one finds that the result decreases monotonously with increasing mode width σ. Thus, theoretically, the Q value of a low index PhC cavity could indeed be driven to arbitrarily large Q factors by increasing the mode volume and maintaining a Gaussian envelope profile. Tanaka et al. [87] derived a design rule of multistep PhC heterostructures in high index waveguide cores to achieve a Gaussian envelope profile of the resonator mode with an arbitrary width in the ΓK direction. It should be noted that this method can be arbitrarily demanding on the fabrication quality and the achievable quality facotor is hence principally limited by the placement accuracy of the PhC holes. Here, this concept is adopted to low index PhC cores and the associated limits on the Q factor will be discussed.

Multistep heterostructures

The general geometry of a multistep heterostructure is displayed in figure 3.14. Through modification of the properties (i.e. lattice constant, radius, waveguide width, etc.) of

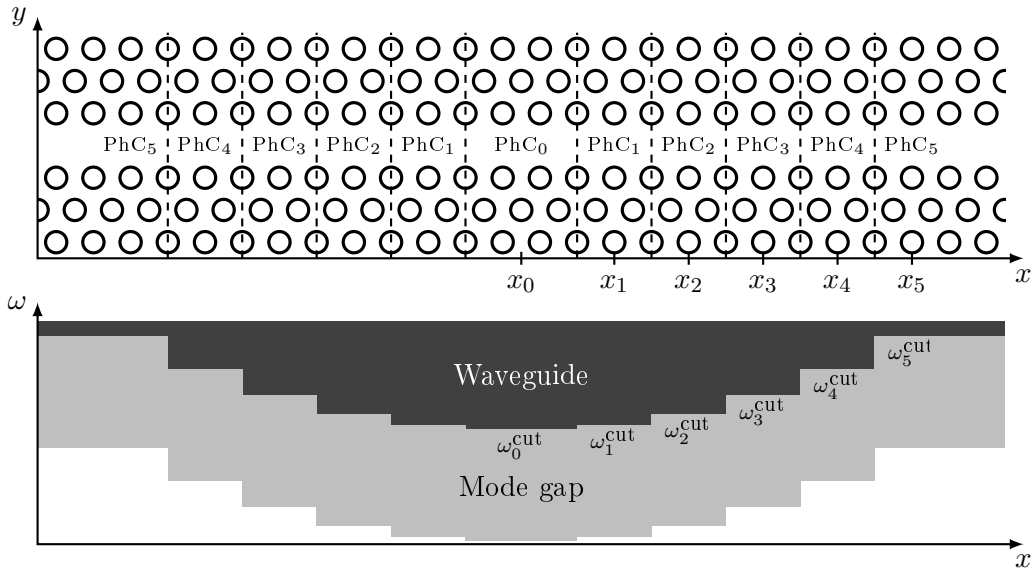

Figure 3.14: Schematic geometry (top) and band structure (bottom) of a multistep PhC heterostructure cavity.

each PhC section $\mathrm{PhC_n}$, the cut-off frequency is modulated along the direction of the waveguide. It will be shown in the following that by appropriate selection of the spatial cut-off frequency distribution, the desired Gaussian field envelope of the cavity mode can be achieved.

In a standard heterostructure cavity as displayed in figure 3.10, the evanescent behavior of the field in the reflector region is determined by the imaginary part of the complex wave vector, which is denoted with $\Im(k) = q$. The field decays exponentially with:

$$H \propto \exp(-qx), \tag{3.7}$$

where q is the imaginary part of the wave vector within the modegap at the resonance frequency ω_0. However, for a Gaussian envelope the magnetic field should adhere to:

$$H \propto \exp\left(-\frac{1}{2}\frac{x^2}{\sigma^2}\right). \tag{3.8}$$

From equations 3.7 and 3.8 it becomes clear that q needs to be a linear function in the spatial coordinate x and hence:

$$q = \frac{x}{2\sigma^2}. \tag{3.9}$$

The complex dispersion relation of the PhC waveguide can be found with the analytic continuation method [92]. With this method, the real dispersion relation of the PhC mode is expanded into its complex form. Assuming the real part of the dispersion relation is known (either from the plane wave or guide wave expansion method), the function $f(k)$

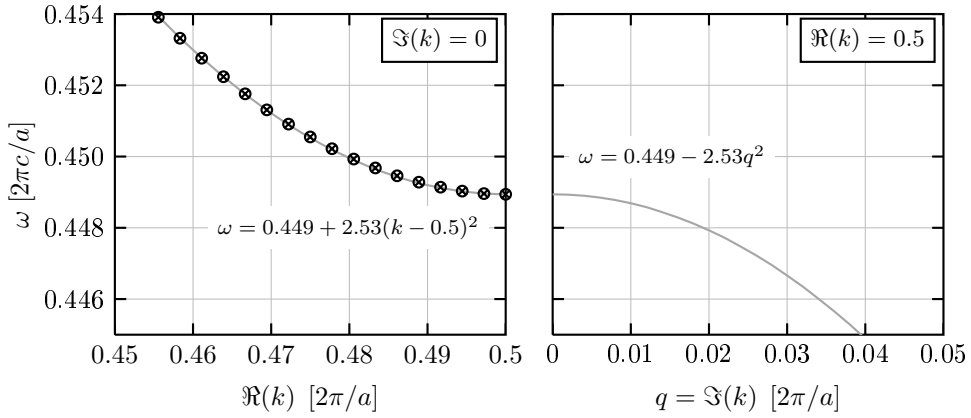

Figure 3.15: Complex dispersion relation of a W0.7 polymer PhC waveguide. The symbols indicate the results from the band diagram calculation using the plane wave expansion method. The gray lines plot the result of a second order polynomial fit.

can be fitted by a Taylor expansion of the term $(k - 0.5)$ at the Brillouin zone boundary $(k = 0.5)$. Due to the even symmetry of the dispersion relation around this point, only even order terms need to be considered in the expansion:

$$\omega = \omega^{\text{cut}} + C_1 \cdot (k - 0.5)^2 + C_2 \cdot (k - 0.5)^4 + C_3 \cdot (k - 0.5)^6 + ... \tag{3.10}$$

Substituting $k = 0.5 - iq$ yields the dispersion in the mode gap region:

$$\omega = \omega^{\text{cut}} - C_1 \cdot q^2 + C_2 \cdot q^4 - C_3 \cdot q^6 + ... \tag{3.11}$$

The knowledge of the complex dispersion relation of the waveguide mode allows for an analytic design of the multistep heterostructure cavity. Inserting the cavity resonance frequency ω^{cav} and equation 3.9 into the previous expression and rearrangement yield the required spatial dependency of the cut-off frequency in the reflecting section of the heterostructure:

$$\omega^{\text{cut}}(x) = \omega^{\text{cav}} + C_1 \left(\frac{x}{2\sigma^2}\right)^2 - C_2 \left(\frac{x}{2\sigma^2}\right)^4 + C_3 \left(\frac{x}{2\sigma^2}\right)^6 - ... \tag{3.12}$$

Thus equation 3.12 gives the required distribution of the cut-off frequency along the PhC waveguide shown in figure 3.14.

A polymer PhC waveguide with a defect width $W = 0.7\sqrt{3}a$ yields a dispersion relation of the defect mode that is well approximated by a second order Taylor expansion (see figure 3.15). This waveguide type is chosen to simplify the derivation of the necessary geometry variations. The operating frequency of a PhC is inversely proportional to its lattice constant. The cut-off frequency can therefore be tuned locally by adjusting the

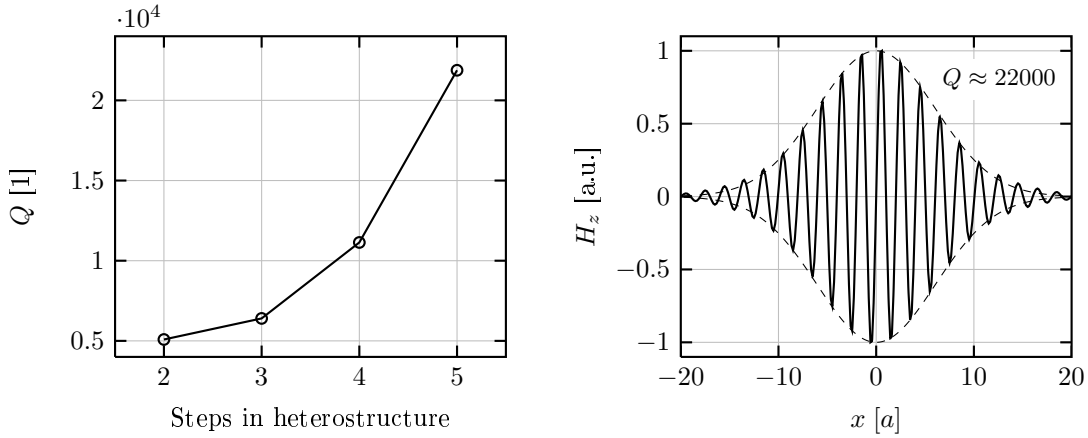

Figure 3.16: The quality factor of a multistep heterostructure increases drastically with an increase in transition steps (left). Optical field $|H_z|$ distribution in a multistep heterostructure, the dashed lines indicate a fitted Gaussian envelope function to the simulation results (right).

lattice constant in the respective PhC section according to:

$$\omega^{\text{cut}}(x)a(x) = \omega_0^{\text{cut}} a_0. \tag{3.13}$$

Together with equation 3.12, this gives a rule for the required spatial dependence of the lattice constant:

$$a(x) = \frac{a_0}{1 + C_1 x^2/(4\sigma^4 \omega_0^{\text{cut}})}. \tag{3.14}$$

As long as $C_1 x^2/(4\sigma^4\omega_0^{\text{cut}}) \ll 1$ is satisfied, this can be simplified to:

$$a(x) = a_0 \left(1 - C_1 x^2/(4\sigma^4 \omega_0^{\text{cut}})\right). \tag{3.15}$$

As indicated in figure 3.14, the lattice parameters are changed stepwise rather than continuously and thus the distances x_m are approximated using:

$$x_m = (2m + 0.5)a_0. \tag{3.16}$$

Yielding for the lattice constant in each section:

$$a_m = a_0 \left(1 - C_1 (2m + 0.5)^2 a_0^2/(4\sigma^4 \omega_0^{\text{cut}})\right). \tag{3.17}$$

This design rule is applied to fine tune a PhC heterostrucutre with cavity lattice constant $a_0 = 660$ nm and bulk lattice constant $a = 650$ nm using between 2 and 5 transition steps. The results are displayed in the left panel of figure 3.16. Using more transition steps and thus achieving a smoother approximation of $a(x)$ given in equation 3.15 drastically

increases the quality factor of the cavity. The right panel of the same figure demonstrates how well the optical field envelope follows a Gaussian envelope function. However, the incremental difference in lattice constant especially of the first transition is below one nanometer. Today's nanofabrication technology allows for a placement accuracy of 2 nm or 1 nm at best and hence the actual fabrication of such structures is not feasible.

To determine an upper estimate of the realistically achievable quality factor, simulations were carried out under the boundary condition that the minimum step size between two PhC sections must not be smaller than either 1 nm or 2 nm. Due to the required parabolic dependence of a_m, the cavity lattice constant a_0 exceeds the value of 660 nm already at either 3 ($\Delta a = 2$ nm) or 4 ($\Delta a = 1$ nm) transition steps. This leads to a resonance frequency, which is below the band gap of the bulk PhC and allows the optical field to couple to PhC slab modes, giving rise to unwanted in-plane losses. Hence, the maximum number of transition steps is very limited, resulting in a maximum Q of roughly $1.3 \cdot 10^4$ in both cases. Following the argumentation of section 2.3 this value would result in an insertion loss of at least 20 dB, if the cavity is loaded to a waveguide. Clearly, this performance is not acceptable for any serious application in optical data transmission.

3.3.4 Cavity definition by photobleaching

The refractive index of polymers with electro-optic chromophores can be permanently altered by photobleaching. In this process the, π-bridges in the chromophores are broken by irradiation of high energy photons (typically in the UV) and the refractive index can be decreased by up to $\Delta n = 6 \cdot 10^{-2}$ [44, 93, 94]. The magnitude of the index change is determined by the exposure dose and can therefore be controlled by the intensity and the exposure time.

In general, the frequencies of PhC modes do not scale linearly with the refractive index of the wave guide core. However, for the variations achievable with photobleaching, which are on the order of 10^{-2}, the position of the cut-off frequency can be approximated by a linear function in refractive index. Thus, the cut-off is described as:

$$\omega^{\mathrm{cut}}(n) = \omega^{\mathrm{cut}}(n_0) + C_n(n - n_0), \tag{3.18}$$

where C_n is a constant that depends on the particular PhC geometry. Using the same argumentation as above, a condition for the spatial distribution of refractive index in x direction is found to be:

$$n(x) = n_0 - C_n' \left(\frac{x}{2\sigma^2}\right)^2. \tag{3.19}$$

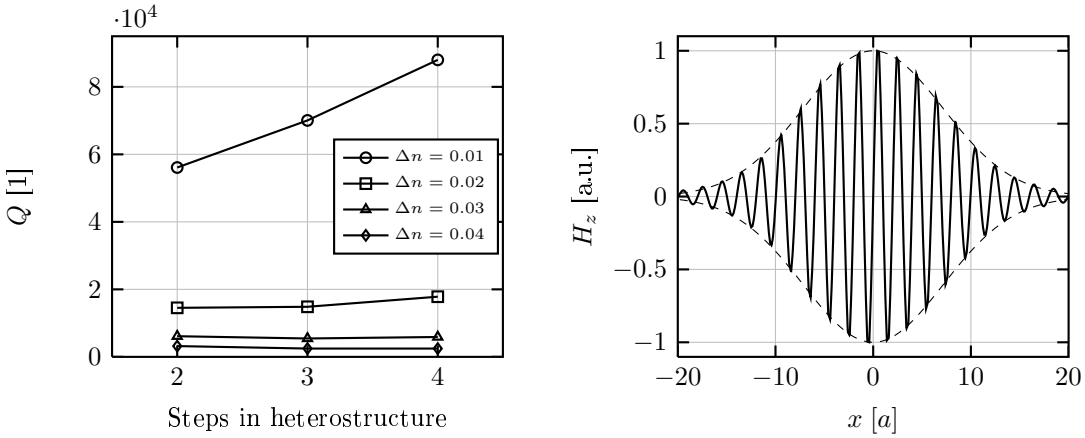

Figure 3.17: The quality factor a multistep heterostructure increases drastically with an increase in transition steps (left). Optical field in a multistep heterostructure. The dashed lines indicate a fitted Gaussian envelope function to the simulation results (right).

This theory was tested using FIT simulations completely analogous to the case discussed above. The simulation results are summarized in figure 3.17. Most noteworthy is the almost one order of magnitude increase of the quality factor to $Q \approx 9 \cdot 10^4$ compared to the geometry variation optimization presented above. Similarly to the previous results, the quality factor increases with a rising number of transition steps. The simulation results with more than 4 transition steps are not presented here because the cavity started to support a second order mode due to the increased cavity volume. The low quality factor values at larger index variations is a result of coupling to PhC slab modes equally to the case of a too large Δa explained previously. However, it becomes clear that defining multistep PhC heterostructures using photobleaching can be a very interesting alternative to overcome fabrication limitations in the positioning accuracy of today's lithography methods. The insertion loss of the loaded resonator would amount to 1.3 dB, which might still be acceptable for application in some optical transmission systems.

3.4 Conclusion

In summary, possibilities of full three-dimensional light confinement in PhC nano cavities using low dielectric contrast materials were evaluated. Cavities in periodically structured ridge waveguides were fabricated using a polymer material as the waveguide core. The performance of these resonating cavities observed in experiments ($Q_{\mathrm{exp}} \approx 10^2$) was more than order of magnitude poorer than predicted from simulations. This deficiency was attributed to fabrication imperfections. Assuming that the same fabrication quality of to-

day's semiconductor technology can be achieved in polymer based PhC ridge waveguides, cavities with loaded Q above 10^4 are feasible.

An omnidirectional PBG with gap to mid-gap ratio of $\approx 5\%$ for TE polarized light in a polymer slab waveguide was experimentally demonstrated. Based on these results, the achievable performance of H1, L3 and double heterostructure type PhC nanocavities in low refractive index material was numerically studied by systematic geometry variations. The H1 and L3 type cavities, which employ light confinement by Bragg scattering in both in-plane directions, the intrinsic quality factor did not exceed 10^3. The double heterostructure, where light confinement is based on the mode gap effect in one in-plane direction and Bragg scattering in the other, a $Q_\perp = 2500$ was possible. PhC nano cavities in low refractive index contrast cavities suffer from the intrinsic disadvantage of a resonance much closer to the air light line compared to the same structures in high dielectric materials. Theoretically, it is possible to achieve arbitrarily high intrinsic Q factors also in low refractive index PhC cavities by increasing the mode volume, while maintaining a Gaussian envelope function of the resonant mode's optical field. However, this would require an arbitrarily fine (sub nanometer) positioning accuracy of the fabrication technology. With the placement accuracy of today's microstructuring technology, theoretic Q values of up to $\approx 10^4$ are possible. However, according to the argumentation in section 2.3, the intrinsic Q factor should be on the order of 10^5 for an EO-modulator device. To circumvent these strong requirements on placement accuracy, photobleaching of the NLO-polymer material can be used to define a multistep heterostructure type cavity. This option theoretically allows for the fabrication of PhC nano cavities with quality factors of almost 10^5. The highest reported experimental quality factors of silicon PhC slab cavities exceed 10^6 [14, 70]. Therefore, it can be assumed that the simulated Q factors of 10^5 in low index PhC cavities are confirmed experimentally, if fabricated with the same quality as the high index structures.

Chapter 4

High dielectric contrast hybrid silicon-organic photonic crystals

This chapter analyzes the possibilities of EO-modulation in 2D PhC slab components, whose core is silicon ($n_{\text{core}} = 3.5$) and completely surrounded by NLO-polymer ($n_{\text{poly}} \approx 1.6$). The high refractive index of the core offers stronger light confinement, compared to the situation described in the previous chapter, thus reducing the component's geometric footprint. Furthermore, it enables access to very mature silicon nano fabrication processes. The disadvantageous lack of an intrinsic Pockels effect is mitigated by infiltrating the silicon PhC structure with second order NLO-polymer. The modulation of the background material's index is translated into a modulation of the *effective* index of the complete device. This effect is optimized by careful structure design and maximizing the integral of the optical field in the EO-active regions.

4.1 Photonic bandgap in infiltrated systems

The impact of the waveguide core's refractive index on the position of the PBG of a 2D PhC was briefly illustrated in section 3.3.3 and figure 3.12. Infiltrating the holes of a silicon based PhC slab with a dielectric material, gives rise to a new situation. The effects on the properties of the PhC shall be discussed in the following in detail. As in the previous chapter, the discussion is restricted to TE polarization.

The left hand panel in figure 4.1 shows the relative gap size of a 2D PhC with a triangular lattice of lower index holes in a high index material as a function of the hole radius r. The relative gap size is defined as the gap-midgap ratio $\Delta\omega/\omega_c$, where $\Delta\omega$ is the width of the PBG and ω_c is its center frequency. Displayed are curves for various core indices with air holes. The case of a silicon core with polymer filled holes is marked by the

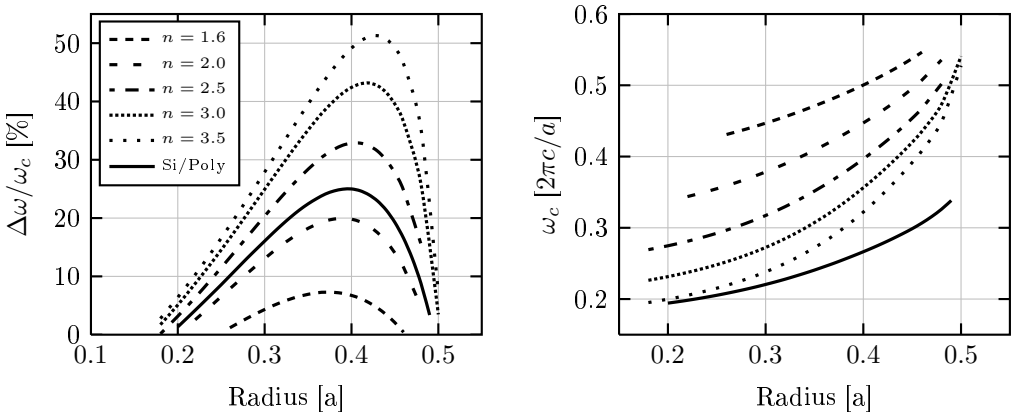

Figure 4.1: Relative PBG size (left) and PBG center frequency (right) as a function of hole radius. The relative gap size rises with the ratio of $n_{\text{core}}/n_{\text{hole}}$, while the position of the gap is decreasing with increasing effective refractive index.

solid line, since it is of particular interest here. The relative gap size is a monotonously increasing function of the ratio of the core refractive index to the hole index [54]. This ratio is, in the case of a hybrid silicon-organic PhC:

$$\frac{n_{\text{Si}}}{n_{\text{poly}}} = \frac{3.5}{1.6} \approx 2.19, \tag{4.1}$$

resulting in a relative gap size of 25%, which is about half the value of silicon with air holes, however, more than 4 times the value of polymer with air holes.

The center frequency of the gap decreases in frequency as the average refractive index of the medium increases as depicted in the right panel of figure 4.1. This is not surprising as the frequency of a mode scales with $1/n$ in a medium with refractive index n [54]. The solid line again represents the hybrid silicon-organic PhC. It is clear that its average index is higher than the silicon perforated with air holes. From the discussion in the previous chapter it is known that a reduction in the PBG center frequency is beneficial for PhC devices as it increases the mode region below the light cone and hence keeps vertical losses low. However, in this case the light cone is shifted to lower frequencies as well, because the cladding material is not air but polymer. Figure 4.2 illustrates the band diagrams of 2D PhC slabs in three different scenarios: polymer slab with air holes and cladding (left), silicon slab with air holes and cladding (middle), and silicon slab with polymer holes and cladding. Obviously, the polymer cladding has significantly reduced the light cone frequency, almost offsetting the advantage of a reduced PBG frequency.

In PhC slabs, the slab thickness d affects the gap size and position as well and thus needs to be considered in the design. Figure 4.3 shows the gap size and position for a set of slab thicknesses and hole radii. Slabs where $d/a > 0.7$ are not considered as the

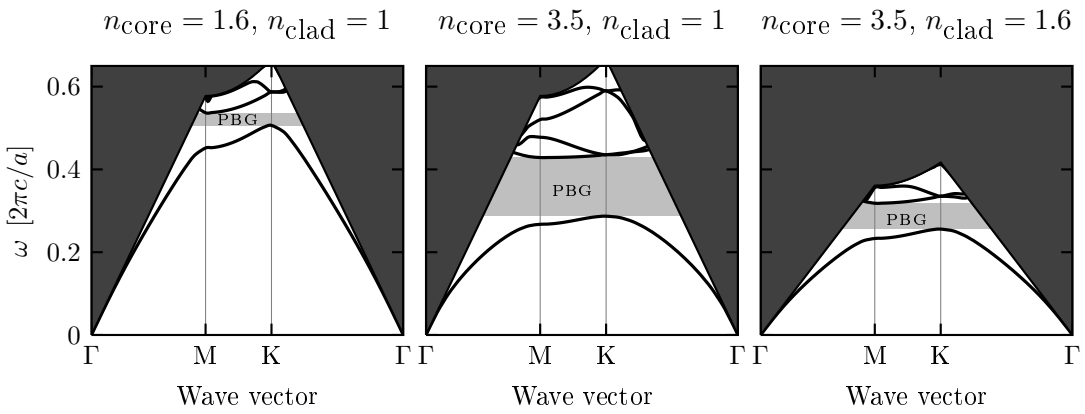

Figure 4.2: Photonic bands diagrams of the TE polarization in 2D PhC slabs with triangular lattice and hole radius $r/a = 0.36$ made of polymer core material (left, slab thickness $d/a = 1.0$), silicon core material (middle, $d/a = 0.5$) and silicon core with polymer filling material (right, $d/a = 0.7$). The band gap increases with increasing index contrast and the center frequency decreases with increasing core index.

waveguide then sustains more than one vertical mode, leading to a closing of the PBG. For the rest of this chapter, a radius of $0.3a$ is chosen. Even though this does not yield the maximum gap size, it is considered to be a good trade off to keep the gap far enough below the light line, while obtaining a sufficient gap size. Furthermore, it reduces the requirements on the lithography and etching process, keeping the minimum structure size of the remaining silicon above 100 nm. To have the PBG located at $\lambda = 1550$ nm, the lattice constant is $a = 410$ nm. The SOI substrates available have a thickness of 220 nm, consequently its ratio to the lattice constant is 0.52.

4.2 Photonic crystal waveguides and resonators

With the knowledge of the bulk properties of a PhC in a hybrid silicon-organic environment, this section evaluates the possibilities of using a microcavity resonator as an EO-modulator in this material composition. Chapter 3 demonstrated that the best resonator performance in terms of spectral line width and mode volume is obtained from PhC heterostructures.

For proper resonator design the properties of the defect waveguide's modes are required. The optimal performance in a heterostructure cavity is expected from a defect mode that is farthest from the light line. This criterion is best satisfied by the defect mode of a $W = 1.1$ waveguide (see figure 4.4), however a resonator mode in a heterostructure with $\Delta a = 5$ nm could couple to bulk PhC modes and would hence be lossy. Therefore, the

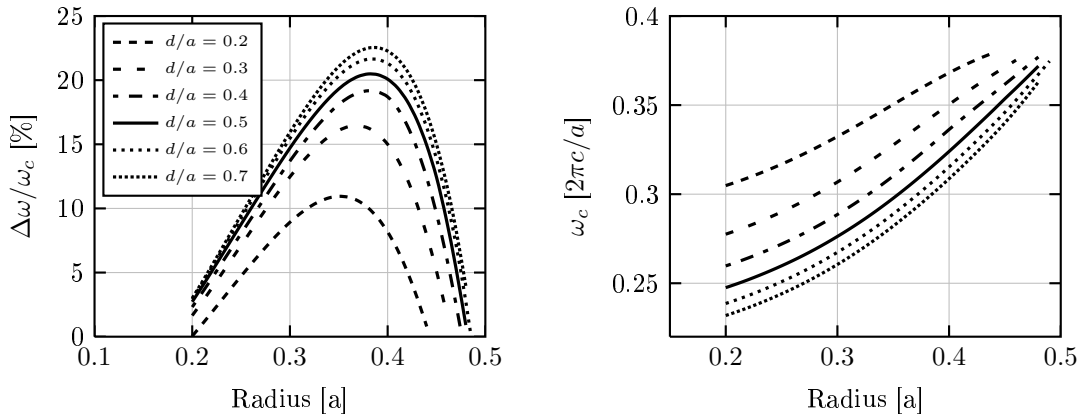

Figure 4.3: Relative PBG size (left) and PBG center frequency (right) as a function of hole radius and slab thickness.

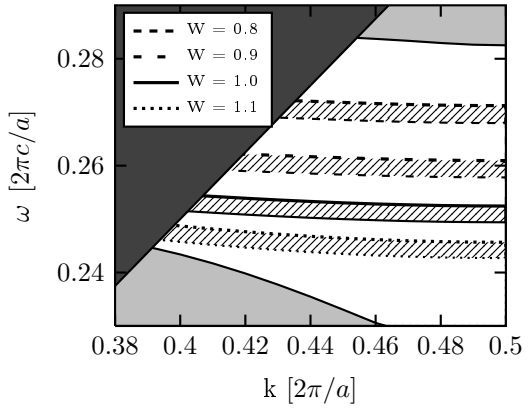

Figure 4.4: Defect modes of a line defect waveguide in hybrid silicon-organic material ($r/a = 0.3$, $a = 410$ nm). The patterned regions indicate the mode gap between two waveguides where $\Delta a = 5$ nm.

$W = 1.0$ waveguide is considered to be the better option to form a high Q resonator.

Numerical simulations of a PhC double heterostructure design in hybrid silicon-organic material yielded intrinsic quality factors of $7 \cdot 10^4$ ($a_{\text{cav}} = 420$ nm) and even $1.7 \cdot 10^5$ ($a_{\text{cav}} = 415$ nm) for a two lattice constant long cavity. This is more than an order of magnitude increase as compared to the similar design in a purely organic PhC and would fulfill the requirements for an EO-modulator (section 2.3). Using the method of a multistep heterostructure could improve the Q value even further.

Even though this structure offers sufficient resonant properties, it is not well suited for efficient EO-modulators, which will be shown in the following. From simulations, where the cladding refractive index has been incremented by $\Delta n = 10^{-3}$, it is found that the resonance shifts by $\Delta\lambda_0 = 0.169$ nm. The refractive index of the NLO-polymer cladding

can be varied by applying a voltage to metal electrodes, which need to be located above and below the cladding. The required modulation field strength can be calculated from:

$$\Delta n = \frac{1}{2} n_{\text{poly}}^3 r_{13} E_{\text{mod}}. \tag{4.2}$$

Due to the anisotropy of the second order nonlinearity and the perpendicular orientation of the optical field in TE polarization to the modulation field, the coefficient r_{13} is used. As explained in section 2.1, this means the effective EO-coefficient is reduced to at least one third of its value, compared to the case when the electric modulation field and the optical electric field are parallel.

The electric modulation field induced in the polymer by a potential difference V_{mod} between the electrodes is given by:

$$E_{\text{mod}} = \frac{\epsilon_{\text{Si}} V_{\text{mod}}}{\epsilon_{\text{Si}} d_{\text{poly}} + \epsilon_{\text{poly}} d_{\text{Si}}}. \tag{4.3}$$

For simplicity, the silicon is assumed to be a solid, perfect dielectric. Assuming a cladding thickness of 1 μm above and below the slab, and a state of the art NLO-polymer with $r_{33} = 150$ pm/V, the modulation voltage computes to be 20 V to achieve a spectral shift of $\Delta\lambda_0 = 0.169$ nm. In other words, the FWHM switching voltage of a $Q = 10^4$ resonator would be 20 V in this geometry, which is far above the anticipated 1 V. The poor performance of this device is attributed to three factors:

- Relatively wide electrode spacing, which is necessary to avoid additional optical losses,
- Limited optical field energy in the NLO-material,
- Perpendicular orientation of optical field and modulation field.

In the next section, the slotted photonic crystal waveguide is introduced, which mitigates all three issues.

4.3 Slotted photonic crystal waveguides and resonators

The conceptual structure of the EO-modulator device, which will be discussed and analyzed in this section, is presented in figure 4.5. The device is again based on a resonant PhC double heterostructure waveguide. To enhance the nonlinear interaction of the electric modulation field and the optical mode, a narrow slot is introduced in the middle of the PhC defect waveguide. Almeida et al. showed that a slot on the scale of hundred

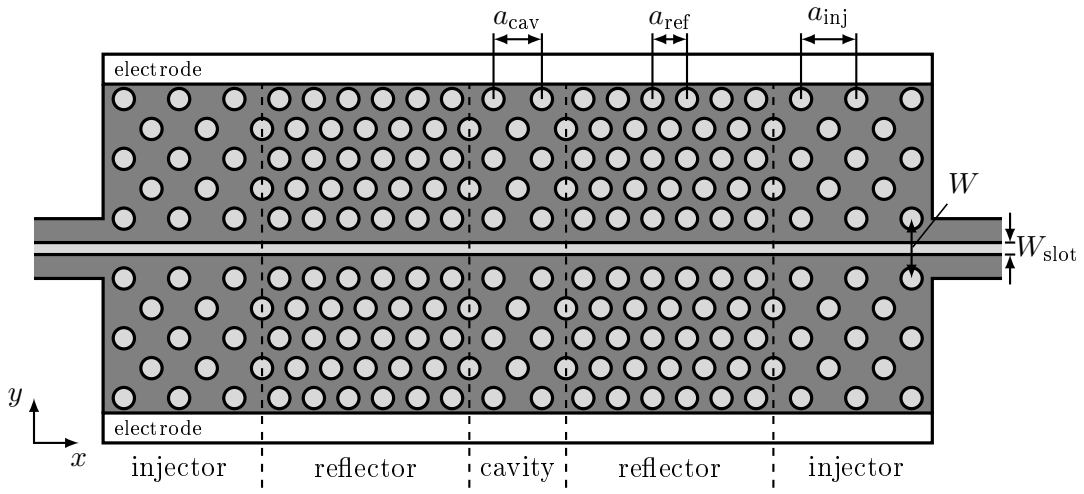

Figure 4.5: Schematic of the proposed slotted PhC waveguide heterostructure modulator. The resonator is defined by the cavity region and the reflector, in-plane light confined is achieved by the mode gap effect. To facilitate coupling to the cavity, an injector section between reflector and the slotted ridge waveguide is designed. The stripe electrodes are placed alongside the PhC waveguide.

nanometers leads to an enhancement of the perpendicularly polarized optical field (i.e. TE polarization) in the slot region, due to the discontinuity of the refractive index and the merging of the evanescent tails of the mode inside the polymer region [95]. The modulation signal is applied to metal electrodes placed alongside the PhC, thus generating an electrical field across the slot. Due to the small dimensions of the slot, the required voltages are by more than an order of magnitude smaller at any given field strength than in the case of the sandwich electrode configuration in the previous situation. Furthermore, the dominating optical field component E_y is oriented parallel to the modulation field, thus making more efficient use of the anisotropy of the Pockels effect in NLO-polymers. Baehr-Jones et al. used this field enhancement in an EO-polymer filled slotted silicon waveguide to achieve EO-modulation with below 1 V switching voltages in a classical Mach-Zehnder geometry, however with a rather large geometric footprint (arm lengths of 2 cm) and time constants above 1 ms [96].

The resonant cavity design presented here enables large modulation depths while, at the same time, maintaining an ultra compact geometrical footprint. Both aspects are optimally accounted for in a heterostructure type photonic crystal cavity, as these devices have the highest reported Q values with a minimal modal volume [91]. The heterostructure is formed by joining PhC waveguides with slightly different lattice constants. The cavity section has a larger lattice constant ($a_{\mathrm{cav}} > a$) compared to the reflector section ($a_{\mathrm{ref}} =$

a) to create a mode gap between the sections and confine light in the cavity region. By creating a heterostructure cavity using a slotted PhC waveguide filled with a NLO-polymer, it is possible to shift the position of the resonance peak in the frequency spectrum via modulation of the refractive index of the NLO-polymer by means of an external electric field. As will be shown in section 4.3.2 this can be done with a considerably reduced voltage, than in the unslotted case of the previous section. The PhC in this design offers the two fold functionality of being optically shielding and electrically conducting at the same time, thus allowing the modulation field to be applied to the electro-optical polymer inside the slotted region while keeping the optical field from reaching the contacting metal electrodes and introducing additional losses. The injector section between the reflectors and the slotted waveguide is used to facilitate coupling from the slot waveguide mode to the Bloch mode of the slotted PhC waveguide. Its effect will be discussed in section 4.3.2.

4.3.1 Unloaded resonator performance

In this section, the design and performance of the unloaded PhC heterostructure resonator, i.e. without access waveguides, is considered. Figure 4.6 shows the band structure of a slotted PhC waveguide of silicon ($n_{\mathrm{Si}} = 3.5$) embedded in polymer material ($n_{\mathrm{poly}} = 1.6$). The geometry parameters are chosen to be: lattice constant $a = 410$ nm, radius $r = 0.3a$, waveguide width $W = 1.4\sqrt{3}a$, slot width $W_{\mathrm{slot}} = 150$ nm and slab thickness $d_{\mathrm{Si}} = 220$ nm. The parameters are based on the design proposed by Brosi et al. [97]. From the band diagram presented in figure 4.6, two defect modes are found, both with considerable field enhancement in the slotted region. The lower mode is not useful here, due to its vicinity to the dielectric band edge. Hence, the following will concentrate on the defect mode at the center of the bandgap. Narrower slot widths would create an even stronger enhancement of the electric field; however, here the above value is chosen to facilitate fabrication of the device.

By slightly increasing the lattice constant in propagation direction of the waveguide the defect mode is shifted to lower frequencies, thus creating a mode gap. This mode gap is used to form a heterostructure resonator by elongating the lattice constant in a two lattice constant long cavity section of the slotted PhC waveguide. Optical fields with frequencies within the mode gap will be trapped in this cavity region. Obviously, choosing a larger step of the lattice constant will result in a larger mode gap. Next, the influence of the difference in lattice constant of cavity and reflector on resonant behavior, namely the Q factor, will be examined.

Three-dimensional numerical simulations using CST Microwave Studio were performed

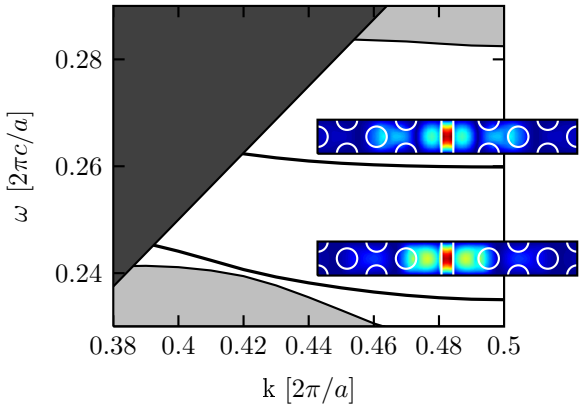

Figure 4.6: Defect modes of a slotted PhC waveguide ($W = 1.4\sqrt{3}a$, $W_{\text{slot}} = 150$ nm). The insets show the $|E_y|$ field distribution of both defect modes in the PhC slab plane at $k = \pi/a$. The field enhancement of the E_y field in the slotted region is apparent in both cases.

to calculate resonant behavior and field distributions. For all simulations, meshings with discretization fine enough such that further detailing only marginally improved the quality of the results were chosen (mesh size was typically $\lambda_{\text{mat}}/10$). The simulation volume was chosen to be 25 lattice constants lateral and 50 lattice constants along the defect waveguide. The intrinsic Q of such a cavity was compared to the penetration depth, which is the 1/e value of the optical field strength, in propagation direction of the electric field into the reflector section. The lattice constant in the cavity region a_{cav} was increased in 5 nm steps, the results are summarized in figure 4.7. The largest Q of $3.7 \cdot 10^5$ is obtained for the smallest elongation of $\Delta a = 5$ nm. However, this geometry also exhibits the largest penetration depth, which implies the necessity of a longer reflector section, thereby increasing the device footprint. Possibilities of further Q factor enhancement by virtue of multistep heterostructures and polymer bleaching are discussed in section 4.3.4.

A reduction in the intrinsic Q factor of a PhC cavity implies an increase in vertical losses due to vertical scattering. This effect is clearly observable in the field distribution in the x-z-plane (upper panel of figure 4.8). A larger step in lattice constant leads to an envelope of the electric field function, which deviates stronger from a Gaussian shape and consequently results in a decreased quality factor as already explained in section 3.3.3. To study this behavior, two-dimensional spatial Fourier transforms of the electric field distribution of the cavity mode (lower panels in figure 4.8) were performed. The white circles in the field plots indicate the leaky region into the polymer cladding ($k = n_{\text{poly}} 2\pi/\lambda_0$). For wave vector components within these regions (light cones), the total internal reflection condition is not satisfied. These k-vector components can serve as escape routes for the

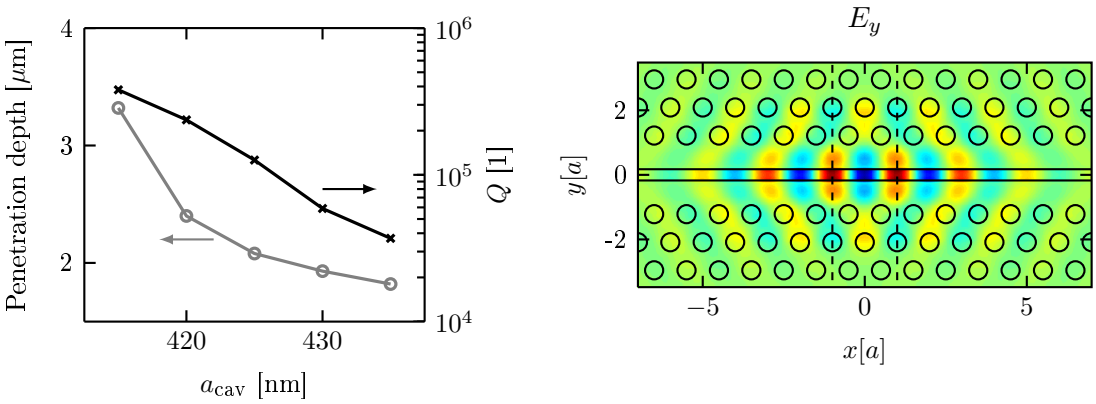

Figure 4.7: Intrinsic quality factor and penetration depth in the reflector section of the PhC heterostructure resonator as a function of cavity lattice constant (left) and the field distribution of the resonant mode (right).

optical energy and are responsible for vertical scattering. It can be seen that the lower Q heterostructures show stronger k-vector components within the light cones.

These results clearly indicate a trade-off between high Q and low penetration depth, i.e. device size, when choosing the cavity lattice constant. At the same time, a trade-off results for the free spectral range of the device and the achievable Q. The free spectral range is predisposed by the mode gap width, which itself is determined by the difference in cavity lattice constant. If a larger free spectral range is desired, a longer cavity lattice constant should be chosen, however at the expense of a reduced Q. For the remainder of this section and the next section, a cavity lattice constant of $a_{\text{cav}} = 420$ nm is considered. This results in a free spectral range of approximately 25 nm.

The intrinsic Q factors reported here are about a factor of 4 smaller compared to the slotted heterostructures reported in [98]. This is not surprising, since the cladding material here is polymer as opposed to air and leads to a larger leaky region. Consequently, more wave vector components are inside the light cone, due to the reduced refractive index contrast between cladding and core material. However, as discussed in section 2.3, this is not necessarily disadvantage a for the envisaged electro-optical modulation device, as long as the intrinsic Q is well above 10^5.

4.3.2 Injector section

To operate the proposed device in transmission, slotted ridge waveguides are added as shown in figure 4.5. A cavity with $a_{\text{cav}} = 420$ nm and reflector section with length $N_{\text{ref}} = 8a$ is considered. Simulations showed that simply butt coupling the slotted ridge

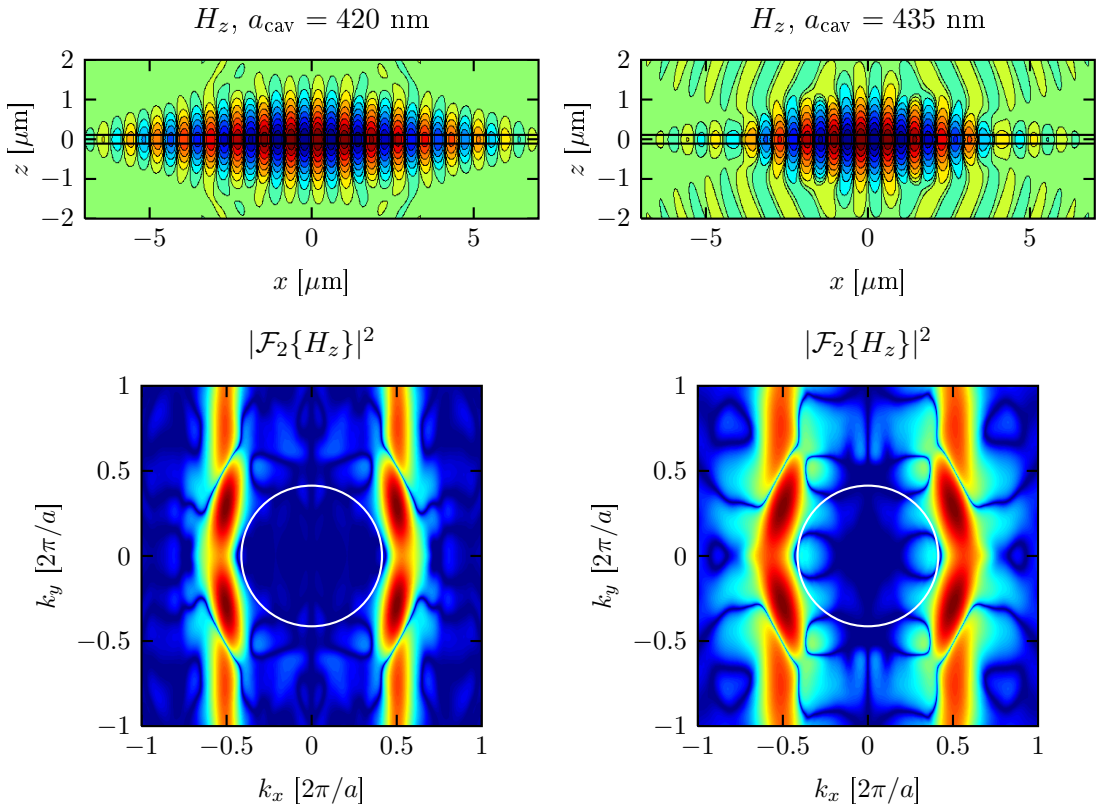

Figure 4.8: The two top panels show the real space field distribution of the H_z component at $y = 0$ in logarithmic scale. Enhanced vertical scattering at the larger cavity lattice constant a_{cav} can be observed. The two bottom panels show the k-space field distribution of the same field vector component at $z = 0$ in false color representation of identical scale. For wave vectors inside the white circle the total internal reflection condition is violated.

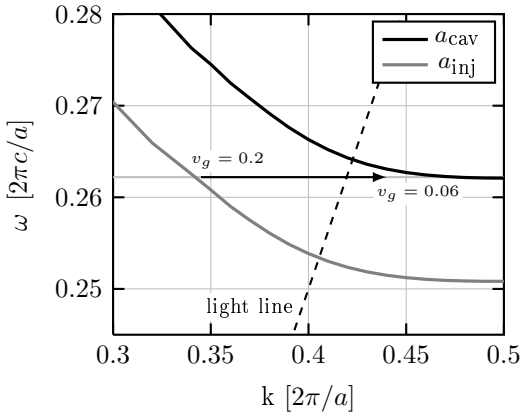

Figure 4.9: 3D band diagram of the slotted PhC waveguide defect mode. By choosing a larger lattice constant, the light at the resonance frequency (ω_{res}) is first coupled to a fast light mode of the injector section and then excites into the slow light mode of the cavity. The fast light region of the transition section is above the light cone, however, this section is just $4a_{\text{inj}}$ short.

waveguide to the PhC heterostructure waveguide results in a very high insertion loss of the device at resonance of more than -16 dB. To mitigate these insertion losses, an injector section of just four lattice constants in length was introduced between the reflector section and the ridge waveguide. In a first step, the lattice constant of this transition section was chosen to be the same as the lattice constant of the cavity region ($a_{\text{cav}} = a_{\text{inj}}$), allowing optical waves at the resonance frequency to propagate in this region. This increased the transmission to approximately -8 dB. It is reasoned that by first coupling to a Bloch mode of the PhC waveguide, optical tunneling through the reflector region to the cavity region is facilitated, which results in less vertical scattering. Hence, the maximum transmission of the resonator is increased.

However, at the resonance frequency, the defect mode of the cavity and the injector are operating in the slow light regime (figure 4.9), which causes back reflections at the interface from fast light ridge to the slow light PhC waveguide. These back reflections originate from the group velocity and thus group refractive index mismatch of the waveguides [99]. In a second step, to compensate for this effect, the defect mode of the injector is shifted to operate in the fast light regime at the resonance frequency (figure 4.9). This can be achieved by either elongating the lattice constant (a_{inj}) or widening the defect width (W_{inj}).

The transmission was increased at the resonance frequency to roughly -3 dB from initially -8 dB, demonstrating that the theory presented in [99] for standard PhC waveguides

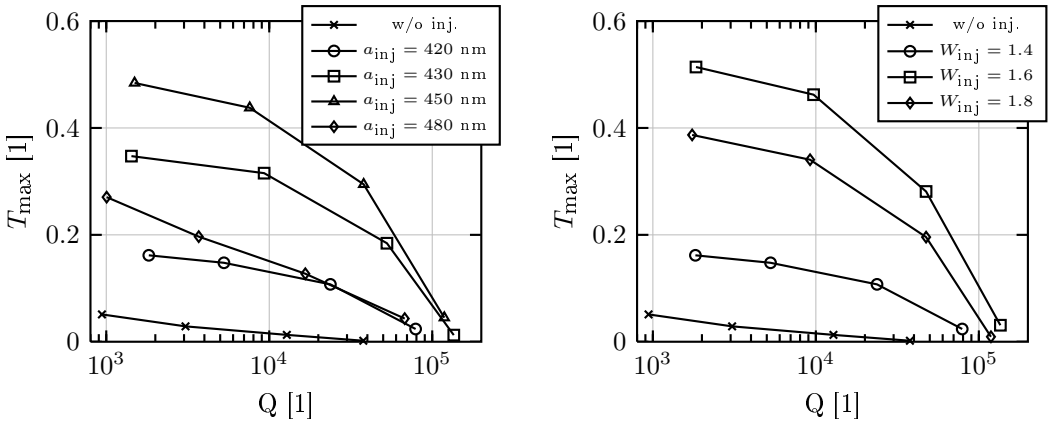

Figure 4.10: Maximum transmission vs. Q factor of in-line coupled cavities without and with an injector section of elongated lattice constants a_{inj} (left). Same plot but for increased defect width W_{inj} (right). The reflector length is varied between 8 and 14 lattice constants in both cases.

can also be applied to slotted PhC waveguides to enhance the light injection efficiency and, consequently, the transmission performance. A transition section of just four lattice constants is sufficient to achieve this improvement. It is desirable to keep this region as short as possible, not only to minimize the geometric footprint of the device, but also to avoid significant radiation losses from the injector due to operation above the light line (figure 4.9).

Naturally, in a coupled system as considered here, the total (or loaded) Q factor and maximum transmission at resonance depend on the intrinsic Q of the cavity and the coupling strength of the system. The former was discussed in the previous section and the latter is controlled by the length of the reflector region. When prolonging the length of this region, the reflectivity and the total Q of the device are increased, while the maximum transmission is decreased. Analytically, this is expressed by the following relations already presented in section 2.3:

$$\frac{1}{Q_{\text{tot}}} = \frac{1}{Q_{||}} + \frac{1}{Q_{\perp}} \quad \text{and} \quad T_{\max} = \left(1 - \frac{Q_{\text{tot}}}{Q_{\perp}}\right)^2, \tag{4.4}$$

where horizontal ($Q_{||}$) and vertical Q factor ($Q_{\perp}$) represent the in-plane and vertical energy decay respectively. The vertical Q is comparable to the intrinsic or unloaded Q of the cavity and the horizontal Q increases when elongating the reflector section (N_{ref}). From 4.4 it is therefore clear that at a given intrinsic (or vertical) $Q_{\perp}$, the maximum transmission has to decrease with increasing total Q.

As mentioned earlier, the defect mode band can be shifted to lower frequencies either by widening the defect width (W_{inj}) or elongating the lattice constant (a_{inj}). To compare

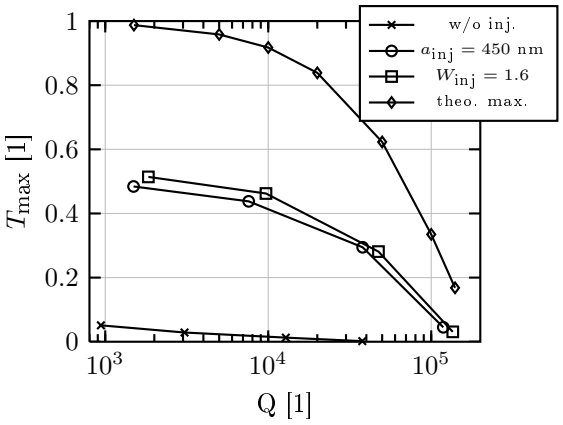

Figure 4.11: Performance of a slotted PhC heterostructure in-line coupled to a ridge waveguide without injector section, optimized injector section geometry and the theoretically expected maximum.

the effect of these different transition section geometries, device simulations for various lengths ($N_{\mathrm{ref}} = 8 \ldots 14$) of the reflector section were performed. The obtained maximum transmission values are plotted versus the total Q in figure 4.10. Clearly, the performance of the resonator shows significantly improved transmission at any given total Q with the injector section in place. Both figures of merit are optimal if either $a_{\mathrm{inj}} = 450$ nm or $W_{\mathrm{inj}} = 1.6$.

For the operation as an EO-modulator, Q factors of about 10^4 are sufficient, since the Q factor is directly proportional to the photon lifetime τ inside the resonant cavity and its resonant frequency ω_0 ($Q = \omega_0 \tau$). This leads to an upper limit to the modulation frequency of the device given by $f_{\mathrm{mod}} = \tau^{-1}$. This result emphasizes that for modulation purposes, the loaded Q factor of a cavity should not exceed 10^4 if a bandwidth of the order of 100 GHz is desired. From figure 4.10, it follows that Q values in this order of magnitude would result in a transmission of approximately -3 dB.

Figure 4.11 compares the device performance without injector section, optimized values for a_{inj} and W_{inj} as well as the theoretical maximum that can be expected from a resonator with an intrinsic Q of $2.4 \cdot 10^5$. The addition of the injector section has significantly improved the insertion loss at any given quality factor. However, the achieved performance is notably below the theoretical maximum. The insertion loss stems mainly from reflection and scattering losses at the ridge to PhC waveguide interface, due to mode profile mismatch.

To confirm that scattering losses at the waveguide to the PhC waveguide interface are indeed the origin of the discrepancy between the theoretical maximum transmission and

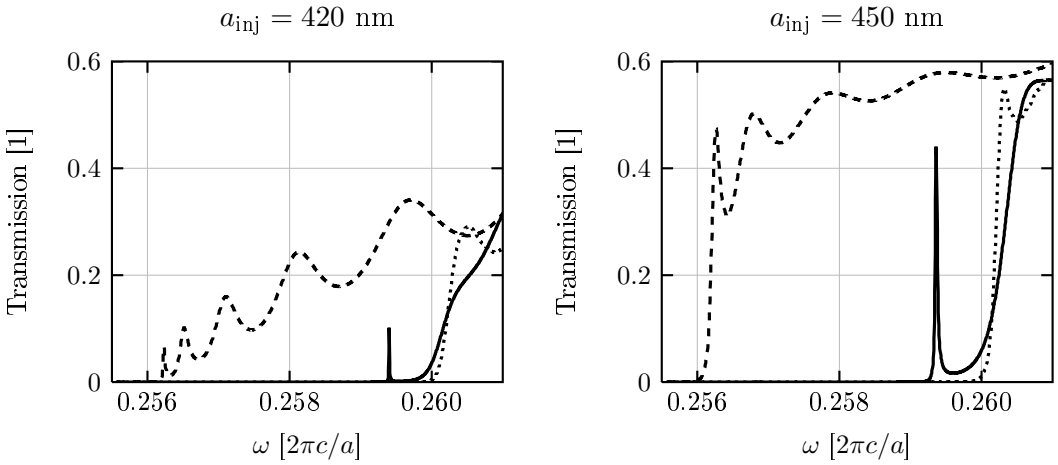

Figure 4.12: Transmission spectra through a slotted PhC heterostructure (solid line) and through slotted PhC waveguides with $a = 410$ nm (dotted line) and $a = 420$ nm (dashed line). Simulation results for structures with 420 nm injector section (left) and 450 nm injector section (right).

the values found in simulations, the transmission spectrum of the PhC heterostructure is compared to the spectra of PhC waveguides without the cavity region. Their transmission is indicated by the dashed ($a = 420$ nm) and dotted ($a = 410$ nm) lines in the graphs presented in figure 4.12. The increased overall transmission in a device with optimized injector section $a_{\mathrm{inj}} = 450$ nm is also visible for PhC waveguides. However, it is apparent that almost half of the optical power is not transmitted. Since the PhC is only 20 lattice constants long and operates below the light line, vertical losses can be neglected. Hence, almost all losses must be due to scattering at the interface of the waveguides. This scattering is an inherent problem also in the coupling of unslotted PhC waveguides to conventional waveguides, which can be mitigated by choosing an optimum interface position of the PhC, thereby minimizing the mode impedance mismatch [100, 101].

4.3.3 Sensitivity of slotted photonic crystal waveguides

Figure 4.13 shows how the transmission spectrum shifts when changing the refractive index in the slotted region of the PhC heterostructure cavity (reflector length $N_2 = 10$, $Q = 8000$). A refractive index change of $\Delta n = 10^{-3}$ results in a wavelength red shift of $\Delta\lambda = 0.12$ nm. This strong sensitivity is a result of the optical field enhancement in the slotted region (figure 4.7). The change in refractive index due to an applied electric modulation field E_{mod} is given by the known relation $\Delta n = n_{\mathrm{poly}}^3 r_{33} E/2$, where $E = V/W_{\mathrm{slot}}$ with slot width W_{slot}, applied voltage V, Pockels coefficient r_{33} and the polymer

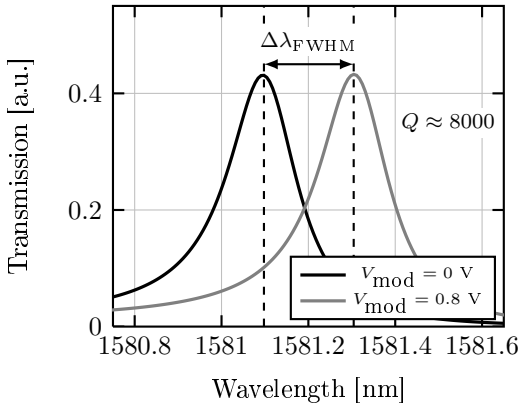

Figure 4.13: Calculated resonance spectra of heterostructure cavity in a hybrid silicon-organic PhC slab at electro-optically shifted refractive indices of the polymer slot material. The voltage required to shift the spectrum by the spectral width of the resonance is $V_{\mathrm{FWHM}} = 0.8$ V when using an electro-optically active polymer with $r_{33} = 150$ pm/V. The slight asymmetric shape of the spectrum is a consequence of the close spectral proximity of the mode gap edge at higher frequencies.

refractive index n_{poly}. To compare resonant modulator devices, it is common to use the full width half maximum voltage V_{FWHM} [102], which corresponds to the voltage needed to shift the resonance by its spectral width at half maximum intensity. By choosing a state of the art polymer material with $r_{33} = 150$ pm/V [25, 103] and using the relations given above the FWHM voltages computes to be $V_{\mathrm{FWHM}} = 0.8$ V with a quality factor $Q = 8000$.

4.3.4 Cavity definition by photobleaching

In the last section of the previous chapter, the potential of high Q cavities in gradually bleached polymer PhC slabs was discussed. The present section analyzes if this concept is also applicable to systems where the polymer cladding material is locally reduced in refractive index. However, since the silicon core material is absorbing light in the ultra violet spectrum, only the top cladding layer, the perforated region and partially the volume straight beneath the holes would be bleached, as the remaining area is shielded by the silicon. Consequently, the vertical symmetry of the PhC slab would be broken. To preserve the symmetry, an electron beam could be used to locally bleach the hole and slot areas perpendicular to the PhC plane. In other words, creating rodes with a reduced refractive index. It was shown that electron beam lithography can tune the refractive index of NLO-polymer with very high spatial precision (minimal feature size

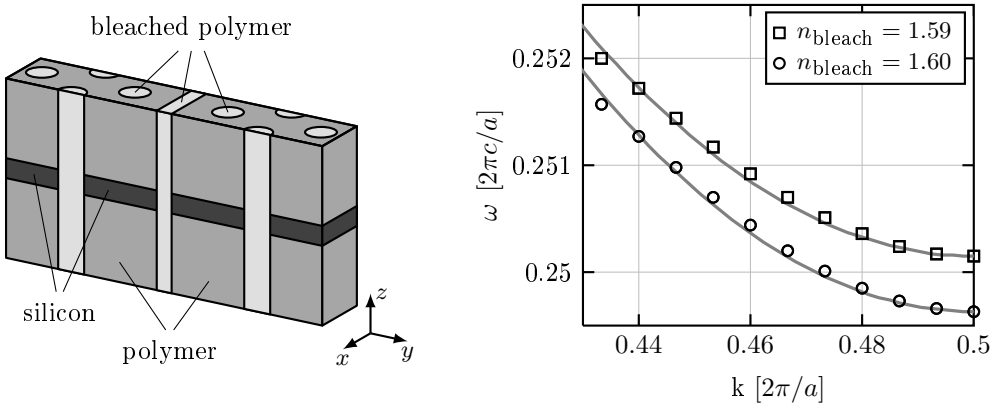

Figure 4.14: Schematic of the slotted PhC waveguide, with bleached slot and holes (left). Defect bands of a slotted PhC waveguide (symbols) and parabolic fits (gray lines) (right). Reduction of the refractive index in the indicated regions shifts the cut-off frequency by $\Delta\omega/2\pi c = 5.2 \cdot 10^{-4}$, which is equivalent to a shift in lattice constant of 2.1 nm.

below 100 nm) [94, 104]. The reduction of refractive index is controlled by the exposure dose, with a maximal achievable index change of $\Delta n = 6 \cdot 10^{-2}$.

To adopt the design principle of a parabolic refractive index distribution around the desired cavity region, the defect mode should exhibit a parabolic dispersion relation (see section 3.3.3 for details). For this reason the slot width is reduced to $W_{\text{slot}} = 100$ nm and the defect width is now $W = 1.0$, which gives a good approximation of a parabolic function in the band diagram (see figure 4.14). By reducing the refractive index by $\Delta n = 10^{-2}$ in the regions indicated in figure 4.14, the cut-off frequency of the defect mode is shifted by $\Delta\omega a/2\pi c = 5.2 \cdot 10^{-4}$, corresponding to a shift in lattice constant of 2.1 nm. In the references [94, 104] the authors report tuning precisions of $\Delta n_{\text{min}} = 2 \cdot 10^{-4}$, consequently the cut-off frequency of the PhC can be tuned with an accuracy equivalent to sub nanometer positioning of individual holes.

To test the potential of this cavity definition approach, the intrinsic Q value of such cavities were calculated using FIT simulations. The geometry parameters remained unchanged and the simulation volume spanned 80 lattice constants in propagation direction and 30 lattice constants laterally. The cavity was three lattice constants long and each transition section of the multistep heterostructure was two lattice constants wide (see also left part of figure 4.15). The total refractive index change between the cavity region and the outermost PhC is denoted by Δn and the refractive index of each transition section m is given by:

$$n_m = n_{\text{poly}} - \frac{\Delta n}{x_{\text{max}}^2} x_m^2, \tag{4.5}$$

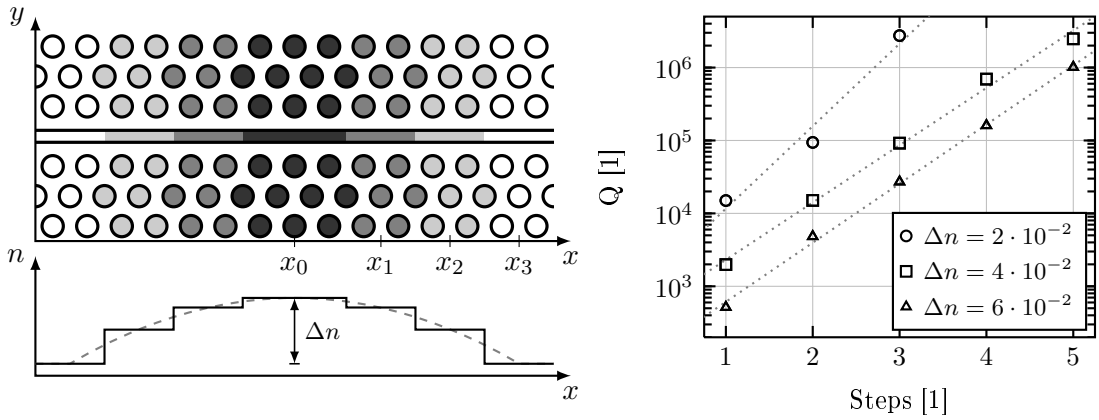

Figure 4.15: Conceptual representation of a three step heterostructure PhC cavity defined by refractive index reduction in individual pores. The gray tones indicate the refractive index in each pore (left). Q values of bleached multistep PhC heterostructures. The dotted straight lines indicate that the quality factor grows exponentially with the number of transition steps (right).

where the index 'max' denotes the maximum number of refractive index transitions.

The resulting Q values for different values of Δn and number of transition steps are summarized in the right panel of figure 4.15. The Q values increase exponentially with the number of transition steps, which is due to the better approximation of the Gaussian envelope profile of the optical field. This reduces the amount of k-vector components in the leaky region, as explained in section 3.3.3. Secondly, cavities with a lower Δn show higher Q values. This is consistent with the behavior observed in the heterostructure cavities with larger a_{cav} in figure 4.7. A stronger contrast in the cut-off frequency between the PhC heterostructure sections leads to a reduced penetration depth, more k-vector components in the leaky region and hence increased vertical scattering.

Finally, the sensitivity to EO-modulation of these structures needs to be analyzed. In the bleached region, the NLO active chromophores are effectively destroyed and hence only the unbleached region in the cavity retains EO-activity. FIT simulations show that a refractive index change of $\Delta n_{\mathrm{eo}} = 10^{-3}$ causes a shift in resonance wavelength of $\Delta\lambda = 0.07$ nm. This is about a factor of 2 less than the unbleached heterostructures discussed in the previous section. However, this reduction is easily offset by the more than one order of magnitude increase in the quality factor.

4.4 Conclusion

In this chapter, the possibilities of guiding and electro-optically manipulating light in hybrid silicon-organic PhC systems were discussed. The implications of a polymer cladding material on the PhC band diagram and its light line were analyzed. It was found that resonators with intrinsic Q factors of 10^5 are easily achievable with this material combination, and the resonance frequency is sufficiently sensitive to refractive index changes of the cladding material. However, due to unfavorable electrode spacing and anisotropy properties of the NLO-polymer, the necessary modulation voltages are almost two orders of magnitude above the desired value of 1 V.

A design of an ultra compact resonant modulator structure based on a heterostructure cavity formed in a slotted PhC waveguide infiltrated with an electro-optically active polymer material was presented. Vertical scattering can be reduced by appropriately choosing the lattice constant in the cavity region thereby designing cavities with high intrinsic Q factors. By introducing an injector section with fast light propagation, the coupling to the resonator was optimized and the maximum transmission at resonance significantly enhanced. It was found that the slotted PhC waveguide geometry offers an optimal solution for EO-manipulation of the guided mode via an external electric modulation signal. The slot geometry concentrates the optical field in the low index polymer material and enables the generation of strong modulation field strengths with comparatively low voltages. The PhC serves as an electric conductor, while shielding the optical field from the required metal electrodes. Thus modulators with switching voltages below 1 V are feasible.

Furthermore, a concept for the definition of ultra high Q heterostructures, based on selectively decreasing the refractive index in the polymer filled holes, was presented. Simulation showed that appropriate tuning of the refractive index profile in propagation direction can result in cavities with Q values exceeding 10^6. At the same time, the EO-modulation sensitivity of the device is decreased, but only moderately.

Chapter 5

Broadband electro-optic modulation

In this chapter, electro-optic modulation in hybrid silicon-organic PhC devices with up to 40 GHz modulation bandwidth using the concepts developed in the previous chapter is experimentally demonstrated. In the first section, the fabrication process with all relevant technological steps is explained. The second section addresses the process of high field poling of second order nonlinear organic materials in narrow slot geometries and associated difficulties. The third section presents device characteristics at frequencies in the kHz range. Characterization at these frequencies is experimentally less challenging than at GHz frequencies and gives important insights into the correct functionality of the modulator. Finally, in the fourth section the results of the GHz modulation experiments are presented and theoretical limitations of the proposed modulator concept are discussed.

5.1 Fabrication process of photonic SOI nano structures

SOI substrates were developed for microelectronic circuits to minimize parasitic capacitances of the individual electronic components. The substrate is a two layer system with a thin silicon layer (typically a few 100 nm) on top of a layer of silicon dioxide (between 1 and 2 μm, also referred to as *buried oxide*, BOX), which reside on a silicon wafer ($\approx$ 0.5 mm) for mechanical stability. The substrates offer an excellent base for micro photonic components as well due to the strong dielectric contrast of silicon ($n = 3.5$) to silicon dioxide ($n = 1.45$) or air, and very low absorption losses in the relevant wavelength windows ($\lambda = 1.3$ μm and $\lambda = 1.55$ μm) in optical telecommunication systems. Furthermore, these substrates are compatible to the very well established CMOS process (complementary metal oxide semiconductor) enabling direct integration of electronic and

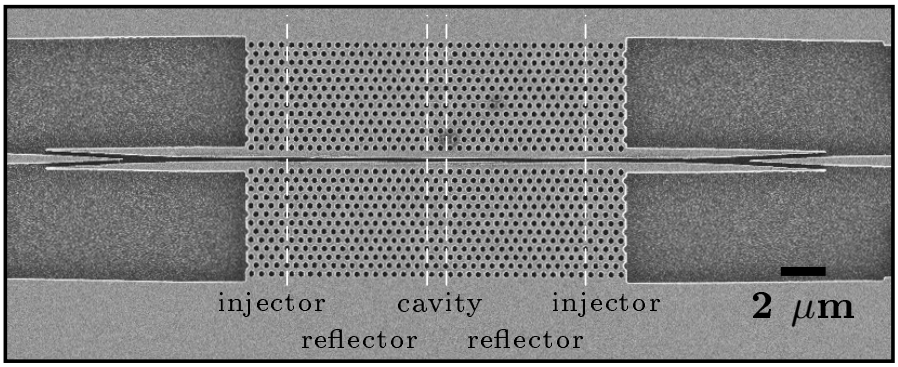

Figure 5.1: SEM of the slotted PhC heterostructure in SOI including slot to strip waveguide converters (before the NLO-polymer deposition).

optical circuits on one chip or die [16, 17]. The maturity of this process allows structuring with nanometer precision.

All devices, which will be discussed in this chapter were fabricated on SOI substrates obtained from S.O.I.TEC, France, with a top silicon layer thickness of 220 nm, to allow mono mode operation of the strip and PhC waveguides. The buried oxide is 2 μm thick, preventing optical losses due to coupling to the lower silicon layer.

The devices were fabricated using an etching mask of ZEP-520 electron beam resist patterned by electron beam lithography (EBL) at the *Heinrich-Hertz-Institute* in Berlin, Germany. Due to the required placement accuracy ($\approx$ 1 nm) and small critical dimensions ($<$ 100 nm), photo lithographic methods are not applicable, mandating the use of e-beam lithography. The pattern of the mask is transfered to the silicon layer through inductively coupled plasma etching. This processing step was carried out at the *Institut Hochfrequenztechnik – Photonik*, Technical University Berlin, Germany. Details on the fabrication process can be found in [105] and [106]. An example of a slotted PhC heterostructure after these processing steps is presented in figure 5.1.

For the EO-modulation experiments metallic contact pads need to be deposited and structured on top of the silicon. A 300 nm layer of either gold or aluminum was deposited by electron beam evaporation. In case of EO-modulation experiments using time constants in the order of milliseconds the contact pads were deposited through a shadow mask. Experiments at radio frequency (RF) in the GHz range, however, require properly dimensioned coplanar waveguides as electrodes in order to keep insertion loss of the electrical wave as small as possible. The required structuring accuracy of the coplanar waveguide is in the order of a few micrometers. Hence, for this electrode type the deposited gold was microstructured using a positive tone photo resist etching mask, which was patterned by photo lithography. The gold was subsequently etched using potassium

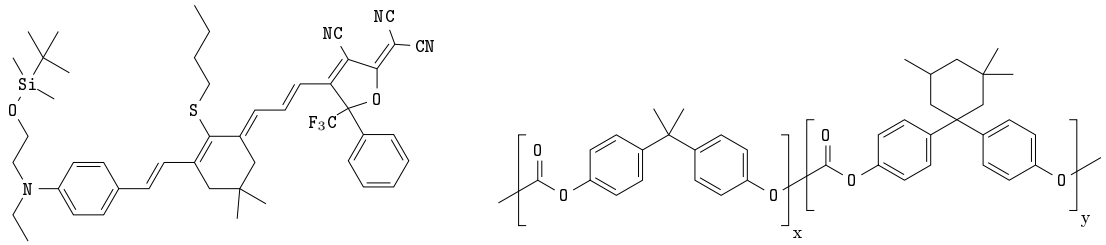

Figure 5.2: Chemical structure of the NLO-chromophore AJ-CKL1 (left) and the polymer host material amorphous polycarbonate (APC) (right).

iodide iodine.

The wafer was then cut into individual chips of 15×15 mm^2 using a wafer saw. To create facets on the access waveguides suitable for end-fire coupling, the chips were cleaved on the input and output side. The chip is typically 8 – 10 mm wide in propagation direction after this procedure.

Finally, the samples were covered by a polymer with strong second order NLO response, consisting of a guest host polymer system of EO-active chromophore AJ-CKL1 doped 25 wt% into amorphous polycarbonate (poly[bisphenol-A-carbonate]x-co-[4, 4'-(3, 3, 5-trimethylcyclohexylidene)diphenol carbonate]) (APC) [107]. The chromophore was supplied by the *Department of Materials Science and Engineering*, University of Washington, USA. The chemical structure of the host polymer and guest chromophore compound is shown in figure 5.2. The polymer was deposited from solution (6 wt% in cyclopentanone) and subsequently baked at 80°C under vacuum for 12 hours to remove residual solvent.

The successful complete infiltration of PhC nano structures with polymer was demonstrated previously to work from solution [108, 109] and melt [110]. For this thesis, the infiltration was also confirmed in an experiment with an alternative NLO-polymer (P(MMA/DR-1)). This is a standard material with a low r_{33} coefficient, which is available in large quantities and was therefore used for this testing purpose. The wetting characteristic of this solution (P(MMA/DR-1) with cyclohexanone) is very similar to the AJ-CKL1, APC, cyclopentanone solution. The complete infiltration of the nanostructures with NLO-polymer is shown in figure 5.3.

5.2 High field poling in nano-slots

As explained in section 2.1, the NLO-chromophores of the polymer matrix need to be aligned in a preferential orientation direction to break the centrosymmetry to observe a macroscopic second order optical nonlinearity. This is achieved through high electric field

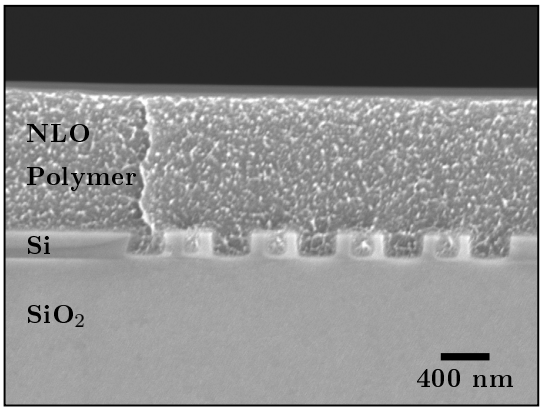

Figure 5.3: SEM view of the PhC structure cross section, completely infiltrated with NLO-polymer P(MMA/DR-1).

poling, during which the sample is heated close to the glass temperature, while a static electric field is applied to the electrodes. A common problem in the high electric field poling process is the risk of dielectric breakdown in the organic material caused by defects and inclusions, as well as the by the increasing conductivity of the polymer at the glass transition temperature. Such an event is undesirable, since it causes an elevated current through the sample and hence reduces the poling efficiency. Furthermore, it creates scattering centers in the polymer material leading to increased optical losses. Dielectric breakdown can occur either at impurities of the polymer or if the electric field strength locally exceeds the damage threshold of the NLO-polymer (typically between 100 and 200 V/μm [107, 27]) due to field enhancement at structural irregularities (e.g. surface roughness) of the electrode. The probability of breakdown at impurities in the organic matrix is kept at a minimum through proper handling and filtering of the solution prior to deposition and through designing the slot with a very small volume of less than 0.5 μm^3. At the same time, it was unexplored prior to this project, whether the small dimensions of the slotted waveguide in combination with the surface roughness at the slot walls could lead to unwanted local enhancements of the poling field above the damage threshold of the polymer.

To align the NLO-chromophores noncentrosymmetrically, the sample was heated to the polymer glass temperature (T_g = 145°C). The heat rate was kept below 10°C/min. During the process, a constant poling voltage of 20 V was applied to the electrodes, resulting in a poling field in the slot of approximately 130 V/μm. After reaching the glass temperature, the sample was rapidly cooled down to room temperature. At room temperature, the poling voltage was switched off, thus freezing the molecular orientation of the NLO-chromophores in the polymer matrix and preserving the macroscopic EO-

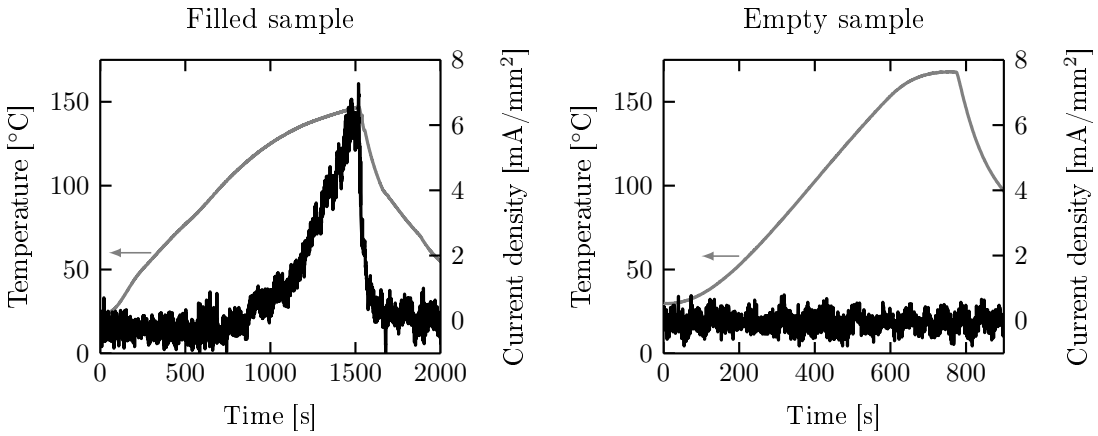

Figure 5.4: Temperature and poling current during the poling process of a polymer filled sample (left) and unfilled sample (right). The applied voltage in both cases was equal to 20 V. The increase in poling current is typical for NLO-polymers as the glass transition temperature is approached. No extreme spikes in the current are visible, indicating that no dielectric breakdown occurred.

response in the absence of the poling field. The heating chamber was purged with inert gas (nitrogen) throughout the poling process, to avoid degradation of the chromophore molecules due to reactions with ambient oxygen. Temperature and poling current were monitored and recorded during the entire poling process.

The left hand panel in figure 5.4 displays a typical current characteristic of a successful poling experiment. A sample, which has not been infiltrated with NLO-polymer (right panel of figure 5.4) does not show any current characteristic. Hence, the current flow in the infiltrated sample originates from conduction mechanisms of the NLO-polymer. The current through the sample increases as the temperature approaches the glass transition temperature of the polymer matrix. The enhanced mobility of charge carriers in this temperature range of the organic material leads to an increased conductivity [111]. However, this is not indicative of a dielectric breakdown event in the sample. In the case of dielectric breakdown, the current typically increases to values in the order of several A/mm^2 at time scales below one second. Both criteria are not observed in the left hand diagram of figure 5.4. The majority of the samples with 150 nm wide nano-slots, which were poled during this project, did not show any indication of a dielectric breakdown. Hence, it is inferred that dielectric breakdown is not a particular problem in the process of high electric field poling at field strengths up to 130 $V/\mu m$ in silicon nano-slot waveguides. This indicates that potentially much higher field stengths could be used to align the chromophores and hence achieve higher Pockels coefficients in the deviecs. Due to

limited amounts of chromophore material available in the scope of this thesis, conservative field values were chosen for poling experiments.

The poling parameters given above (final temperature, heat rate and poling field) are based on thin film poling experiments conducted previously on this organic compound by Chen et al. [107]. The authors report thin film Pockels coefficients of 133 pm/V with 32 wt% chromophore loading. Similar poling experiments were repeated at our institute on thin film samples with approximately 2 μm film thickness and 25 wt% chromophore loading. Pockels coefficients of $r_{33} = 90$ pm/V were recorded using an ellipsometric measurement technique proposed by Teng and Man [112]. However, the r_{33} obtained in the nano-slot waveguides presented in the following sections are between 8 and 12 pm/V, which is about one order of magnitude below the reported thin film value.

The reasons for this significant discrepancy are being investigated in a subsequent research project. One hypothesis is that the orientation of the molecules could be hindered due to the extremely narrow dimensions of the slot, which is less than 100 molecular monolayers. The surface area to volume ratio in the nano-slot is by more than a factor of 10 larger than in the thin film case and molecular interactions at the interface between the silicon and the polymer might reduce the poling efficiency. Effects of anchoring liquid crystal molecules to surfaces may be similar [113] and have been observed in liquid crystals infiltrated into pores with submicron diameter [114]. Further research is necessary to fully understand the processes during the high field poling in nano-slots on a molecular level and derive solutions to enhance the poling efficiency.

5.3 Modulation at low frequencies

The fabricated devices were characterized in an end-fire setup using a broadband source (1525 - 1605 nm bandwidth) and an optical spectrum analyzer. The TE polarized light was coupled on and off chip using microscope objectives and lensed fibers, to create a focused spot with 2.5 μm diameter on the facets of the 3 μm wide access waveguides.

First, the transmission characteristics of the slotted heterostructure were examined. Figure 5.5 shows a clear resonance peak with a quality factor of 2600. This spectrum was compared to numerical results obtained from the FIT simulations, both are superimposed on the experimental curve in figure 5.5. In order to obtain the good match displayed in the figure, the calculated spectrum was red shifted by 1.6% in wavelength compared to the experimental results, which is a reasonable deviation given experimental uncertainties [71]. The numerically achieved Q factor is approximately 3 times higher than the one obtained in the experiment. This is most likely caused by scattering losses from fabrication

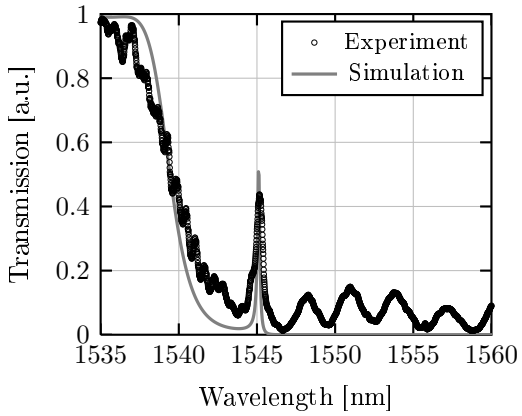

Figure 5.5: Transmission through a slotted PhC heterostructure cavity.

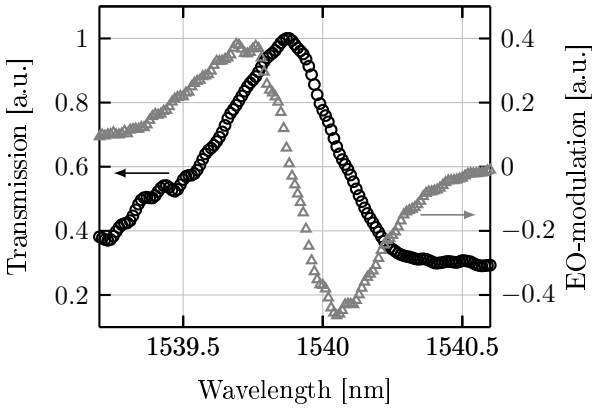

Figure 5.6: Spectral transmission (black circles) and modulation response (gray triangles) of a slotted PhC heterostructure after infiltration with APC/AJ-CKL1 guest host polymer and after high electric field poling. The magnitude of the detected modulated signal corresponds qualitatively to the first derivative of the transmission spectrum.

imperfections, such as surface roughness, as well as deviations from the ideal hole size, shape and position.

To apply an electrical modulation signal to the slot, metal electrodes are deposited laterally to the defect waveguide in a distance W_{Si}. The PhC in this design offers the two fold functionality of being both a reflector for the optical field and electrically conducting at the same time. This allows the modulation field to be applied to the electro-optical polymer inside the slotted region while keeping the optical field from reaching the contacting metal electrodes and introducing additional losses. By choosing $W_{\mathrm{Si}} = 3\ \mu m$ (roughly 8 lattice constants in ΓM direction), the optical loss from the metal contacts is negligible, as the optical field is by 40 dB lower at this point compared to the exit port of the device.

For the EO-modulation measurements, a tunable laser source was employed and the

signal detected with a photodiode. The photodiode was connected to a Lock-In amplifier, which also supplied the electric modulation signal to the device. This technique enables the separate observation of the Pockels effect and electrical Kerr effect, which have linear and quadratic dependency on the electric field, respectively. For simplicity, modulation experiments were carried out at a frequency of $f_{\mathrm{mod}} = 5$ kHz.

A spectral scan of the optical transmission and EO-modulation behavior of the slotted PhC heterostructure is shown in figure 5.6. The linewidth of the resonance peak in this sample was approximately $\Delta\lambda \approx 0.7$ nm, which corresponds to a quality factor of $Q = 2200$. The magnitude of the modulated signal as a function of wavelength is expected to be directly proportional to the first derivative of the transmission spectrum of the modulator for small perturbations of the effective refractive index. This is confirmed by the spectral response of the detected modulation signal in figure 5.6. Most noteworthy is the zero crossing of the modulated signal at the resonance frequency and the accompanying phase shift of π as well as the two prominent extremum points on either side of the resonance frequency.

As mentioned before, the detection by virtue of the Lock-In technique allows the separate detection of the contributions of the Pockels and electrical Kerr effect. For this experiment, the output of the laser source was tuned to the wavelength of the maximum modulation response found in figure 5.6 at 1540 nm. The modulated signals at the first and second harmonic of the modulation frequency were then recorded as a function of the applied voltage to the electrodes, which is directly proportional to the quasi-static field in the polymer filled slot. The results are presented in figure 5.7. As predicted, the modulated signal shows a linear and quadratic dependence on the quasi-static electric field amplitude at the first and second harmonic of the modulation frequency, respectively. This confirms the observation of EO-modulation due to the Pockels and electrical Kerr effect. Finally, the sample was thermally annealed to randomize the orientation of the NLO-chromophores in the polymer host matrix and the above experiments were repeated. After the thermal treatment, the EO-susceptibility was erased and thus the sample did not show any further EO-response, which confirms that the observed modulation effects are indeed due to the NLO-effects of the infiltrated and poled polymer.

The information obtained from the Lock-In amplifier is used to determine the in-device Pockels coefficient. The Lock-In amplifier's signal as a function of wavelength is directly proportional to the wavelength shift and the slope of the transmission curve of the device under test:

$$V_{\mathrm{LK}}(\lambda_0) = \left[\frac{dT}{d\lambda}\right]_{\lambda_0} \Delta\lambda. \tag{5.1}$$

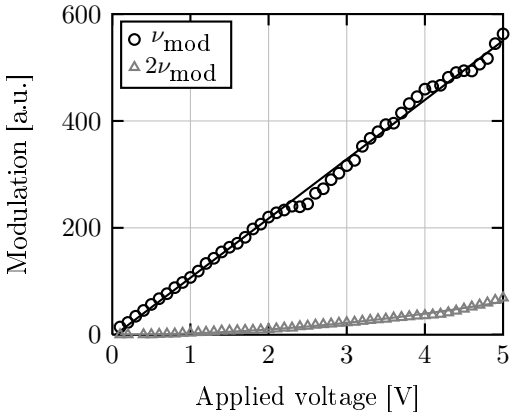

Figure 5.7: Modulation amplitude as a function of modulation voltage detected at the first (black circles) and second harmonic (gray triangles) of the modulation frequency. The lines represent linear (black) and square (gray) fits to the data points, indicating Pockels and electrical Kerr effect, respectively.

From the simulations in section 4.3.3 it is known that the relation of wavelength shift to Δn is:

$$\frac{\Delta\lambda}{\Delta n} = \frac{0.12\ \mathrm{nm}}{10^{-3}} \tag{5.2}$$

Combining the last two expressions with the relation:

$$\Delta n = \frac{1}{2} r_{33} n_{\mathrm{poly}}^3 E_{\mathrm{mod}}, \tag{5.3}$$

leads to:

$$V_{\mathrm{LK}}(\lambda_0) = \left[\frac{dT}{d\lambda}\right]_{\lambda_0} \frac{0.12\ \mathrm{nm}}{10^{-3}} \cdot \frac{1}{2} r_{33} n_{\mathrm{poly}}^3 \frac{V_{\mathrm{mod}}}{d_{\mathrm{slot}}}, \tag{5.4}$$

where V_{mod} is the applied modulation voltage. From the last expression, the Pockels coefficient r_{33} can be easily extracted. The index change of the polymer in the slot is calculated to be approximately $\Delta n = 1.3 \cdot 10^{-4}$ at 1 V applied modulation voltage, thus the in-device Pockels coefficient of the NLO-polymer in this sample is 9 pm/V. This value is about 15 times lower than the value reported in thin films of the same material [107]. This is attributed to an incomplete poling induced polar orientation of the guest chromophores in the 150 nm wide slot [96]. This topic is currently under investigation as the deviation indicates that the performance of the device can be significantly improved by increasing the poling efficiency in the slot. Those further studies target the understanding of the physics of high field poling of macromolecular NLO-materials in submicron silicon cavities in order to obtain an optimized poling process. Such an optimized procedure would give one order of magnitude improvement in the induced refractive index change and consequently spectral shift at a given modulation voltage.

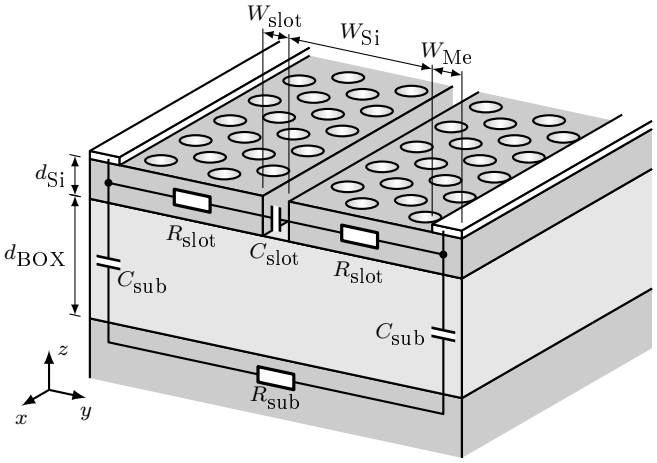

Figure 5.8: Sketch of the electrically relevant geometry of the device (not drawn to scale).

5.4 Modulation at GHz frequencies

Due to the ultra compact dimensions of the device, the maximum modulation frequency is not limited by the group velocity mismatch of the electrical and optical wave, as in macroscopic traveling wave modulator configurations. In the present case, the bandwidth limit is dictated by the charging time needed to load the capacitance C_{slot} formed by the slot through the ohmic resistance R_{slot} across the silicon due to the finite silicon resistivity (figure 5.8). Since the device dimensions are small compared to the RF wavelengths, the electrical behavior can be modeled by lumped elements. The charging time is given by $\tau = 2R_{\mathrm{slot}}C_{\mathrm{slot}}$, which yields the 3 dB frequency:

$$f_{3\mathrm{dB}} = \frac{1}{(2\pi 2R_{\mathrm{slot}}C_{\mathrm{slot}})}, \tag{5.5}$$

with the resistance:

$$R_{\mathrm{slot}} \approx \frac{W_{\mathrm{Si}}\rho}{Fd_{\mathrm{Si}}l} \tag{5.6}$$

and capacitance:

$$C_{\mathrm{slot}} = \frac{\epsilon_0 n_{\mathrm{poly}}^2 d_{\mathrm{Si}} l}{W_{\mathrm{slot}}}, \tag{5.7}$$

where ρ is the resistivity of the used silicon, l the device length and $F = 0.67$ the fill factor (for the definition of the geometry variables see figure 5.8). The resistance is increased by the fill factor as a result of the reduced conducting material in the PhC volume, as, compared to silicon, the polymer filled regions have a near zero conductivity. The formula for the resistance is a first order approximation, as the exact value of a perforated material is not easily calculated. The silicon resistance is approximated using a fill factor approach for estimating the effect of perforation.

The used SOI wafers are specified with a specific resistivity of $\rho_{\mathrm{Si}} = 11.5\ \Omega$cm. When considering a device length of $l = 15\ \mu$m, slot width $W_{\mathrm{slot}} = 150$ nm, and $W_{\mathrm{Si}} = 3\ \mu$m, the slot capacitance computes to be $C_{\mathrm{slot}} = 0.52$ fF and the resistance $R_{\mathrm{slot}} = 157\ \mathrm{k}\Omega$. Consequently, the 3 dB frequency is just about 1 GHz. As a modulation frequency of $f_{3\mathrm{dB}} = 100$ GHz is aimed for, the maximum permitted resistivity is calculated to be 0.1 Ωcm, reducing R_{slot} to 1.4 kΩ. A dopant concentration of $N_{\mathrm{D}} = 10^{17}\ \mathrm{cm}^{-3}$ would be sufficient to decrease the specific resistivity accordingly [115]. At this relatively modest doping level the additional optical loss of roughly 2 dB/cm [116] in the bulk silicon is negligible considering the device length of about 15 μm.

As indicated in figure 5.8, apart from the $R_{\mathrm{slot}}C_{\mathrm{slot}}$ circuit of the slotted PhC waveguide, a parasitic shunt $R_{\mathrm{sub}}C_{\mathrm{sub}}$ circuit through the substrate is also present in this device. These parasitic elements induce a capacitive coupling to the substrate and hence an additional loss mechanism, which might increase the power consumption of the device. To estimate these losses here, the currents through each RC arm of the electrical circuit are compared. Following Ohm's law, this current is inversely proportional to the impedance of each arm. The substrate capacitance is given by:

$$C_{\mathrm{sub}} = \frac{\epsilon_0 n_{\mathrm{BOX}}^2 l(W_{\mathrm{Si}} + W_{\mathrm{Me}})}{d_{\mathrm{BOX}}}, \tag{5.8}$$

where d_{BOX} is the separation of SOI layer and silicon substrate and the width of the metal electrodes W_{Me} is assumed to be equal to W_{Si}. The series connection of the two substrate capacitances then turns out to be comparable to the capacitance of the slot ($\frac{1}{2}C_{\mathrm{sub}} \approx C_{\mathrm{slot}}$). The silicon substrate is assumed to have the same resistivity as the SOI layer. Since the substrate is orders of magnitude thicker than the top waveguiding layer, the substrate resistance R_{sub} is much smaller than R_{slot}. From this it follows that the impedance presented by the parasitic circuit is mostly capacitive and hence consumes primarily reactive power. Certainly, this has to be considered in the design of the feeding lines in order to match the load impedance to the generator.

The on-chip microwave feeding circuitry was designed in collaboration with the *Institut für Hochfrequenztechnik* at the Hamburg University of Technology. A coplanar waveguide structure achieved the best performance in terms of voltage amplitude at the polymer filled slot and compact geometrical footprint compared to microstrip line or slot line feeding geometries. The detailed synthesis and comparison of the microwave circuitry is given in reference [117]. Rigorous numerical simulations using CST Microwave Studio yielded that the field strength across the optical slot is maximized for a coplanar waveguide with an impedance of 100 Ω. As explained above, for these experiments the top silicon layer of the SOI was doped to achieve a specific resistivity of below 0.1 Ωcm. On this

type of SOI substrate, a line with a center metalization width of 14 μm and separation to the ground electrode of 70 μm fulfills the requirement of a waveguide impedance of 100 Ω. Most microwave generators are matched to 50 Ω impedance, which mandates a center strip width of 73 μm and a separation to the ground electrode of 39 μm. For an adiabatic transition between these line geometries, a two step Klopfenstein taper is used [118]. In the first step, the width of the inner conductor is reduced. In the second step, the separation to the outer electrode is increased to the final width. The full length of the taper is 625 μm. The overall geometry is displayed in figure 5.9. The narrow metal strips perpendicular to the direction of propagation at the end of the coplanar waveguide are introduced to reduce the contact resistance to the slotted PhC waveguide devices. This geometry delivers at least 1.02 V voltage drop across the NLO-polymer filled slot with 10 dBm feeding power over a frequency range of 20 – 100 GHz. Due to the coplanar waveguide design, two EO-modulator devices can be addressed in parallel with one electric feeding line. Compared to the dimensions of the slotted PhC waveguide the geometrical footprint of the coplanar taper is several orders of magnitude larger. The taper is required due to the off-chip feeding of the GHz signal, in applications with integrated electric and photonic circuits on one chip, such a large taper section would not be required [8, 18].

Here, a slotted PhC waveguide, infiltrated with NLO-polymer, will be used to demonstrate GHz EO-modulation at the transmission edge of the defect mode. The heterostructures fabricated on the doped wafer did not exhibit a resonance peak. This is most probably due to fabrication imperfections, which were observed in this particular set of samples. Figure 5.9 shows a scanning electron micrograph of the structure. A tapered coupler transition serves to couple the light between the dielectric access waveguide and the slotted waveguide [119]. The 150 nm wide slot in the center of the waveguide is filled with NLO-polymer ($n_{\mathrm{poly}} = 1.63$). The narrow slot width leads to an optical field enhancement in this region [95]. Consequently the defect mode frequency is very sensitive to refractive index changes of the NLO-polymer and the spectral position of the transmission edge can be shifted by an external electric field. Here this effect will be used to electro-optically modulate the amplitude of a continuous wave input signal tuned closely to the transmission edge.

The transmission properties of the devices were again first characterized in an end-fire setup using a broadband source (1525 - 1605 nm bandwidth) and an optical spectrum analyzer. The transmission spectrum of a slotted PhC waveguide device is displayed in figure 5.10, the band edge is located near 1533 nm.

The response to high frequency modulation was measured using side band detection. The optical carrier is amplitude modulated with a sinusoidal signal. Hence, the optical

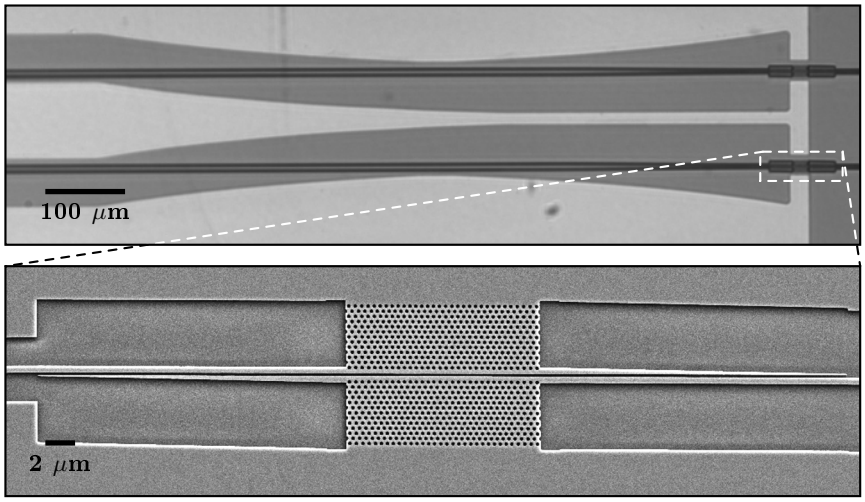

Figure 5.9: Light microscope picture of the coplanar waveguide taper electrodes used to feed the RF wave to the modulator structure (top). Scanning electron micrograph of the slotted PhC waveguide used for the RF modulation experiments (before the deposition of the NLO-polymer) (bottom). The strip to slotted waveguide mode converters are also visible.

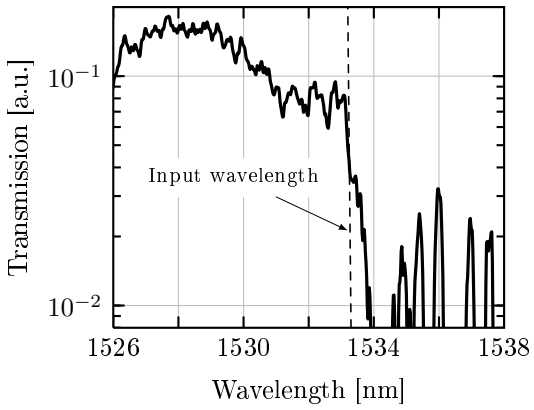

Figure 5.10: Transmission spectrum of a 30 lattice constants long slotted PhC waveguide, infiltrated and covered with NLO-polymer.

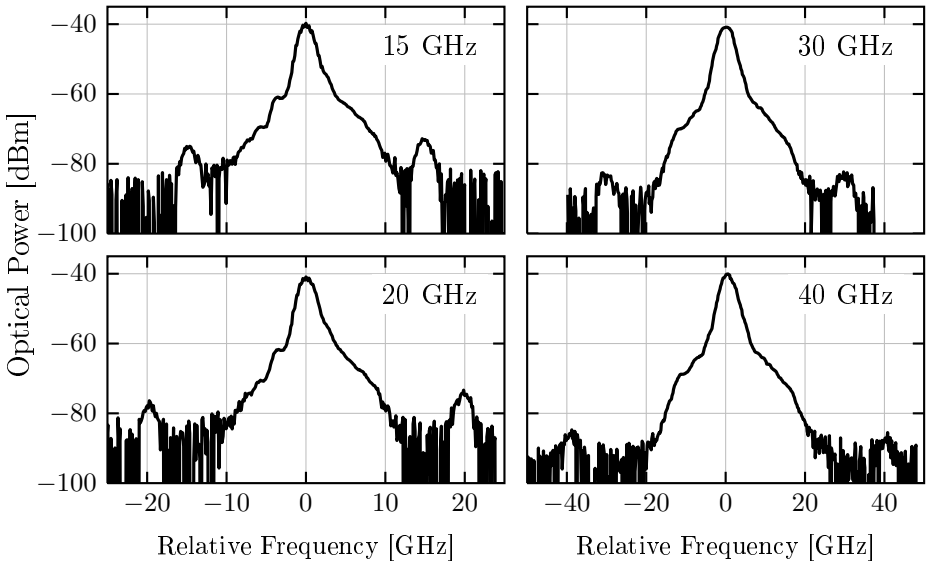

Figure 5.11: Optical power spectra of the modulator output at several modulation frequencies measured with an optical spectrum analyzer. The spectral position of the side bands relative to the optical carrier frequency confirms the EO-modulation at microwave frequencies.

spectrum consists of a main peak of the carrier and two side peaks equally spaced around the carrier. The spectral distance from side to main peak is equal to the modulation frequency. In the experimental setup, the carrier was supplied from a tunable laser source, emitting closely at the transition region from optical pass band to stop band, where the slope of the transmission curve is steep. The electrical signal was supplied from a synthesized signal generator with 40 GHz bandwidth and coupled to the coplanar waveguide of the chip using a ground-signal-ground configured Z-probe with 150 μm pitch. The output signal was detected and spectrally scanned with high resolution around the carrier wavelength using an optical spectrum analyzer.

The resulting optical spectra using modulation frequencies at 15, 20, 30, and 40 GHz are presented in figure 5.11. The side band frequencies are plotted relative to the carrier, which defines the zero frequency. The 15 and 20 GHz plots were obtained with the scanning resolution of the optical spectrum analyzer set to 10 pm, while for the 30 and 40 GHz plots the resolution was set to 20 pm, thus explaining the apparently broader line width of the carrier. The side bands at the correct spectral positions are clearly identifiable at all displayed modulation frequencies. The experiment was repeated with samples, where the NLO-polymer has not been poled. In these samples, no side bands were observed, proving that the modulation is indeed due to the EO-activity of the poled NLO-polymer in the slot. The drop in side band power with increasing frequency is due to reduced

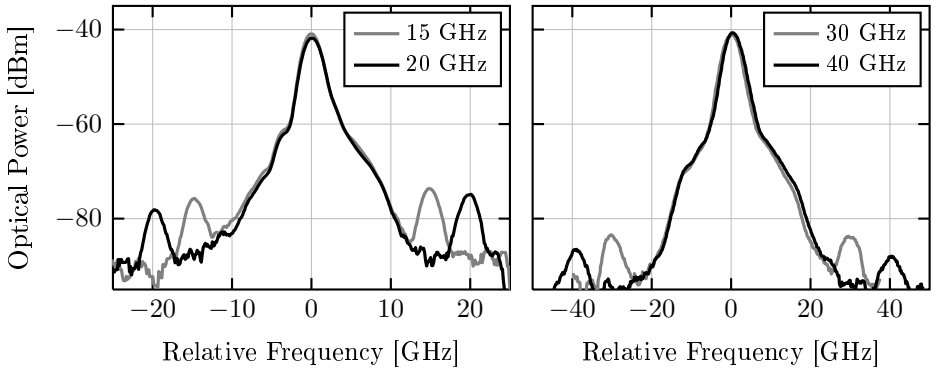

Figure 5.12: Optical power spectra of the modulator output at several modulation frequencies measured with an optical spectrum analyzer and after averaging 5 adjacent data points.

output power of the RF source (specified to be 4 dB) and increased insertion loss from the feeding cable and RF probe (measured with network analyzer to be 2 dB). Therefore the total delivered power to the device drops by 6 dB as the frequency increases from 15 to 40 GHz. Additionally, a shift in the transmission spectrum, most likely due to thermal drift, was observed during the measurements. Slightly shifting the transmission spectrum and, hence decreased the slope of the transmission curve at the probing wavelength. The combined effects lead to the observed drop in side band power of approximately 10 dB.

The low power level of the center frequency shown in the plots of figure 5.11 is a result of strong insertion loss, which amounts to 50 dB in the experimental setup. Consequently, the spectral data points around the amplitude modulation side bands are very close to the noise floor of the employed optical spectrum analyzer. To reduce the noise, which is evident in figure 5.11, the power spectra were smoothed using averaging of 5 adjacent data points. The resulting curves are shown in figure 5.12, where the side bands can be identified with much better clarity.

The side band power P_{SB} in amplitude modulation schemes is proportional to the square of the modulated amplitude, which in this case is the change in transmission through the slotted PhC waveguide ΔT. The calculated in-device Pockels coefficient of the NLO-polymer was 12 pm/V, using the technique described above. This value is more than one order of magnitude below the value reported for thin film samples of the same material [107] or other NLO-polymers. Thus, even at constant Q the modulation efficiency and hence the side band power could be increased more than 20 dB by enhancing the poling efficiency of the slotted device and achieving r_{33} values similar to those obtained in thin films. The modulation efficiency could be improved even further by performing the modulation at a micro cavity resonance, where the slope of the transmission spectrum

is much steeper as it was demonstrated at kHz modulation frequencies in section 5.3. Alternatively, following Brosi et al. [97] a slow light slotted PhC waveguide Mach-Zehnder interferometer could be used to enhance the modulation depths.

5.5 Conclusion

In conclusion, slotted PhC waveguides were fabricated to form a heterostructure cavity in SOI covered and infiltrated by NLO-polymer. This enables EO-modulation on an extremely small geometrical footprint at potentially very high modulation speeds in the GHz range. The devices achieved Q-factors of up to 2600 and the EO-modulation of the device's resonance position was successfully shown.

Additionally, EO-modulation in slotted PhC waveguides in SOI covered and infiltrated by NLO-polymer with up to 40 GHz bandwidth was demonstrated. The modulation frequency was limited only by the available RF source, and no significant roll off in the modulation signal amplitude up to this value was observed, indicating that operation at even higher bandwidths should be feasible. The device had an extremely small geometrical footprint, with a slotted PhC waveguide spanning only 30 lattice constants in propagation direction. The EO amplitude modulation was performed at the optical mode transmission edge of the device, where the slope of the spectrum is only moderate. The efficiency of the device can be greatly improved, if more sophisticated PhC devices like resonant or MZI configurations are used. Even further improvements in modulation depth are possible, if the poling efficiency of the NLO-polymer is increased to yield equally large r_{33} values in a slotted PhC waveguide as in thin films. All of these three approaches are currently in the focus of our research efforts. The presented results show that ultra-compact and ultra-fast EO-modulators can be realized in slotted PhC waveguides based on hybrid silicon-organic materials.

Chapter 6

Conclusion and outlook

6.1 Conclusion

The objective of this thesis was to develop an EO-modulator design with large electrical bandwidth ($> 10\,\mathrm{GHz}$), low drive voltage, and small geometrical footprint. NLO-polymers were the material of choice for the nonlinear optical interaction of the quasi-static electric and the optical field. NLO-organic materials offer ultra fast response times and simultaneously very large EO-coefficients, satisfying the first two requirements of the desired EO-modulator. A PhC based design was envisioned to meet the third objective of a small geometric footprint. However, polymers generally exhibit only a moderate refractive index and thus limited light confinement ability, principally prohibiting small device geometries. All studies conducted within the scope of this thesis focused on satisfying the given objectives with NLO-polymers in conjunction with PhCs and finding solutions to overcome the weakness of a low dielectric constant.

First, the possibilities of full three-dimensional light confinement in PhC slab nano cavities using low refractive index NLO-organic materials as core material were evaluated. It was demonstrated analytically that moderate refractive index contrast PhC defect structures suffer the intrinsic disadvantage of having the resonance much closer to the air light line compared to the same structures in high dielectric materials. Adequate designs can mitigate this effect and, theoretically, intrinsic Q factors exceeding 10^4 could also be achieved in low index PhC defects. However, this requires fabrication technologies with placement accuracies in the regime of single atomic layers. To circumvent the high demands on geometric positioning accuracy, an alternative scheme based on permanent local index variation was proposed that could enable intrinsic Qs up to 10^5.

Next, it was found that PhC slab devices with silicon core and NLO-polymer as cladding material easily achieve intrinsic Qs exceeding 10^5, by reason of the increased index con-

trast between core and cladding material. To enhance the interaction of the quasi-static electric field and the optical mode, a narrow slot was introduced into the PhC waveguide. The resulting sensitivity of the spectral position of the mode on the EO-induced index variation is sufficient to operate the device below 1 V modulation voltage with a state of the art NLO-polymer ($r_{33} = 150$ pm/V). By introducing an injector section with fast light propagation, the coupling to the resonator was optimized and the maximum transmission at resonance significantly enhanced. The slotted PhC waveguide geometry offers an optimal solution for EO-manipulation of the guided mode via an external electric modulation signal. SOI substrates with a reduced sheet resistance of the top silicon layer should enable devices with an electrical 3 dB bandwidth as high as 100 GHz. The specific resistivity of the top layer can be reduced by slight doping without increasing the optical loss to unacceptable levels. Additionally, it was shown that the concept of permanent local index variation of the NLO-polymer can be applied to this configuration as well. By selectively bleaching the cladding material, intrinsic Q values of more than 10^6 are feasible.

In the final step, the devices were fabricated on SOI wafers to experimentally validate the developed concept. In spectral measurements, loaded Q values up to 2600 were measured and the EO-modulation of the device's spectral position was successfully demonstrated. Modulation up to 40 GHz was shown on slotted PhC waveguide samples fabricated on p^+-doped SOI substrates. The modulation frequency was limited only by the available RF source and power feeding scheme. No significant roll off was observed in the modulation signal amplitude up to this value, indicating that operation at even higher bandwidths should be feasible, as the EO-effect based on pure electronic displacement polarization is intrinsically ultra fast. The presented results show that ultra compact and ultra fast EO-modulators can be realized in slotted PhC waveguides based on hybrid silicon and organic materials.

6.2 Outlook

The experimental results presented in this thesis prove the validity of using hybrid silicon-organic materials as a platform for ultra fast and geometrically compact EO-modulator devices. However, it has to be noted that this technology is in direct competition with silicon integrated modulator designs, which modulate the material index by charge carrier injection or depletion. Even though the modulation speed of these devices is limited by the charge carrier lifetime in silicon, numerous groups have been active and successful in achieving broadband modulation in p-n and p-i-n diode devices. A good overview of

the recent progress in the field of silicon-diode-based modulators is given in [120]. Most remarkable is the performance of a 30 GHz bandwidth reverse bias p-n diode Mach-Zehnder modulator presented by Intel [20]. However, EO-modulators based on hybrid silicon-organic materials are just beginning to emerge and bear significant improvement potential, as outlined in the remaining paragraphs of this thesis.

Improvement of modulation depth: The modulation depth is essential for data transmission systems to adequately separate the transmitted signal from background noise. For the hybrid silicon-organic slotted PhC devices, which were presented in this thesis, a number of approaches can be used to improve the achievable modulated amplitude at a given modulation voltage:

- The NLO-polymer in the slot of the devices presented in chapter 5 only achieved 10% of the Pockels coefficient, which has been reported for the bulk material. This bears improvement potential of 20 dB in modulated amplitude. Clearly, a better understanding of the poling process of NLO-polymers in narrow silicon slots is necessary to fully exploit the potential of the given NLO-chromophore.

- Similarly, novel NLO-organic materials with even higher Pockels coefficients could contribute to enhance the modulation sensitivity.

- Increasing the quality factor of the resonators to the permitted maximum value of 10^4 represents another lever.

All three of these approaches are a direct consequence of the relation given in equation 5.4.

Increase in electrical bandwidth: The limit of the electric modulation bandwidth has not yet been explored. The 40 GHz reported in chapter 5 were limited only by the RF hardware available at this institute. The true 3 dB frequency of these devices has yet to be tested. The NLO-polymer material properties suggest that modulation speeds up to the THz range are possible. This, however, would require more sophisticated on-chip microwave feeding schemes.

Increase in optical bandwidth: Modulators based on resonant structures inherently have a narrow optical bandwidth. Slow light PhC Mach-Zehnder modulator designs, on the other hand, could operate across a broader frequency range. However, this comes at the expense of a larger geometrical footprint, due to the reduced sensitivity of the non-resonant device. Such concepts have already been discussed in the theoretical paper by Brosi et al. [97] and are an interesting alternative.

Improvement in coupling efficiency: Even with the injector section developed in chapter 4, the coupling from the slotted ridge to the slotted PhC introduces scattering losses, limiting the peak transmission to -3 dB. A coupling scheme for slotted PhCs, similar to those developed in [13] for unslotted PhC waveguides, could improve the device performance in terms of insertion loss.

Testing for data transmission rates: To evaluate the ability of the developed device to electro-optically encode data streams, more sophisticated test equipment is required. Testbeds with the capability to record important figures of merit for system designers like bits per second, bit error rate (BER), open eye diagrams and the like would be necessary to estimate the modulator performance in a realistic application environment.

Compensation of thermal drift: The spectral properties of silicon photonic devices are very sensitive to temperature variations. The strong thermo-optic coefficient in silicon is responsible for this shift. It was shown in slotted ridge waveguides that polymer claddings with thermo-optic coefficients of opposing sign can be used to compensate for the change in effective refractive index to virtually zero [121]. Extending this idea to appropriately designed slotted PhCs cladded with NLO-polymer could give these structures an important advantage over all-silicon devices.

Bibliography

[1] G. P. Agrawal, *Lightwave Technology: Telecommunication Systems.* Wiley, New York, 1st ed., 2005.

[2] B. E. A. Saleh and M. C. Teich, *Fundamentals of Photonics.* Wiley, 2nd ed., 2007.

[3] *IEEE Standard for Information Technology- Telecommunications and Information Exchange Between Systems- Local and Metropolitan Area Networks- Specific Requirements Part 3: Carrier Sense Multiple Access With Collision Detection (CSMA/CD) Access Method and Physical Layer Specifications Amendment: Media Access Control Parameters, Physical Layers, and Management Parameters for Subscriber Access Networks*, 2004.

[4] *IEEE Standard for Information Technology- Telecommunications and Information Exchange Between Systems- Local and Metropolitan Area Networks- Specific Requirements Part 3: Carrier Sense Multiple Access With Collision Detection (CSMA/CD) Access Method and Physical Layer Specifications Amendment: Media Access Control (MAC) Parameters, Physical Layers, and Management Parameters for 10 Gb/S Operation*, 2002.

[5] G. P. Agrawal, *Fiber-optic communication systems.* Wiley, New York, 2nd ed., 1997.

[6] D. Huang, T. Sze, A. Landin, R. Lytel, and H. L. Davidson, "Optical interconnects: out of the box forever?," *IEEE Journal of Selected Topics in Quantum Electronics*, vol. 9, no. 2, pp. 614 – 623, 2003.

[7] D. A. B. Miller, "Device Requirements for Optical Interconnects to Silicon Chips," *Proceedings of the IEEE*, vol. 97, no. 7, pp. 1166 – 1185, 2009.

[8] B. G. Lee, A. Biberman, J. Chan, and K. Bergman, "High-Performance Modulators and Switches for Silicon Photonic Networks-on-Chip," *IEEE Journal of Selected Topics in Quantum Electronics*, vol. 16, no. 1, pp. 6 – 22, 2010.

[9] A. F. J. Levi, "Optical interconnects in systems," *Proceedings of the IEEE*, vol. 88, no. 6, pp. 750 – 757, 2000.

[10] E. Yablonovitch, "Inhibited spontaneous emission in solid-state physics and electronics," *Physical Review Letters*, vol. 58, no. 20, pp. 2059 – 2062, 1987.

[11] S. John, "Strong Localization of Photons in Certain Disordered Dielectric Superlattices," *Physical Review Letters*, vol. 58, no. 23, pp. 2486 – 2489, 1987.

[12] Joannopoulos, D. J. and Villeneuve, R. P. and Fan, S., "Photonic crystals: Putting a new twist on light," *Nature*, vol. 386, pp. 143 – 149, 1997.

[13] A. Petrov, *Slow light photonic crystal line-defect waveguides*. PhD thesis, Hamburg University of Technology, 2008.

[14] T. Asano, S. B. Song, and S. Noda, "Analysis of the experimental Q factors (1 million) of photonic crystal nanocavities," *Optics Express*, vol. 14, no. 5, pp. 1996 – 2002, 2006.

[15] Y. Vlasov and S. McNab, "Losses in single-mode silicon-on-insulator strip waveguides and bends," *Optics Express*, vol. 12, no. 8, pp. 1622 – 1631, 2004.

[16] B. Jalali, M. Paniccia, and G. Reed, "Silicon photonics," *IEEE Microwave Magazine*, vol. 7, no. 3, pp. 58 – 68, 2006.

[17] R. Soref, "The past, present, and future of silicon photonics," *IEEE Journal of Selected Topics in Quantum Electronics*, vol. 12, no. 6, pp. 1678 – 1687, 2006.

[18] A. Liu, L. Liao, Y. Chetrit, J. Basak, H. Nguyen, D. Rubin, and M. Paniccia, "Wavelength Division Multiplexing Based Photonic Integrated Circuits on Silicon-on-Insulator Platform," *IEEE Journal of Selected Topics in Quantum Electronics*, vol. 16, no. 1, pp. 23 –32, 2010.

[19] S. R. Jacobsen, N. K. Andersen, I. P. Borel, J. Fage-Pedersen, H. L. Frandsen, O. Hansen, M. Kristensen, V. A. Lavrinenko, G. Moulin, H. Ou, C. Peucheret, B. Zsigri, and A. Bjarklev, "Strained silicon as a new electro-optic material," *Nature*, vol. 441, pp. 199 – 202, 2006.

[20] L. Liao, A. Liu, J. Basak, H. Nguyen, M. Paniccia, D. Rubin, Y. Chetrit, R. Cohen, and N. Izhaky, "40 Gbit/s silicon optical modulator for highspeed applications," *Electronics Letters*, vol. 43, no. 22, 2007.

[21] Q. Xu, S. Manipatruni, B. Schmidt, J. Shakya, and M. Lipson, "12.5 Gbit/s carrier-injection-based silicon micro-ring silicon modulators," *Optics Express*, vol. 15, no. 2, pp. 430 – 436, 2007.

[22] X. Chen, Y.-S. Chen, Y. Zhao, W. Jiang, and R. T. Chen, "Capacitor-embedded 0.54 pJ/bit silicon-slot photonic crystal waveguide modulator," *Optics Letters*, vol. 34, no. 5, pp. 602 – 604, 2009.

[23] M. Lee, E. H. Katz, C. Erben, M. D. Gill, P. Gopalan, D. J. Heber, and J. D. McGee, "Broadband Modulation of Light by Using an Electro-Optic Polymer," *Science*, vol. 298, pp. 1401 – 1403, 2002.

[24] Y. Enami, T. C. Derose, D. Mathine, C. Loychik, C. Greenlee, A. R. Norwood, D. T. Kim, J. Luo, Y. Tian, K.-Y. A. Jen, and N. Peyghambarian, "Hybrid polymer/sol-gel waveguide modulations with exceptionally large electro-optic coefficients," *Nature Photonics*, vol. 1, pp. 180 – 185, 2007.

[25] T.-D. Kim, J.-W. Kang, J. Luo, S.-H. Jang, J.-W. Ka, N. Tucker, J. B. Benedict, L. R. Dalton, T. Gray, M. R. Overney, H. D. Park, W. N. Herman, and A. K.-Y. Jen, "Ultralarge and Thermally Stable Electro-Optic Activities from Supramolecular Self-Assembled Molecular Glasses," *Journal of the American Chemical Society*, vol. 129, no. 3, pp. 488 – 489, 2007.

[26] T.-D. Kim, J. Luo, Y.-J. Cheng, Z. Shi, S. Hau, S.-H. Jang, X.-H. Zhou, Y. Tian, B. Polishak, S. Huang, H. Ma, L. R. Dalton, and A. K.-Y. Jen, "Binary Chromophore Systems in Nonlinear Optical Dendrimers and Polymers for Large Electrooptic Activities," *The Journal of Physical Chemistry C*, vol. 112, no. 21, pp. 8091 – 8098, 2008.

[27] S.-H. Jang and A. K.-Y. Jen, "Electro-Optic (E-O) Molecular Glasses," *Chemistry - An Asian Journal*, vol. 4, no. 1, pp. 20 – 31, 2009.

[28] L. R. Dalton, "Rational design of organic electro-optic materials," *Journal of Physics: Condensed Matter*, vol. 15, pp. R897 – R934, 2003.

[29] C. Liguda, G. Böttger, A. Kuligk, R. Blum, M. Eich, H. Roth, J. Kunert, W. Morgenroth, H. Elsner, and G. H. Meyer, "Polymer photonic crystal slab waveguides," *Applied Physics Letters*, vol. 78, no. 17, pp. 2434 – 2436, 2001.

[30] M. Schmidt, *Nonlinear Optical Polymeric Photonic Crystals*. PhD thesis, Hamburg University of Technology, 2005.

[31] R. L. Sutherland, *Handbook of Nonlinear Optics*. Marcel Dekker, Inc., 2nd ed., 2003.

[32] F. Kajzar, K.-S. Lee, and A. K.-Y. Jen, "Polymeric Materials and their Orientation Techniques for Second-Order Nonlinear Optics," *Advances in Polymer Science*, vol. 161, pp. 1 – 85, 2003.

[33] B. Kippelen and N. Peyghambarian, "Photorefractive Polymers and their Applications," *Advances in Polymer Science*, vol. 161, pp. 87 – 156, 2003.

[34] M. J. Cho, D. H. Choi, P. A. Sullivan, A. J. P. Akelaitis, and L. R. Dalton, "Recent progress in second-order nonlinear optical polymers and dendrimers," *Progress in Polymer Science*, vol. 33, pp. 1013 – 1058, 2008.

[35] J. D. Luo, X. H. Zhou, and A. K.-Y. Jen, "Rational molecular design and supramolecular assembly of highly efficient organic electro-optic materials," *Journal of Materials Chemistry*, vol. 19, pp. 7410 – 7424, 2009.

[36] J. L. Oudar and D. S. Chemla, "Theory of second-order optical susceptibilities of benzene substitutes," *Optics Communications*, vol. 13, no. 2, pp. 164 – 168, 1975.

[37] J. L. Oudar and D. S. Chemla, "Hyperpolarizabilities of the nitroanilines and their relations to the excited state dipole moment," *The Journal of Chemical Physics*, vol. 66, no. 6, pp. 2664 – 2668, 1977.

[38] M. G. Kuzyk, "Quantum limits of the hyper-Rayleigh scattering susceptibility," *IEEE Journal of Selected Topics in Quantum Electronics*, vol. 7, no. 5, pp. 774 – 780, 2001.

[39] M. G. Kuzyk, "Fundamental Material Limitations on Optical Devices," *IEEE Circuits and Devices Magazine*, vol. 19, no. 1, pp. 8 – 17, 2003.

[40] J. Pérez-Moreno, Y. Zhao, K. Clays, and M. G. Kuzyk, "Modulated conjugation as a means for attaining a record high intrinsic hyperpolarizability," *Optics Letters*, vol. 32, no. 1, pp. 59 – 61, 2007.

[41] M. G. Kuzyk, "Intrinsic Hyperpolarizabilities as a Figure of Merit for Electro-optic Molecules," *The Journal of Physical Chemistry C*, vol. 112, no. 21, pp. 7978 – 7982, 2008.

[42] L. R. Dalton, P. A. Sullivan, and D. H. Bale, "Electric Field Poled Electro-optic Materials: State of the Art and Future Prospects," *Chemical Reviews*, vol. 110, no. 1, pp. 25 – 55, 2010.

[43] K. B. Rochford, R. Zanoni, Q. Gong, and G. I. Stegeman, "Fabrication of integrated optical structures in polydiacetylene films by irreversible photoinduced bleaching," *Applied Physics Letters*, vol. 55, no. 12, pp. 1161–1163, 1989.

[44] J. Vydra, H. Beisinghoff, T. Tschudi, and M. Eich, "Photodecay mechanisms in side chain nonlinear optical polymethacrylates," *Applied Physics Letters*, vol. 69, no. 8, pp. 1035 – 1037, 1996.

[45] A. Galvan-Gonzalez, M. Canva, G. I. Stegeman, R. Twieg, K. P. Chan, T. C. Kowalczyk, X. Q. Zhang, H. S. Lackritz, S. Marder, and S. Thayumanavan, "Systematic behavior of electro-optic chromophore photostability," *Optics Letters*, vol. 25, no. 5, pp. 332 – 334, 2000.

[46] M. E. DeRosa, M. He, J. S. Cites, S. M. Garner, and Y. R. Tang, "Photostability of High $\mu\beta$ Electro-Optic Chromophores at 1550 nm," *The Journal of Physical Chemistry B*, vol. 108, no. 25, pp. 8725 – 8730, 2004.

[47] D. Rezzonico, M. Jazbinsek, P. Günter, C. Bosshard, D. H. Bale, Y. Liao, L. R. Dalton, and P. J. Reid, "Photostability studies of π-conjugated chromophores with resonant and nonresonant light excitation for long-life polymeric telecommunication devices," *Journal of the Optical Society of America B*, vol. 24, no. 9, pp. 2199 – 2207, 2007.

[48] S. Takahashi, B. Bhola, A. Yick, W. Steier, J. Luo, A.-Y. Jen, D. Jin, and R. Dinu, "Photo-Stability Measurement of Electro-Optic Polymer Waveguides With High Intensity at 1550-nm Wavelength," *Journal of Lightwave Technology*, vol. 27, no. 8, pp. 1045 – 1050, 2009.

[49] A. K.-Y. Jen, Y. Liu, L. Zheng, S. Liu, K. J. Drost, Y. Zhang, and L. R. Dalton, "Synthesis and Characterization of Highly Efficient, Chemically and Thermally Stable Chromophores with Chromone-Containing Electron Acceptors for NLO Applications," *Advanced Materials*, vol. 11, no. 6, pp. 452 – 455, 1999.

[50] S.-K. Kim, Y.-C. Hung, S. B.-J., K. Geary, W. Yuan, B. Bortnik, H. R. Fetterman, C. Wang, W. H. Steier, and C. Zhang, "Side-chain electro-optic polymer modulator

with wide thermal stability ranging from -46 °C to 95 °C for fiber-optic gyroscope applications," *Applied Physics Letters*, vol. 87, no. 6, p. 061112, 2005.

[51] J. Luo, M. Haller, H. Li, T.-D. Kim, and A.-Y. Jen, "Highly Efficient and Thermally Stable Electro-optic Polymer from a Smartly Controlled Crosslinking Process," *Advanced Materials*, vol. 15, no. 19, pp. 1635 – 1638, 2003.

[52] M. Haller, J. Luo, H. Li, T.-D. Kim, Y. Liao, B. H. Robinson, L. R. Dalton, and A. K.-Y. Jen, "A Novel Lattice-Hardening Process To Achieve Highly Efficient and Thermally Stable Nonlinear Optical Polymers," *Macromolecules*, vol. 37, no. 3, pp. 688 – 690, 2005.

[53] L. Rayleigh, "On the maintenance of vibrations by forces of double frequency, and on the propagation of waves through a medium endowed with a periodic structure," *Philosophical Magazine*, vol. 24, pp. 145 – 159, 1887.

[54] J. D. Joannopoulos, S. G. Johnson, J. N. Winn, and R. D. Meade, *Photonic Crystals, Molding the Flow of Light*. Princeton University Press, 2nd ed., 2008.

[55] M. Qiu, "Effective index method for heterostructure-slab-waveguide-based two-dimensional photonic crystals," *Applied Physics Letters*, vol. 81, no. 7, pp. 1163 – 1165, 2002.

[56] M. J. Manolatou, M. J. Khan, S. Fan, P. R. Villeneuve, H. A. Haus, and J. D. Joannopoulos, "Coupling of Modes Analysis of Resonant Channel Add-Drop Filters," *IEEE Journal of Quantum Electronics*, vol. 35, no. 9, pp. 1322 – 1331, 1999.

[57] L. C. Andreani and D. Gerace, "Photonic-crystal slabs with a triangular lattice of triangular holes investigated using a guided-mode expansion method," *Phys. Rev. B*, vol. 73, no. 23, pp. 235114 – 235116, 2006.

[58] R. D. Meade, A. M. Rappe, K. D. Brommer, J. D. Joannopoulos, and O. L. Alerhand, "Accurate theoretical analysis of photonic band-gap materials," *Physical Review B*, vol. 48, no. 11, pp. 8434 – 8437, 1993.

[59] http://fisicavolta.unipv.it/ricerca/fotonici/.

[60] G. Böttger, *Finite integration simulations of photonic crystal structures for microphotonic devices*. PhD thesis, Hamburg University of Technology, 2005.

[61] T. Weiland, "Time domain electromagnetic field computation with finite difference methods," *International Journal of Numerical Modelling*, vol. 9, pp. 295 – 319, 1996.

[62] M. Clemens and T. Weiland, "Discrete electromagnetism with the finite integration technique," *Progress in Electromagnetic Research PIER*, vol. 32, pp. 65 – 87, 2001.

[63] S. Fan, D. J. Joannopoulos, N. J. Winn, A. Devenyi, C. J. Chen, and D. R. Meade, "Guided and defect modes in periodic dielectric waveguides," *Journal of the Optical Society of America B*, vol. 12, no. 7, pp. 1267 – 1272, 1995.

[64] S. J. Foresi, R. P. Villeneuve, J. Ferrera, R. E. Thoen, G. Steinmeyer, S. Fan, D. J. Joannopoulos, C. L. Kimerling, I. H. Smith, and P. E. Ippen, "Photonic-bandgap microcavities in optical waveguides," *Nature*, vol. 390, pp. 143 – 145, 1997.

[65] P. Velha, E. Picard, T. Charvolin, E. Hadji, C. J. Rodier, P. Lalanne, and D. Peyrade, "Ultra-high Q/V Fabry-Perot microcavity on SOI substrate," *Optics Express*, vol. 15, no. 24, pp. 16090 – 16096, 2007.

[66] B. P. Deotare, W. M. McCutcheon, W. I. Frank, M. Khan, and M. LonCar, "High quality factor photonic crystal nanobeam cavities," *Applied Physics Letters*, vol. 94, no. 12, pp. 121106 – 3, 2009.

[67] A. Nahata, J. Shan, J. T. Yardley, and C. Wu, "Electro-optic determination of the nonlinear-optical properties of a covalently functionalized Disperse Red 1 copolymer," *Journal of the Optical Society of America B*, vol. 10, no. 9, pp. 1553 – 1564, 1993.

[68] U. Hübner, R. Boucher, W. Morgenroth, M. Schmidt, and M. Eich, "Fabrication of photonic crystal structures in polymer waveguide material," *Microelectronic Engineering*, vol. 83, no. 4-9, pp. 1138 – 1141, 2006.

[69] J. H. Wülbern, M. Schmidt, U. Huebner, R. Boucher, W. Volksen, Y. Lu, R. Zentel, and M. Eich, "Polymer based tuneable photonic crystals," *Physica Status Solidi A-Applied Research*, vol. 204, no. 11, pp. 3739 – 3753, 2007.

[70] T. Tanabe, M. Notomi, E. Kuramochi, A. Shinya, and H. Taniyama, "Trapping and delaying photons for one nanosecond in an ultrasmall high-Q photonic-crystal nanocavity," *Nature Photonics*, vol. 1, no. 1, pp. 49 – 52, 2007.

[71] J. Li, T. P. White, L. O'Faolain, A. Gomez-Iglesias, and T. F. Krauss, "Systematic design of flat band slow light in photonic crystal waveguides," *Optics Express*, vol. 16, no. 9, pp. 6227 – 6232, 2008.

[72] S. C. Kee, P. S. Han, B. K. Yoon, G. C. Choi, K. H. Sung, S. S. Oh, Y. H. Park, S. Park, and H. Schift, "Photonic band gaps and defect modes of polymer photonic crystal slabs," *Applied Physics Letters*, vol. 86, no. 5, p. 051101, 2005.

[73] M. Schmidt, G. Böttger, M. Eich, W. Morgenroth, U. Hübner, R. Boucher, G. H. Meyer, D. Konjhodzic, H. Bretinger, and F. Marlow, "Ultralow refractive index substrates-a base for photonic crystal slab waveguides," *Applied Physics Letters*, vol. 85, no. 1, pp. 16 – 18, 2004.

[74] M. Qiu, "Band gap effects in asymmetric photonic crystal slabs," *Physical Review B*, vol. 66, no. 3, p. 033103, 2002.

[75] G. C. Choi, T. Y. Han, T. J. Kim, and H. Schift, "Air-suspended two-dimensional polymer photonic crystal slab waveguides fabricated by nanoimprint lithography," *Applied Physics Letters*, vol. 90, no. 22, p. 221109, 2007.

[76] D. Gerace and C. L. Andreani, "Low-loss guided modes in photonic crystal waveguides," *Optics Express*, vol. 13, no. 13, pp. 4939 – 4951, 2005.

[77] S. B. Song, S. Noda, T. Asano, and Y. Akahane, "Ultra-high-Q photonic double-heterostructure nanocavity," *Nature Materials*, vol. 4, no. 3, pp. 207 – 210, 2005.

[78] O. Painter, K. R. Lee, A. Scherer, A. Yariv, D. J. O'Brien, D. P. Dapkus, and I. Kim, "Two-dimensional photonic band-gap defect mode laser," *Science*, vol. 284, pp. 1819 – 1821, 1999.

[79] P. Michler, A. Kiraz, C. Becher, W. Schoenfeld, P. Petroff, L. Zhang, E. Hu, and A. Imamoglu, "A quantum dot single-photon turnstile device," *Science*, vol. 290, no. 5500, p. 2282, 2000.

[80] F. M. Yanik and S. Fan, "Stopping light all optically," *Physical Review Letters*, vol. 92, no. 8, p. 083901, 2004.

[81] Y. Akahane, T. Asano, S. B. Song, and S. Noda, "High-Q photonic nanocavity in a two-dimensional photonic crystal," *Nature*, vol. 425, pp. 944 – 947, 2003.

[82] Y. H. Ryu, M. Notomi, and H. Y. Lee, "High-quality-factor and small-mode-volume hexapole modes in photonic-crystal-slab nanocavities," *Applied Physics Letters*, vol. 83, no. 21, pp. 4294 – 4296, 2003.

[83] H. G. Kim, H. Y. Lee, A. Shinya, and M. Notomi, "Coupling of small, low-loss hexapole mode with photonic crystal slab waveguide mode," *Optics Express*, vol. 12, no. 26, pp. 6624 – 6631, 2004.

[84] Y. Akahane, T. Asano, S. B. Song, and S. Noda, "Fine-tuned high-Q photonic-crystal nanocavity," *Optics Express*, vol. 13, no. 4, pp. 1202 – 1214, 2005.

[85] T. Tanabe, A. Shinya, E. Kuramochi, S. Kondo, H. Taniyama, and M. Notomi, "Single point defect photonic crystal nanocavity with ultrahigh quality factor achieved by using hexapole mode," *Applied Physics Letters*, vol. 91, no. 2, p. 021110, 2007.

[86] M. A. Adawi, R. A. A. Chalcraft, M. D. Whittaker, and G. D. Lidzey, "Refractive index dependence of L3 photonic crystal nano-cavities," *Optics Express*, vol. 15, no. 22, pp. 14299 – 14305, 2007.

[87] Y. Tanaka, T. Asano, and S. Noda, "Design of Photonic Crystal Nanocavity With Q-Factor of $\sim 10^9$," *Journal of Lightwave Technology*, vol. 26, no. 11, pp. 1532 – 1539, 2008.

[88] K. Srinivasan and O. Painter, "Momentum space design of high-Q photonic crystal optical cavities," *Optics Express*, vol. 10, no. 15, pp. 670 – 684, 2002.

[89] K. Srinivasan, E. P. Barclay, O. Painter, X. J. Chen, Y. A. Cho, and C. Gmachl, "Experimental demonstration of a high quality factor photonic crystal microcavity," *Applied Physics Letters*, vol. 83, no. 10, pp. 1915 – 1917, 2003.

[90] D. Englund, I. Fushman, and J. Vuckovic, "General recipe for designing photonic crystal cavities," *Optics Express*, vol. 13, no. 16, pp. 5961 – 5975, 2005.

[91] T. Asano, S. B. Song, Y. Akahane, and S. Noda, "Ultrahigh-Q nanocavities in two-dimensional photonic crystal slabs," *IEEE Journal of Selected Topics in Quantum Electronics*, vol. 12, no. 6, pp. 1123 – 1134, 2006.

[92] W. Kohn, "Analytic properties of Bloch waves and Wannier functions," *Physical Review*, vol. 115, no. 4, pp. 809 – 821, 1959.

[93] Z. J., A. Pyayt, L. R. Dalton, J. Luo, A. K.-Y. Jen, and A. Chen, "Photobleaching Fabrication of Microring Resonator in a Chromophore-Containing Polymer," *IEEE Photonics Technology Letters*, vol. 18, no. 21, pp. 2221 – 2223, 2006.

[94] H. Sun, A. Chen, B. C. Olbricht, J. A. Davies, P. A. Sullivan, Y. Liao, and L. R. Dalton, "Microring resonators fabricated by electron beam bleaching of chromophore doped polymers," *Applied Physics Letters*, vol. 92, p. 193305, 2008.

[95] R. V. Almeida, F. Q. Xu, A. C. Barrios, and M. Lipson, "Guiding and confining light in void nanostructure," *Optics Letters*, vol. 29, no. 11, pp. 1209 – 1211, 2004.

[96] T. Baehr-Jones, B. Penkov, J. Huang, P. Sullivan, J. Davies, J. Takayesu, J. Luo, T.-D. Kim, L. Dalton, A. Jen, M. Hochberg, and A. Scherer, "Nonlinear polymer-clad silicon slot waveguide modulator with a half wave voltage of 0.25 V," *Applied Physics Letters*, vol. 92, no. 16, p. 163303, 2008.

[97] J.-M. Brosi, C. Koos, L. C. Andreani, M. Waldow, J. Leuthold, and W. Freude, "High-speed low-voltage electro-optic modulator with a polymer-infiltrated silicon photonic crystal waveguide," *Optics Express*, vol. 16, no. 6, pp. 4177 – 4191, 2008.

[98] T. Yamamoto, M. Notomi, H. Taniyama, E. Kuramochi, Y. Yoshikawa, Y. Torii, and T. Kuga, "Design of a high-Q air-slot cavity based on a width-modulated line-defect in a photonic crystal slab," *Optics Express*, vol. 16, pp. 1645 – 1652, 2008.

[99] P. J. Hugonin, P. Lalanne, P. T. White, and F. T. Krauss, "Coupling into slow-mode photonic crystal waveguides," *Optics Letters*, vol. 32, no. 18, pp. 2638 – 2640, 2007.

[100] P. Sanchis, P. Bienstman, B. Luyssaert, R. Baets, and J. Marti, "Analysis of butt coupling in photonic crystals," *IEEE Journal of Quantum Electronics*, vol. 40, no. 5, pp. 541 – 550, 2004.

[101] A. Y. Vlasov and J. S. McNab, "Coupling into the slow light mode in slab-type photonic crystal waveguides," *Optics Letters*, vol. 31, no. 1, pp. 50 – 52, 2006.

[102] K. K. McLauchlan and S. T. Dunham, "Analysis of a compact modulator incorporating a hybrid silicon/electro-optic polymer waveguide," *IEEE Journal of Selected Topics Quantum Electronics*, vol. 12, pp. 1455 – 1460, 2006.

[103] J. D. Luo, Y. J. Cheng, T. D. Kim, H. S., S. H. Jang, Z. W. Shi, X. H. Zhou, and A. K.-Y. Jen, "Facile synthesis of highly efficient phenyltetraene-based nonlinear optical chromophores for electrooptics," *Organic Letters*, vol. 8, pp. 1387 – 1390, 2006.

[104] A. Chen, H. Sun, A. Pyayt, L. R. Dalton, J. Luo, and A. K.-Y. Jen, "Microring resonators made in poled and unpoled chromophore-containing polymers for optical communication and sensors," *IEEE Journal of Selected Topics in Quantum Electronics*, vol. 14, no. 5, pp. 1281 – 1288, 2008.

[105] I. Giuntoni, A. Gajda, M. Krause, R. Steingrüber, J. Bruns, and K. Petermann, "Tunable Bragg reflectors on silicon-on-insulator rib waveguides," *Optics Express*, vol. 17, no. 21, pp. 18518 – 18524, 2009.

[106] B. Kuhlow, G. Przyrembel, S. Schlüter, W. Fürst, R. Steingrüber, and C. Weimann, "Photonic Crystal Microcavities in SOI Photonic Wires for WDM Filter Applications," *Journal of Lightwave Technology*, vol. 25, no. 1, pp. 421 – 430, 2007.

[107] H. Chen, B. Chen, D. Huang, D. Jin, J. D. Luo, A. K.-Y. Jen, and R. Dinu, "Broadband electro-optic polymer modulators with high electro-optic activity and low poling induced optical loss," *Applied Physics Letters*, vol. 93, no. 4, p. 043507, 2008.

[108] T. Baehr-Jones, M. Hochberg, X. G. Wang, R. Lawson, Y. Liao, A. P. Sullivan, L. R. Dalton, K.-Y. A. Jen, and A. Scherer, "Optical modulation and detection in slotted Silicon waveguides," *Optics Express*, vol. 13, no. 14, pp. 5216 – 5226, 2005.

[109] R. van der Heijden, F. C. Carlstrom, A. P. J. Snijders, W. R. van der Heijden, F. Karouta, R. Notzel, W. M. H. Salemink, K. C. B. Kjellander, W. M. C. Bastiaansen, J. D. Broer, and E. van der Drift, "InP-based two-dimensional photonic crystals filled with polymers," *Applied Physics Letters*, vol. 88, no. 16, p. 161112, 2006.

[110] S. Tay, J. Thomas, B. Momeni, M. Askari, A. Adibi, J. P. Hotchkiss, C. S. Jones, R. S. Marder, A. R. Norwood, and N. Peyghambarian, "Planar photonic crystals infiltrated with nanoparticle/polymer composites," *Applied Physics Letters*, vol. 91, no. 22, p. 221109, 2007.

[111] G. M. Sessler, ed., *Electrets*, vol. 1. Laplacian Press, third ed., 1998.

[112] C. C. Teng and T. H. Man, "Simple reflection technique for measuring the electro-optic coefficient of poled polymers," *Applied Physics Letters*, vol. 56, no. 18, pp. 1734 – 1736, 1990.

[113] T. J. Sluckin, "Anchoring transitions at liquid crystal surfaces," *Physica A*, vol. 213, no. 1-2, pp. 105 – 109, 1995.

[114] E. P. Kosmidou and E. E. Kriezis, "Studies of photonic crystal structures infiltrated with liquid crystals," in *Proceedings of SPIE, Photonic Crystal Materials and Devices III (i.e. V)*, vol. 6182, p. 618213, 2006.

[115] D. Widman, H. Mader, and H. Friedrich, *Technology of integrated circuits*. Springer, 2000.

[116] R. Soref and B. Bennett, "Electrooptical effects in silicon," *IEEE Journal of Quantum Electronics*, vol. 23, pp. 123 – 129, 1987.

[117] S. Prorok, "Hochfrequente Ansteuerung eines elektro-optischen Modulators," Diplomarbeit, Hamburg University of Technology, 2009.

[118] R. W. Kopfenstein, "A transmission line taper of improved design," in *Proceedings of IRE*, vol. 44, pp. 31 – 35, 1956.

[119] Feng, N.-N. and Sun, R. and Kimerling, C. L. and Michel, J., "Lossless strip-to-slot waveguide transformer," *Optics Letters*, vol. 32, no. 10, pp. 1250 – 1252, 2007.

[120] S. J. Spector, C. M. Sorace, M. W. Geis, M. E. Grein, J. U. Yoon, T. M. Lyszczarz, E. P. Ippen, and F. X. Kärtner, "Operation and Optimization of Silicon-Diode-Based Optical Modulators," *IEEE Journal of Selected Topics in Quantum Electronics*, vol. 16, no. 1, pp. 165 – 172, 2010.

[121] J. M. Lee, D.-J. Kim, G.-H. Kim, O. K. Kwon, K.-J. Kim, and G. Kim, "Controlling temperature dependence of silicon waveguide using slot structure," *Optics Express*, vol. 16, no. 3, pp. 1645 – 1652, 2008.

List of Publications

Papers

- J. H. Wülbern, S. Prorok, J. Hampe, A. Petrov, M. Eich, J. Luo, A. K.-Y. Jen, M. Jenett, and A. Jacob, "40 GHz electro-optic modulation in hybrid silicon-organic slotted photonic crystal waveguides," *Opitcs Letters*, accepted for publication (2010).

- J. H. Wülbern, J. Hampe, A. Petrov, M. Eich, J. Luo, A. K.-Y. Jen, A. DiFalco, T. F. Krauss, and J. Bruns, "Electro-optic modulation in slotted resonant photonic crystal heterostructures," *Applied Physics Letters*, **94**, 241107 (2009).

- J. H. Wülbern, A. Petrov, and M. Eich, "Electro-optical modulator in a polymer infiltrated silicon slotted photonic crystal waveguide heterostructure resonator," *Optics Express*, **17**, 304 (2009).

- J. H. Wülbern, M. Schmidt, M. Eich, U. Hübner, R. Boucher, F. Marlow, and W. Volksen, "Omnidirectional photonic band gap in polymer photonic crystal slabs," *Applied Physics Letters*, **91**, 221104 (2007).

- J. H. Wülbern, M. Schmidt, U. Hübner, R. Boucher, W. Volksen, Y. Lu, R. Zentel, and M. Eich, "Polymer based tuneable photonic crystals," *physica status solidi (a)* **204**, 3739 (2007).

- J. H. Wülbern, M. Schmidt, M. Eich, and U. Hübner, "Electro-optically tunable photonic crystals," *Proc. SPIE Linear and Nonlinear Optics of Organic Materials VI*, **6331**, 633109 (2006).

Book articles

- J. H. Wülbern and M. Eich *Low dielectric contrast photonic crystals.* Optical Polymers for Photonics Applications, Ed.: R. A. Norwood, J. Thomas, John Wiley and Sons, New York, to be published in fall 2010.

- J. H. Wülbern, M. Schmidt, U. Hübner, R. Boucher, W. Volksen, Y. Lu, R. Zentel, and M. Eich, *Polymer based tunable photonic crystals.* Nanophotonic Materials, Ed.: R. Wehrspohn, H.-S. Kitzerow, K. Busch, Wiley-VCH, Weinheim (2008).

Talks

- J. H. Wülbern, J. Hampe, A. Petrov, M. Eich, J. Luo, A. K.-Y. Jen, A. DiFalco, T. F. Krauss, and J. Bruns, "Electro-optic modulation in hybrid SOI and polymer slotted resonant photonic crystal heterostructures", 6th International Conference on Group VI Photonics, San Francisco, USA, 9–11 September, 2009.
- J. H. Wülbern, J. Hampe, A. Petrov, and M. Eich, "Electro-optical modulator in a polymer-infiltrated silicon slotted photonic crystal waveguide heterostructure resonator", PECS-VIII, Sydney, Australia, 5–9 April, 2009.
- J. H. Wülbern, J. Hampe, A. Petrov, and M. Eich, "Electro-optical modulator in a polymer-infiltrated silicon slotted photonic crystal waveguide heterostructure resonator", DPG Annual Meeting, Dresden, Germany, 22–27 March, 2009.
- J. H. Wülbern, J. Hampe, A. Petrov, and M. Eich, "Polymer-SOI hybrid photonic nano-structures", Workshop on Tunable and Active Silicon Photonics, Hamburg, Germany, 28–30 September, 2008.
- J. H. Wülbern, J. Hampe, A. Petrov, and M. Eich, "Investigations of microphotonic structures with CST Microwave Studio", Design Challenges: Optics Simulations with CST MWS, Twente, Netherlands, 3 June, 2008.
- J. H. Wülbern, M. Eich, U. Hübner, R. Boucher, Y. Lu, and R. Zentel, "Electro-optically tunable photonic crystals", DFG-SPP 1113 Abschlusstreffen, Bad Honnef, Germany, 22–25 April, 2007.
- J. H. Wülbern, M. Schmidt, A. Petrov, and M. Eich, "Electro-optically tunable photonic crystals" SPIE Photonics Europe, Strasbourg, France, 2–8 April, 2006.

Posters

- J. H. Wülbern, J. Hampe, M. Eich, U. Hübner, R. Boucher, Y. Lu, and R. Zentel, "Electro-optically tunable photonic crystals", PECS-VII, Monterey, USA, 8–11 April, 2007.
- J. H. Wülbern, M. Schmidt, M. Eich, U. Hübner, R. Boucher, R. Zentel, "Electro-optically tunable photonic crystals", DPG Annual Meeting, Frankfurt, Germany, 13–17 March, 2006.

Supervised Student Projects

- Stefan Prorok, Hochfrequente Ansteuernung eines elektro-optischen Modulators. Diplomarbeit (2009).
- Adarsha Kanchana, Disorder effects on the performance of PhC slab cavities. Project work (2009).
- Panagiotis Androutsos, Slow light photonic crystal cavities. Master thesis (2008).
- Focho Atte Formum, Numerical study of the impact of disorder in photonic crystal resonators. Project work (2008).
- Hooi Sing Lee, Low index photonic crystal nano-cavities. Project work (2008).
- Cecilia Flores Mozo, Poling and optical characterization of novel electro-optic chromophores. Project work (2007).
- Panagiota Politi, Experimental characterization and optimization of electrode poling for novel electro-optic polymers. Project work (2007).
- Hui Liu, Investigation and benchmarking of a novel finite difference time domain (FDTD) algorithm for photonic crystal structures. Diplomarbeit (2007).

Acknowledgements

Die folgenden Worte der Danksagung möchte ich gerne in deutscher Sprache verfassen. Zu dem Gelingen der vorliegenden Arbeit haben viele Personen beigetragen, bei denen ich mich bedanken möchte.

Zu Beginn vielen Dank an Prof. Manfred Eich, der mich in sein Team geholt und somit überhaupt erst den Rahmen für eine erfolgreiche Arbeit geschaffen hat und darüber hinaus für die Arbeitsmethoden und -techniken, die ich während unserer Zusammenarbeit durch ihn erlernt habe. Dank natürlich auch an Prof. Wolfgang Bauhofer für seine Unterstützung als Institutsleiter, sowie an Prof. Ernst Brinkmeyer für die gute Zusammenarbeit mit seinem *Institut für Optische Kommunikationstechnik* und ebenso Prof. Jörg Müller und dem *Institut für Mikrosystemtechnik*.

Ich möchte mich bei allen derzeitigen und ehemaligen Mitarbeitern des *Instituts für optische und elektronische Materialien* bedanken, die mich die Jahre begleitet und immer für eine angenehme Atmosphäre und gute Stimmung im Institut gesorgt haben. Besonders erwähnen möchte ich hier Gabriele Birjukov, Iris Bucher, Michael Seiler und Stefan Schön ohne deren Hilfe bei so vielen labor-, büro- und verwaltungstechnischen Angelegenheiten diese Arbeit wohl nie vollendet worden wäre. Auch ohne die Mithilfe des Photonischen-Kristall-Flüsterers Alexander Petrov hätte ich die Lichtausbreitung in Bloch-Moden nie in solcher Tiefe verstanden. Nicht unerwähnt lassen möchte ich hier meinen langjährigen Zellengenossen Jan Hampe ohne den die Zeit einfach so viel langweiliger gewesen wäre ("Willst du noch Tee, Tante?" und TGIF). Schließlich auch vielen Dank an alle Studenten, die durch ihre Studien- und Diplomarbeiten wichtige Puzzleteile zu der vorliegenden Arbeit beigesteuert haben.

Zu Dank verpflichtet bin ich ebenfalls den vielen Kollegen aus anderen Instituten der TUHH und weiteren Universitäten: Dr. Matrin Jenett und Prof. Jacob (*Institut für Hochfrequenztechnik*) für die Hilfe bei der Umsetzung der HF-Messungen; Dr. Andrea di Falco und Prof. Thomas Krauss (*University of St. Andrews, Schottland*) für die Unterstützung bei der optischen Charakterisierung und dem Bereitstellen von PhC-Proben; Dr. Jingdong Luo und Prof. Alex K.-Y. Jen (*University of Washington, USA*) für die Synthese des NLO-Chromophores; Dr. Ralf Steingrüber für die E-Beam Lithographie (*HHI Berlin*) und Dr. Jürgen Bruns (*TU Berlin*) für das ICP Ätzen der SOI Strukturen; sowie Dr. Uwe Hübner (*IPHT Jena*) für die Herstellung der Polymer PhC-Proben. Das Simulationstool MicrowaveStudio wurde von der Firma CST in Darmstadt zur Verfügung gestellt, herzlichen Dank daher auch CST und Dr. Irina Munteanu.

Vielen Dank auch an die Deutsche Forschungsgemeinschaft, die dieses Projekt im Rah-

men des Schwerpunktprogramms *Photonische Kristalle*, sowie der Forschergruppe *Aktive und abstimmbare mikrophotonische Systeme auf der Basis von Silicon-on-Insulator (SOI)* gefördert hat. In diesem Zusammenhang auch vielen Dank an die Kollegen der Forschergruppe, insbesondere Jost Müller, Michael Krause, Julia Amthor und Oliver Horn für die konstruktive Zusammenarbeit.

Natürlich wäre ich ohne die Unterstützung und den Rückhalt meiner Eltern Monika und Volker Wülbern niemals zu dem Punkt gekommen, überhaupt ein solches Projekt beginnen zu können: daher gilt ihnen mein ganz besonderer Dank.

Abschließend und in besonderem Maße danke ich Sünje Callsen für ihre Geduld und Verständnis für all die Zeiten, in denen dieses Projekt mehr Raum als geplant eingenommen hat und sie trotzdem immer die richtigen Worte des Zuspruches und der Motivation fand.